University of California
Santa Barbara

Role of neighborhood constraints on deformation twinning in magnesium

A dissertation submitted in partial satisfaction
of the requirements for the degree

Doctor of Philosophy
in
Materials

by

Brandon Leu

Committee in charge:

Professor Irene J. Beyerlein, Chair
Professor Matthew R. Begley
Professor Samantha Daly
Professor Daniel S. Gianola

June 2022

The Dissertation of Brandon Leu is approved.

Professor Matthew R. Begley

Professor Samantha Daly

Professor Daniel S. Gianola

Professor Irene J. Beyerlein, Committee Chair

March 2022

Role of neighborhood constraints on deformation twinning in magnesium

by

Brandon Leu

Dedicated to my family, friends and future.

Acknowledgements

Firstly, I would like to thank my parents, whose unwavering love and dedication to my brother and me has allowed us to pursue a better future than was available to them. I am eternally grateful to my grandma, who raised me and instilled in me the values of education, hard work, and selflessness. I am also especially thankful for my girlfriend of twelve years, Kelly, for bringing me endless joy and supporting me through all of my life endeavors. Her constant positivity and motivation has been a major key to my success.

I would like to thank Professor Suveen Mathaudhu, for enabling and inspiring me to pursue a degree in materials engineering. His guidance and confidence in me has allowed me to succeed in many aspects of my life. I would also like to thank Dr. M. Arul Kumar for his tireless commitment to my success. He has always been willing to share with me his wisdom in all things, academic or otherwise, and I am grateful for both his mentorship and friendship. Finally, I would like to thank my advisor, Professor Irene Beyerlein, for her mentorship, enthusiasm, and encouragement during my graduate studies. Her unique kindness towards everyone and unwavering patience in revealing the many mysteries of science has been inspirational. My PhD journey would not have been possible without her. I am fortunate and proud to have been a part of her first group of graduate students.

Curriculum Vitæ

Brandon Leu

Education

2022	Ph.D. in Materials, University of California, Santa Barbara.
2016	B.S. in Materials Science and Engineering, University of California, Riverside.

Publications

13. **B. Leu**, M. Arul Kumar, K.Y. Xie, I.J. Beyerlein, "Twin growth mechanism enabled by precipitates in AZ91", Acta Materialia 2022 (Submitted)
12. **B. Leu**, M. Arul Kumar, P. Rottmann, K. Hemker, I.J. Beyerlein, "Micromechanical fields associated with irregular deformation twins in magnesium", Journal of Materials Engineering and Performance 2022 (Submitted)
11. **B. Leu**, M. Arul Kumar, K.Y. Xie, I.J. Beyerlein, "Twinning pathways enabled by precipitates in AZ91", Materialia 2021, 21, 101292
10. **B. Leu**, M. Arul Kumar, I.J. Beyerlein, "The effects of free surfaces on deformation twinning in HCP metals", Materialia 2021, 17, 101124
9. K.Y. Xie, D. Zhao, **B. Leu**, X. Ma, Q. Jiao, J.A. El-Awady, T.P. Weihs, I.J. Beyerlein, M. Arul Kumar, "Understanding the interaction of extension twinning and basal-plate precipitates in Mg-9Al using precession electron diffraction", Materialia 2021, 15, 101044
8. K. Yaddanapudi, **B. Leu**, M. Arul Kumar, X. Wang, J.M. Schoenung, E.J. Lavernia, T.J. Rupert, I.J. Beyerlein, S. Mahajan, "Accommodation and formation of $\{10\bar{1}2\}$ twins in Mg-Y alloys", Acta Materialia 2021, 204, 116514
7. **B. Leu**, M. Arul Kumar, I.J. Beyerlein, "Influence of layer thickness on deformation twinning in Mg/Nb laminates", Magnesium Technology 2021, 3-8
6. **B. Leu**, M. Arul Kumar, I.J. Beyerlein, "The effects of basal and prismatic precipitates on deformation twinning in AZ91 magnesium alloy", Magnesium Technology 2021, 73-79
5. **B. Leu**, M. Arul Kumar, Y. Liu, I.J. Beyerlein, "Deviations from theoretical orientation relationship along tensile twin boundaries in Magnesium", Magnesium Technology 2020,123-128
4. J.W. Zhang, **B. Leu**, M. Arul Kumar, I.J. Beyerlein, W.Z. Han, "Twin hopping in nanolayered Zr-2.5 Nb", Materials Research Letters 2020, 8 (8), 307-313
3. **B. Leu**, D.J. Savage, J. Wang, M.E. Alam, N.A. Mara, M. Arul Kumar, J.S. Carpenter, S.C. Vogel, M. Knezevic, R. Decker, I.J. Beyerlein, "Processing of dilute Mg-Zn-Ca alloy/Nb multilayers by accumulative roll bonding", Advanced Engineering Materials 2019, 22 (1), 1900673

2. M. Arul Kumar, **B. Leu**, P. Rottmann, I.J. Beyerlein, "Characterization of staggered twin formation in HCP Magnesium", Magnesium Technology 2019, 207-213

1. A. Hunter, **B. Leu**, I.J. Beyerlein, "A review of slip transfer: applications of mesoscale techniques", Journal of Materials Science 2018, 53 (8), 5584-5603

Abstract

Role of neighborhood constraints on deformation twinning in magnesium

by

Brandon Leu

Magnesium alloys have garnered much interest in automotive and aerospace industries, where simultaneously light-weight and strong components are needed to improve energy efficiency without sacrificing structural stability. However, the widespread application of magnesium has been limited due to its poor room temperature formability, which renders it incompatible with modern industrial processing methods, such as rolling, forming, die punching and extrusion techniques. Unlike traditional structural metals that deform primarily by dislocation slip, the deformation of magnesium alloys is carried out by a combination of dislocations motion and the development of deformation twins. Twinning deformation occurs on the grain scale and can strongly influence the mechanical properties of the material, such as ductility, strength, and stability. Thus, a fundamental understanding of how dislocations and twins interact with each other and with other common microstructural features found in magnesium alloys is critical in the design of useful magnesium components for industrial applications.

In this work, an elasto-viscoplastic fast-Fourier-transform (EVP-FFT) computation model was used in order to investigate the interaction between twins and two commonly encountered microstructural features: precipitates and free surfaces. First, we consider a newly propagated twin that intersects a $Mg_{17}Al_{12}$ basal precipitates in AZ91. It is shown that these precipitates can impede the propagation and thickening of twins, however, the impingement of a twin against one side of a precipitate can cause local stress concentrations to develop along the precipitate-matrix boundary, where a new twin of

the same or different twin variant can nucleate from. Both the relative thickness and length of the precipitate, in relation to the thickness of the twin, are important factors that determine how twins can continue to develop. The size of the precipitate is a key factor in controlling twinning deformation during the early stages of development and determining the twinning pathways that emerge.

Next, a dislocation-density based hardening law was incorporated into EVP-FFT framework in order to reveal the evolution of the spatial distribution of dislocation densities in the microstructure. Here, defect content in addition to adequate stresses are used as indicators for the determining how twins will continue developing. By considering twinning from the early stages of deformation, a two-step twin growth mechanism is proposed: starting with an initial twin propagation front that impinges upon a precipitate, resulting in a stress concentration that develops on the other side of the precipitate that prompts the formation of a second twin. Subsequently, the backstresses around the first twin are relaxed by the propagation of a second twin, allowing the first twin to grow at the twin-precipitate junction and eventually engulf the precipitate. This mechanism suggests that twin growth can be achieved locally with minimal additional external forces, explaining how relatively large twin domains can develop even in the presence of arrays of precipitates, despite contradictory reports that precipitates harden against twin growth. The precipitate spacing is shown to affect the stresses and dislocation generated near the twin-precipitate interaction site that support twin growth.

Lastly, a method for simulating free surface relaxation was implemented to study how free surfaces can affect the development of twins. Surface analysis techniques, such as SEM and TEM, that make up the bulk of the experimental evidence regarding twin development inevitably expose twins to free surfaces during the sample preparation process. The advanced model allows the stress fields generated by the twin to be deconvoluted from the free surface relaxation and provides insight into the differences between mi-

cromechanical fields found in the interior of a bulk grain compared to grains at a free surface. The calculated field predicted by the model when accounting for free surface effects are quantitatively and qualitatively closer in comparison to experimentally measured fields. The calculations indicate that twins near the free surfaces have a greater propensity to develop larger, asymmetrically, and with blunted tips when compared to twins located in the interior grains.

This works makes several critical advances towards improving the fundamental understanding of how twins develop in the presence of a field of elastically hard precipitates and at free surfaces. The improvements of the EVP-FFT modeling framework has been used to gain a better fundamental understanding of the role of precipitates on twinning behavior and the microstructural features that influences how twins develop. The model calculations provide insight into how to control deformation twinning by controlling the size and spacing of precipitates, which can be achieved through careful alloying selection and heat treatment processes. Furthermore, the model has revealed the effects of free surfaces on the experimental observations of twins, illustrating how near surface measurements may not be directly translated to bulk properties. The model introduces a framework to bridge the connection between lab-scale samples and their bulk counterparts.

Contents

List of Figures

List of Tables

Chapter 1

Introduction

1.1 Motivation

As modern technology advances, there is an ever-growing demand for structural materials that are simultaneously sustainable, light-weight and strong. Magnesium (Mg) uniquely satisfies these criterions, while also having good castability and weldability. Mg is highly recyclable and readily available as the eighth most abundant element in the Earth's crust [11]. Furthermore, Mg has a low density of 1.74 $\frac{g}{cm^3}$ and is approximately 30% lighter than aluminum (Al) and 75% lighter than steel. Its low weight and high specific strength makes Mg an ideal candidate base metal for structural applications. As a result, Mg-based alloys have become highly desirable in many industrial applications where light-weighting can yield tremendous benefits for fuel efficiency without the need to sacrifice structural strength. For example, according to some estimations, light-weight construction of automobiles can yield up to 10-15% in fuel savings and reduce CO_2 emissions by up to 30% [12].

A common strategy that has been employed to develop Mg alloys with improved mechanical strength and ductility is through alloying. Table 1.1 lists some Mg alloys

that have been used in automotive applications [10]. Mg alloys have reported tensile yield strengths between 156–277 MPa, which is comparable to that of aluminum (100–240 MPa) [13], however, still far below that of steel (350 MPa) [14]. Another example can be seen in a Mg alloy containing Zn and Ca that form Guinier-Preston (GP) zones to achieve a combination of ductility and strength are comparable to aluminum 6000 series alloys [15]. Despite having comparable mechanical strength to Al, Mg only contributed to 0.3% of the average weight of a domestic vehicle in 2013 while Al contribute 9.5% [16]. The disparity in industrial application between Mg and Al is due, in large part, to the challenges associated with manufacturing and processing of Mg components [17]. The geometry of automotive components can be complex and range greatly in sizes, which is typically achieved through conventional forming processes that require severe plastic deformation. A major disadvantage of Mg that has limited its widespread application as a structural material is its poor formability.

Alloy	Comp (%)	TS (MPa)	YS (MPa)	El (%)	ρ ($\frac{g}{cm^3}$)	Creep*
AZ91D	9Al,0.7Zn,0.17-0.4Mn	230	160	3	1.81	3
AM60B	6Al,0.2Zn,0.15-0.5Mn	220	130	6-8	1.78	3
AM50A	5Al,0.2Zn,0.28-0.5Mn	220	110	6-10	1.78	3
AM20	2Al,0.23Mn	210	90	12	1.78	3
RZ5	4.2Al,1.2Re,0.7Zr	218	148	4	1.78	3
MEZ	2.5Al,1.2Re,0.35Zn	172	145	5	1.78	2
ZAC8506	8Zn,5Al,0.6Ca	219	146	5	1.8	2
AMC5006	5Al,0.6Ca,0.32Mn	156	95	8.5	1.78	2
MRI 151		277	175	7.5		2
MRI 177		275	177	6.7		2
Noranda-A1		202	145			2

Table 1.1: Composition and mechanical properties of magnesium alloys used in automobiles. Adapted from Baghni et al. [10].

Poor formability in Mg is primarily caused by its hexagonal-close-packed (HCP) structure and limited number of active slip systems. Unlike traditional metals, such as Al, that have a face-centered cubic (FCC) crystal structure with 12 independent slip systems to accommodate deformation, only three slip systems along the basal plane are easily activated in Mg at low and room temperatures [18]. However, basal slip does not accommodate deformation in the direction normal to the basal plane. Instead, deformation twinning is commonly observed in Mg and Mg alloys under ambient conditions. Twinning is an important mode of plastic deformation in these materials that can provide greater ductility by accommodating strain along the $\langle c \rangle$-axis of the crystal and my reorienting portions of grains more favorably for slip [19, 20]. However, twinning also strongly influences the strain hardening response [21], texture evolution [22, 23] and the generation of strain localization that can ultimately lead to premature failure of the material under loading [24]. Therefore, in order to develop useful light-weight Mg alloys for industrial applications, it is necessary to understand how twins develop and their respective roles on the creation of heterogeneous micromechanical fields around them that control the overall mechanical behavior of the material. This is an outstanding challenge that is not yet fully understood.

In the following section, an introduction of the predominant dislocation mediated slip and twinning deformation mechanisms of Mg alloys are presented. Next, the interactions of dislocations with common microstructural features, such as precipitates, are summarized with respect to their ability to influence the macroscopic mechanical response. Unlike dislocation-precipitate interactions, which have received much attention over the years and are generally well understood [25, 26], twin-precipitate are much less understood. Then, an Elasto-ViscoPlastic Fast-Fourier-Transform (EVP-FFT) crystal plasticity-based model [27] is presented that will be used to calculate and predict the micromechanical fields associated with developing twins as they interact with vari-

ous microstructural features, such as precipitates, nearby twins, free surfaces and grain boundaries. The model is able to give insight into rare twinning events that would be otherwise difficult to isolate and observe experimentally.

1.2 Plastic deformation in magnesium and its alloys

The commonly observed slip systems in Mg include: basal $\{0001\}\ \langle 11\bar{2}0\rangle$, prismatic $\{01\bar{1}0\}\ \langle 2\bar{1}\bar{1}0\rangle$, and pyramidal-I $\{10\bar{1}1\}\ \langle \bar{1}\bar{1}23\rangle$ [28]. In the past, pyramidal-II slip $\{11\bar{2}2\}\ \langle \bar{1}\bar{1}23\rangle$ had been frequently reported [29], however, more recent works have surfaced that support the prevalence of pyramidal-I over pyramidal-II slip [30, 31]. $\langle a\rangle$-type pyramidal slip $\{0\bar{1}11\}\ \langle 2\bar{1}\bar{1}0\rangle$ is also possible, but has only been reported at higher temperatures, above 225°C [32]. At lower temperatures, $\langle a\rangle$-type basal or prismatic slip have a much lower critical resolved shear stress (CRSS) to activate and can accommodate strain along the same directions [32]. The crystallographic slip planes and directions are schematically illustrated in Figure 1.1a [1].

The values of the CRSS for basal, prismatic and pyramidal $\langle c+a\rangle$ slip systems and twinning are varied between reports in the literature and depend heavily on temperature and chemistry, whether pure Mg [33, 32, 34] or alloyed [35, 36, 37]. However, the relatives strengths under ambient conditions are well agreed upon, with basal slip and twinning frequently being the easiest to activate, followed by prismatic, and finally pyramidal $\langle c+a\rangle$ systems being the hardest [38]. Table 3.1 lists some CRSS values for slip and twinning that have been reported for Mg and its alloys.

In addition to slip, deformation twins are often found in metals with lower crystal symmetry that lack five independent slip systems required to satisfy the Taylor criterion for general plastic deformation; in which case, both slip and twinning are needed. In Mg, basal $\langle a\rangle$, prismatic $\langle a\rangle$ and pyramidal $\langle a\rangle$ slip only provide four independent slip

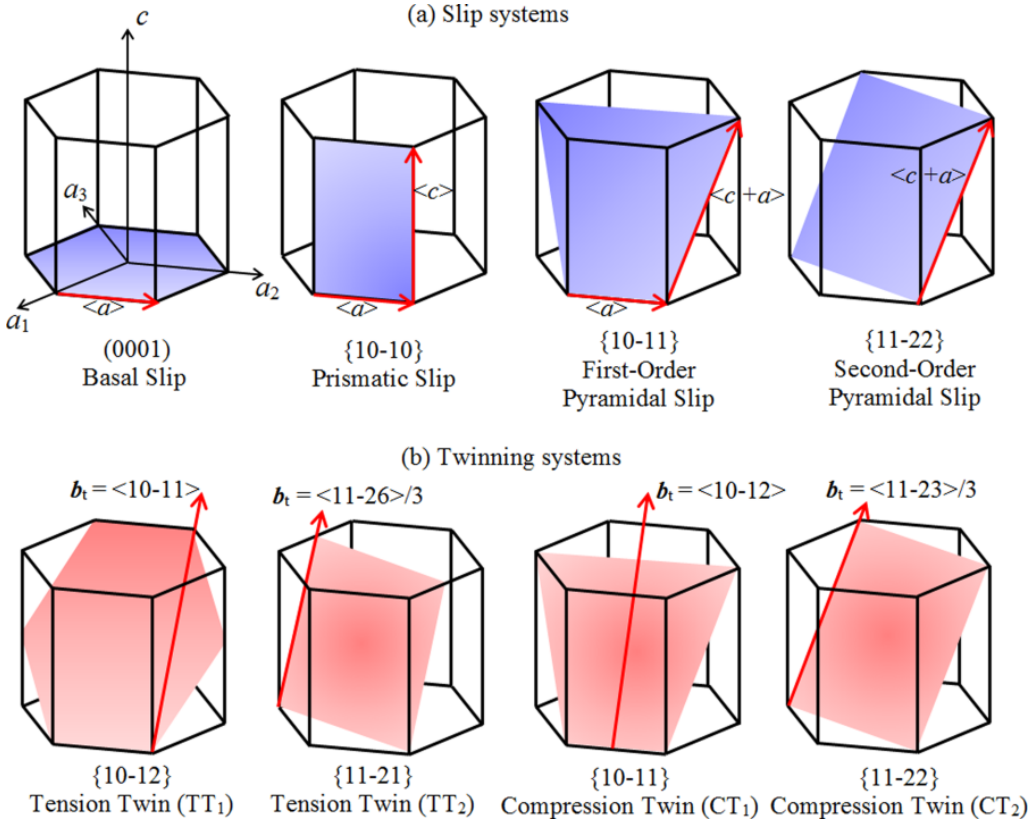

Figure 1.1: Crystallographic (a) slip and (b) twinning systems of HCP metals. Taken from Fan et al. [1]

Composition	Basal $\langle a \rangle$	Prismatic $\langle a \rangle$	Pyramidal $\langle c+a \rangle$	Tensile twinning	Reference
Pure Mg	3.3	35.7	86.2	11	[33]
AZ91	20	85	120	45	[35]
AZ91	44	90	169	NA	[39]
AZ31	12	60	100	60	[40]
AZ31B	12	60	100	60	[41]
WE43	12	78	130	85	[36]
Z6	25	113	NA	23	[42]
Mg-Y	9	85	100	10	[43]

Table 1.2: Reported critical resolved shear stress required to activate basal slip, prismatic slip, pyramidal slip and tensile twinning. Values are in MPa.

systems, and while the activation of pyramidal $\langle c+a \rangle$ slip could provide the additional independent slip systems, it is difficult to activate due to its large CRSS values [44, 45]. The crystallographic twin systems for HCP crystals are schematically illustrated in Figure 1.1b. Tension twins $\{10\bar{1}2\}$ $\langle \bar{1}011 \rangle$, also called extension twins, help to accommodate $\langle c \rangle$-axis extension [46, 47] and are the most ubiquitous type of twins in Mg at room temperature, sometimes reaching twin volume fractions of up to 70% by 10% engineering strain [40, 48]. There are other deformation twin modes, such as compression twins $\{10\bar{1}2\}$ $\langle 10\bar{1}1 \rangle$, that accommodate $\langle c \rangle$-axis contraction [46], also called contraction twins, however, they are relatively uncommon and usually require large stresses to activate [24, 49, 50, 51].

In principle, twins form through a homogenous simple shearing of the parent lattice [52]. A subregion of a grain, the twin domain, undergoes a coordinated directional shear that reorients the twin such that the twin and parent lattices are related to each other by a reflection about a crystallographic plane or a 180° rotation about a crystallographic direction [28, 53]. In Mg, the twin has a mirror symmetry with the parent lattice about the twin plane(K_1), which is equivalent to a 180° rotation about the twinning shear direction (η_1) [54]. The amount of shear and rotation of the twin can vary depending on the geometry of the crystal structure. For Mg, which has a $\frac{c}{a}$ ratio of 1.624, the characteristic twin shear is 12.6% and the twin is reoriented by 86.3° [46], as shown in Figure 1.2 [2, 3].

The formation of twins can be generalized into three distinct stages: twin nucleation, twin propagation (in the twinning shear direction), and twin growth (in the twin plane normal direction) [55, 54]. Experimental evidence suggests that twin nucleation is likely to occur along interfaces, such as grain boundaries [56, 33, 57] where there are adequate defects and sufficiently high local stresses to support the dislocation reactions necessary to form a twin nucleus of critical size [58, 59, 60, 61]. Once nucleated, the twin can rapidly

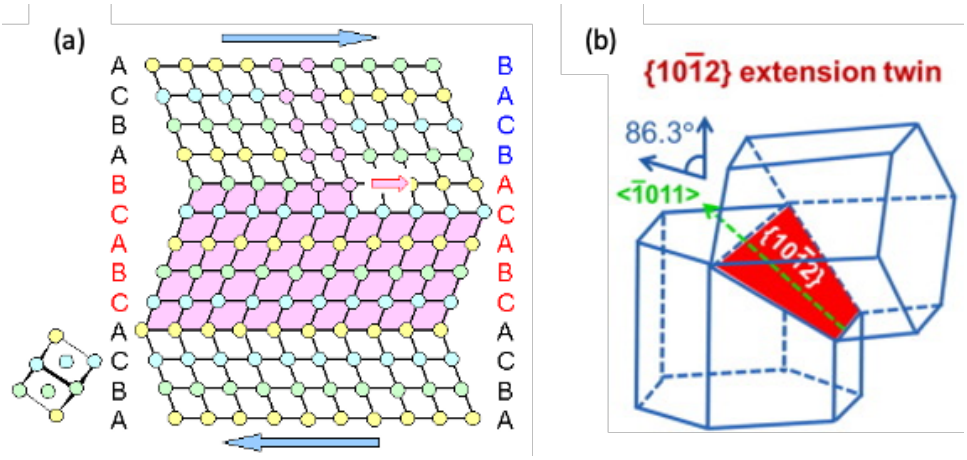

Figure 1.2: Schematic illustration of (a) the simple shear process in the twin domain [2] and (b) the resulting crystal reorientation. Schematic adapted from Guo et al. [3]

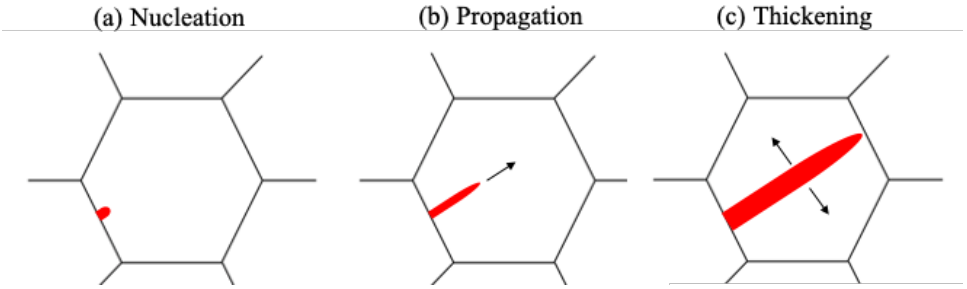

Figure 1.3: Schematic illustration of the twinning processes: (a) twin nucleation at a grain boundary (b) twin propagation in the twinning shear direction across the grain and (c) twin growth/thickening, characterized by the migration of the twin boundary in the twin plane normal direction.

propagate across the grain, taking on a lamellar or lenticular shape [62, 63]. Typically, propagation does not stop until they impinge upon an obstacle, such as a grain boundary or precipitate [64]; however, in some cases, twins have been observed to terminate in the interior of the grain [65, 66]. Finally, once the thin twin has been arrested on both ends and under appropriate loading conditions, the twin boundaries may begin to migrate and thicken the twin. The dissociation of basal dislocation at the $\{10\bar{1}2\}$ tensile twin boundaries in Mg develops facets that facilitate the migration of the twin boundary in the twin plane normal direction through a combination of twinning dislocation glide and

climb along the facets [67, 68, 69, 70, 71, 72, 73, 74, 75, 76]. As indicated by these studies, the presence of suitable defects in combination with favorable driving stresses are needed to advance the twin boundary. Each stage of the twinning process is unique and merits individual treatment and assessment of their contributions to the overall macroscopic mechanical properties.

1.3 Precipitates in magnesium alloys

Precipitation strengthening has been an effective approach to improving the mechanical properties of various metallic systems [77, 78, 79]. Precipitation strengthening is achieved through a distribution of unshearable precipitates throughout the solid-solution matrix that block the glide of dislocations [26, 25]. The strengthening provided by the precipitates in Mg alloys has been approximated by an Orowan-type equation, where the precipitate size, shape, habit plane, orientation, and spacing are all important contributing factors [80, 81, 4, 82, 83]. Various different precipitates can be formed through careful alloying and heat treatment processes, which involves a solution treatment at relatively high temperatures in the α-Mg single-phase region, followed by quenching to obtain a supersaturated solid-solution of alloying elements in Mg, and lastly a final aging at lower temperatures, where fine precipitates are able to decompose out of the supersaturated solution into the Mg matrix and at grain boundaries via continuous and discontinuous precipitation [4, 84].

In particular, Mg-Al systems have gain much attention [85, 4, 5]. According to the Mg-Al binary phase diagram, $\beta-$ $Mg_{17}Al_{12}$ precipitates can form with an equilibrium volume fraction up to 11.4% [4]. $\beta-Mg_{17}Al_{12}$ precipitates are resistant to dislocation shearing, have a body-centered-cubic (BCC) crystal structure, and form along the basal plane of the α-Mg parent matrix with plate-shaped morphology [86, 4]. The Burgers

orientation relationship ($(0001)_\alpha//(011)_\beta$ and $[2\overline{1}\overline{1}0]_\alpha//[1\overline{1}1]_\beta$) [86, 85], and the similar Potter [87, 88] orientation relationship ($(0001)_\alpha$ 2° from $(011)_\beta$ and $[2\overline{1}\overline{1}0]_\alpha//[1\overline{1}1]_\beta$) have been reported between the $\beta-Mg_{17}Al_{12}$ and the α-Mg parent matrix. A transmission electron micrograph (TEM) from Nie et al. [4] is shown in Figure 1.4.

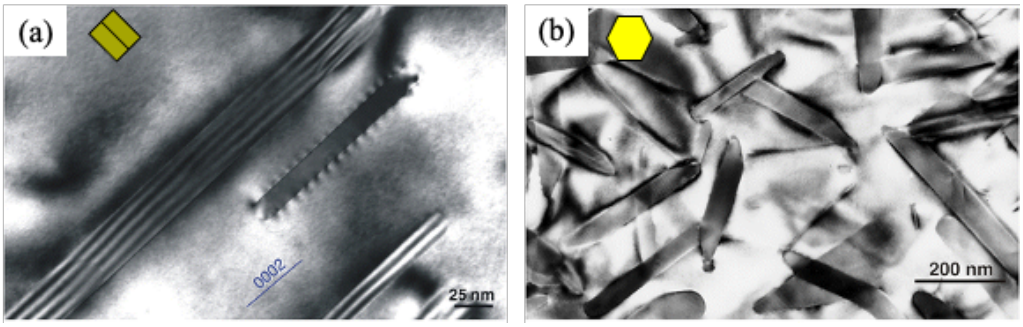

Figure 1.4: TEM micrograph adapted from Nie et al. [4] showing size, distribution and morphology of commonly observed $\beta-Mg_{17}Al_{12}$ precipitates in AZ91. The micrographs correspond to the electron beam parallel to (a) the $[2\overline{1}\overline{1}0]_\alpha$ and (b) $[0001]_\alpha$ directions. The orientation of α-Mg is schematically illustrated by the hexagonal insets in yellow.

In contrast to dislocation-precipitate interactions, twin-precipitate interactions are much less is understood. Unlike slip, twins are three-dimensional and develop through a sequence of nucleation, propagation and then thickening, as described in Section 1.2. Precipitates can influence the development of twins during each stage uniquely and thus precipitate-twin interactions should be treated separately. In regard to precipitate effects on twin nucleation, it has been suggested that precipitate/matrix interfaces can serve as nucleation sites since their defect and stress concentrations are higher compared to the matrix [89]. Consistent with this notion, experimental evidence has shown that the volume fraction of twins remains consistent, regardless of precipitate volume fractions; however, the presence of precipitates correlate well with an increase in the density of twins and a decrease in twin size, implying that precipitates can enhance multiple twin formation while suppressing twin thickening [90, 42, 91, 92]. Twin-precipitate interactions that involve twin nucleation have been investigated by computational methods as well.

Tang et al. used molecular dynamics (MD) simulations to show that twin-precipitate interaction sites can initiate twinning dislocation loops that lead to a reduction in the resolved shear stress needed to nucleate twinning dislocation partials under strain rates of 10^6 1/s at 283 K [93].

A majority of studies in the literature investigate twin-precipitate interactions during twin thickening. It is generally accepted that a distribution of precipitates can block and pin the lateral migration of the twin boundary, thereby increasing the resolved shear stress needed to grow the twin. Some theoretical models have treated twinning synonymously with slip and described the strengthening akin to an Orowan bowing mechanism of twinning dislocation partials around the precipitates [94, 92, 95, 4]. Barnett extended this idea by representing the twinning dislocations as a wall of super-dislocations, which yielded closer approximations to experimentally observed values of strengthening [96]. This model was later supported by dislocation-dynamics (DD) simulations [94]. Other computational methods have been used to study precipitate effects on twin thickening as well. For example, Jain et al. used transmission electron microscopy (TEM) combined with visco-plastic self-consistent modeling to study the role of long-range elastic back-stresses developed by precipitates on hardening slip and twinning [42]. Liu et al. used crystal plasticity phase-field simulations to show that precipitate size and habit-plane alignment with the twin boundary play critical roles on the critical resolved shear stress required for twin thickening [97]. Siska et al. used a crystal plasticity based finite element method to show that precipitates can indirectly suppress the twin thickening process by hardening the slip modes that would normally relax the stresses around the twins [39]. Another study, using MD simulations by Fan et al., showed that basal dislocations and stacking faults can nucleate at the twin-precipitate interfaces, causing local plastic relaxation [98]. As a result, they were able to rank the effectiveness of precipitate shapes on hardening, showing that spheres have the strongest hardening, followed by plates and

then rods.

Despite the great efforts towards understanding twin-precipitate interactions in the recent years, there are still many unknowns. For instance, while it is generally accepted that precipitates impede the growth of twins, large twin domains that can engulf entire precipitates are still commonly observed [5, 99, 100]. The various analytical and computation models that exist to describe the strengthening by precipitates against twin thickening do not agree with each other, nor do they accurately predict the experimentally measured values [101, 97]. These studies primarily focus on twins that are prexisting in the parent matrix, but do not consider how the twins have initially propagated. Furthermore, precipitate effects during the twin propagation stage have been largely ignored to this point. The ability of precipitates to potentially divert, blunt, or affect the nucleation of new twins after a propagating twin impinges on the precipitate can determine the final twinning microstructure (e.g., morphology and variant selection) and thus are important to consider. Also, the role of dislocations on the twin growth process in connection with precipitates have not been studied thoroughly. As discussed in Section 1.2, adequate stresses in combination with dislocations are important for the migration of the twin boundaries. While Siska et al. [39] revealed the importance of the plastic accommodation of the surrounding matrix around a twin, the CRSS values used in his simulations were constant and did not evolve spatially with deformation, thus making it difficult to assess whether the dislocation densities at the boundaries are sufficient or realistic.

1.4 Free surface effects during the characterization of twins

A variety of experimental techniques, including neutron diffraction, X-ray diffraction, and scanning (SEM) and transmission electron microscopy (TEM) in conjunction with digital image correlation (DIC) have been employed to understand the effect twins have on the evolution of internal stresses [102, 103, 41, 9, 104, 64]. X-rays allow for non-destructive investigation of the internal microstructure, however, it can be limited in its spatial resolution and interaction volume [105, 106]. Electron microscopy techniques offer higher resolution, faster data acquisition, and can collect data over larger areas of the specimen; however, the sample preparation required for these techniques introduces free surfaces near the areas of interest. Due to the nature of the electron microscopy techniques, the interaction volume of the electrons and the sample surface are bounded due to the limited penetration depths of the electrons, often less than 100 μm for SEM and less than 1 μm for TEM [106]. For this reason, part of the sample preparation requires the removal of sections of the material until the region of interest is within 100 μm of the free surface for SEM or the creation of thin films with thicknesses below 1 μm from the bulk sample for TEM. In both cases, the sample preparation process introduces one or two free surfaces near the region of interest for SEM or TEM, respectively.

The regions of a sample adjacent to free surfaces are physically less constrained than the regions within the bulk, thus prompting unique material behavior. A few works have studied the influence of free surfaces on dislocations and the overall mechanical strength and ductility. For example, Greer et al. suggested a "starvation model" that explains, for thin samples, that the rate of dislocation loss at the free surface can exceed the dislocation multiplication rate, resulting in a limited amount of dislocations available to carry out plastic deformation, consequently hardening the material [107, 108, 109]. Experimental

TEM evidence has indicated that the escape of dislocations through free surfaces can result in stress, strain and dislocation density gradients between the bulk and surface of the sample [110, 111, 112]. The global response of the specimen can be dominated by the surface regions when the sample dimensions are reduced. These results are supported by computational finite element method (FEM) analysis [113]. Furthermore, TEM has shown that free surfaces can directly influence the distribution of dislocation pileups near the free surface, which could consequently influence plastic response of the material when compared to the bulk [114].

Computational efforts have also been made to describe the effects of free surfaces on dislocation behavior. Atomistic studies have shown that, in thin samples, the image forces on dislocations near free surfaces are different and can cause the Peierls stresses for dislocation motion to be lower and dislocation mobility to be higher than in the bulk [115, 116, 117, 118, 119]. Similar conclusions have been drawn using molecular dynamics (MD) based methods [120, 121]. MD simulations have shown that the stress required for dislocation nucleation near free surfaces are lower than the bulk [122]. Dislocation dynamics (DD) simulations have also been implemented in order to capture image force effects on near-surface dislocations that assist in their fast ejection from the surface [123, 124]. Additionally, Crone et al. explained that voids, another source of free surfaces, in Al provided weaker strengthening effects than predicted by classical calculations of Lothe due to long-range image forces that act on the entire dislocation far away from the free surface [125, 126].

While free surface effects on dislocation behavior has been a topic of research for some time, the same treatment of free surfaces effects has not yet been extended to deformation twinning. One study by Datta et al., using first-principles, found that twins in Ni are harder to nucleate in thin films than the bulk due to the localization of the electronic structure near free surfaces [127]. Unlike dislocations, the dimensions of twins can be

grain-scale, resulting in extensive long-range changes in the local stress states [66]. Any effect of surfaces on local twin stresses can translate to a change in their propagation and growth behavior. The experimentally measured stresses and strains, via SEM or TEM, could be significantly different when compared to the interior of the bulk sample. Thus, the observations and analysis derived from near free surface techniques on twins in lab scale samples may not directly translatable to the bulk, making it difficult to predict the in service properties of Mg alloys.

1.5 Research objectives

The primary goal of this dissertation is to improve the understanding of how tensile twins develop around common microstructural features found in Mg alloys in order to advance the development of useful light-weight materials for future industrial applications. A mesoscale elasto-viscoplastic fast-Fourier-transform (EVP-FFT) model will be used to calculate the micromechanical fields that emerge in and around developing twins. The model is able to provide insight into how twins develop by predicting the development of internal stress fields and dislocation distributions. In order to accomplish this, the model will be advanced to account for a three-dimensional representation of twins, free surfaces, and spatial distribution of dislocation densities. Chapter 2 begins with an introduction and formulation of the EVP-FFT model used and the associated dislocation-density-based hardening law that has been integrated into the model. Chapter 3 and 4 discuss the insight gained into the AZ91 material system and how twins interact with $\beta-Mg_{17}Al_{12}$ precipitates that act as elastically hard obstacles. Next, Chapter 5 studies the development of twins in the presence of a free surface, the limit of an elastically soft medium. The limitations and challenges of surface characterization sample preparation techniques and the ability of computational methods to help deconvolute the effects of

free surfaces from the true internal stress fields is discussed. Lastly, in Chapter 6, closing remarks and recommendations for future work are presented.

In support of the aforementioned research objective, the following specific goals are proposed:

1. To isolate and identify twin-precipitate interactions that can influence the propagation and subsequent growth of twins. To date, the study of twin-precipitate interactions during the propagation stage of twinning has been largely ignored. In order to understand the wide range of effects that precipitates have on twins, a holistic approach to twinning has been considered, where twin propagation and twin growth are considered separately and sequentially. The mechanical response of the material can be tied to twinning behavior. Thus, a comprehensive understanding of how twins form starting from the early stages of deformation, when the twins are still thin, to the later stages, when the twins have thickened substantially, is needed in order to effectively predict and engineer Mg alloys for industrial applications.

2. To reveal the evolution of the spatial distribution of dislocation densities as twins develop. The migration of twin boundaries requires both adequate driving stresses and dislocations. Thus, it is important to consider both criterion in order to accurately assess the likelihood for twins to develop. Since the plastic deformation behavior consists of both slip and twinning deformation, it is critical to understand them both individually and their influences on each other in order to better improve the forming behavior of Mg alloys.

3. To identify key microstructural features, such as precipitate size and distribution, that control how twins propagate and how they thicken. Identifying these features can help guide the design of Mg alloys and heat treatment processes that optimize

the strength, ductility, and stability of Mg alloys for structural applications.

4. To reveal how free surfaces, commonly introduced during SEM and TEM sample preparation processes, can influence the experimentally observed dislocation accommodation of strain, twin morphology, and measured stresses and strains. Free surface effects in lab scale samples can lead to a misrepresentation of the bulk state of the material and ultimately influence our ability to understand and predict the material behavior in service. SEM and TEM techniques provide a majority of the microstructural observations and measurements of internal micromechanical fields that act as a basis for our understanding of materials. Thus, it is important to understand how free surfaces can influence the data collected by these characterization techniques. By qualitatively and quantitatively deconvoluting the internal stresses from free surface effects, a more accurate and realistic representation of the bulk material is achieved, which can greatly improve our ability to efficiently engineer useful Mg alloys.

Chapter 2

Crystal Plasticity-based Modeling (EVP-FFT)

2.1 Introduction

The results and analysis presented in this thesis have been made possible with the help a crystal-plasticity based elasto-viscoplastic fast-Fourier transform (EVP-FFT) model [27]. The modeling framework was inspired by the work of Moulinec and Soquet in 1994 [128, 129], who established a numerical method for computing the local and overall mechanical responses of nonlinear composites materials through an iterative algorithm that makes use of the Fourier transform of the stress and strain fields. The method they proposed was computationally efficient and made direct use of microstructural images taken from experimental techniques, without the need to mesh the microsture, an advantage over other popular techniques, namely Finite Element Methods (FEM). A disadvantage of the model, however, is that it operates on a periodic square grid, which makes it less general than FEM. This technique was later implemented into a mesoscale model to treat the deformation of polycrystalline materials under the elastic [130], rigid-

viscoplastic [131], and elasto-viscoplastic regimes [27]. The strength of the EVP-FFT model lies in its capability to take any arbitrary microstructure and calculate the intra-granular micromechanical fields, such as internal stresses and strains, that develop under arbitrary loading from initial elastic loading, through the elastoplastic transition, and the fully plastic regime [27]. The EVP-FFT model has since been further modified to treat twinning deformation [66, 132, 133], multi-phase material systems [8, 134, 135, 136], and free surfaces [137].

2.2 Elasto-ViscoPlastic Fast-Fourier-Transform formulation

Next, a summary of the EVP-FFT formulation is presented. For a more detailed description of the formulation, the reader is deferred to original paper by Lebensohn et al. [27]. The FFT solver operates on periodic unit cells and calculates the solution to the governing equations of equilibrium and compatibility with respect to the imposed boundary conditions and user defined error limits. The stresses at each Fourier point x are constitutively related to the elastic strains. Adopting a time-discretized form, the stresses can at time $t + \Delta t$ is written as

$$\sigma^{t+\Delta t}(x) = C(x) : \varepsilon^{e,t+\Delta t}(x) \tag{2.1}$$

where $\sigma(x)$ is the Cauchy stress tensor, $C(x)$ is the elastic stiffness tensor, and $\varepsilon^e(x)$ is the elastic strain tensor. The total strain, $\varepsilon(x)$, consists of the sum of $\varepsilon^e(x)$ and the total plastic strain,$\varepsilon^p(x)$. Accordingly, the elastic strain can be written as

$$\varepsilon^{e,t+\Delta t}(x) = (\varepsilon^{t+\Delta t}(x) - \varepsilon^{p,t+\Delta t}(x)) \tag{2.2}$$

The total plastic strain is comprised of contributions by slip and by twinning [66].

$$\varepsilon^{p,t+\Delta t}(x) = \varepsilon^{p,t}_{slip}(x) + \dot{\varepsilon}^{p}_{slip}(x,\sigma)\Delta t + \varepsilon^{p,t}_{twin}(x) + \Delta\varepsilon^{p}_{twin}(x) \tag{2.3}$$

Where $\dot{\varepsilon}^{p}_{slip}(x,\sigma)$ is the plastic strain-rate tensor by slip and $\Delta\varepsilon^{p}_{twin}(x)$ is an increment of the deformation twinning shear transformation strain. The plastic strain-rate by slip is a function of stress and is found by taking the sum of shear rates over the active slip systems

$$\dot{\varepsilon}^{p}_{slip}(x,\sigma) = \sum_{s=1}^{N} m^{s}(x)\dot{\gamma}^{s}(x) = \dot{\gamma_o}\sum_{s=1}^{N} m^{s}(x)\left(\frac{|m^{s}(x):\sigma(x)|}{\tau^{s}_{crit}(x)}\right)^{n} sgn\left(m^{s}(x):\sigma(x)\right) \tag{2.4}$$

In the above equation, N is the total number of active slip systems and $\dot{\gamma}$ is the shear rate tensors associated with slip system s. m is the symmetric part of the Schmid tensor

$$m^{s}(x) = \frac{1}{2}\left(b^{s}\otimes n^{s} + n^{s}\otimes b^{s}\right) \tag{2.5}$$

where b^s and n^s are the slip direction and slip plane normal of slip system s. $\dot{\gamma_o}$ is a reference slip rate, usually on the order of the applied strain rate, τ^{s}_{crit} is the critical resolved shear stress required to activate slip on system s, and n is the stress exponent (inverse of the strain-rate sensitivity exponent).

The model treats twinning explicitly, meaning the twin is formed in predefined region of the microstructure [66]. Twinning is achieved through the crystallographic reorientation of the twin domain by a 180° rotation about the twinning shear direction. Afterwards, the twinning transformation shear is incrementally applied until the characteristic twin shear, g^{twin}, of the material is fully developed over I^{twin}.

$$\Delta\varepsilon^{p}_{twin}(x) = m^{twin}(x)\Delta\gamma^{twin}(x) = m^{twin}(x)\frac{g^{twin}}{I^{twin}} \tag{2.6}$$

$m^{twin}(x)$ represents the Schmid tensor associated with the twinning system, such that

$$m^{twin}(x) = \frac{1}{2}\left(b^{twin} \otimes n^{twin} + n^{twin} \otimes b^{twin}\right) \tag{2.7}$$

where b^{twin} and n^{twin} is the twinning shear direction and twin plane normal, respectively. It should be noted here, that outside of the twin domain, $\varepsilon^{p}_{twin}(x)$ and $\Delta\varepsilon^{p}_{twin}(x)$ is always zero. During the twinning transformation process, the boundary conditions held constant and the system is relaxed to a new energetic minimum after each twin increment.

2.3 Simulation set-up

The simulations presented in this work are primarily concerned with studying the development of micromechanical fields around tensile twins in Mg and its alloys. The EVP-FFT framework has been extended to explicitly treat deformation twinning by Arul Kumar et al. [66]. In this approach, the twin domain is defined a priori and occurs first through a crystallographic reorientation of the twin volume by a 180° rotation about the twinning shear direction. Then, the characteristic twin shear is incrementally developed over I^{twin} steps along the twin plane in the twinning shear direction as an eigenstrain to complete the twinning trasnformation processes. The simulation is relaxed to an energetic minimum after each I^{twin} and I^{twin} is kept sufficiently large (i.e., 2000) in order to ensure numeric convergence. The twin-matrix boundary is simply defined as the border separating the twinned and untwinned domain.

In reality, twins are three dimensional and can vary significantly in size and shape

in all three directions. In order to study the early stages of twinning, when the twin has not yet grown significantly, a columnar microstructure is adopted in order simplify the microstructure. In this case, the twin shear direction and twin plane normal is kept in-plane, thus no gradients develop in the out-of-plane direction from the twinning process and the predicted fields are directly comparable with experimentally measured bright side views of twins [138]. The simulation cell size is chosen to be a minimum of 3 x 500 x 500 voxels, which is sufficiently large to reduce numerical aberrations from Gibbs phenomenon and allows for the isolated study in individual twin interactions with reasonable computational costs. The simulation cells typically include a buffer layer that is 50 voxels thick in each in-plane direction. A minimum buffer layer of 20 voxels is required in each direction in order to shield the central grain from the overlapping fields due to the periodic boundary conditions. In all present studies, the buffer layer consists of individually oriented voxels of the same phase as the parent matrix. The crystallographic orientations of the buffer layer voxels were sampled from a list of orientatations that represent a polycrystal with no texture.

In Chapter 5, a fully 3D ellipsoidal twin model is implemented with a simulation cell size of 174 x 174 x 174 voxels. Due to the massive simulation cell size, a balance was struck between achieving high resolution micromechanical fields and reasonable compuational costs (i.e., one month to complete one simulation). The simulation cell size was chosen to be sufficiently large to avoid significant influences from Gibbs phenomenon. In this work, a buffer layer of 24 voxels was used and was sufficiently large to avoid overlapping fields from periodic boundary conditions.

2.4 Dislocation-density-based hardening law

As ductile metals continue to plastically deform, the stress required to continue the deformation rises; this phenomenon is generally referred to as strain hardening or work hardening [139]. Work hardening can be divided into four stages, each in succession: Stage I, referred to as "easy glide", refers to the single slip of single crystals, stage II describes an athermal linear hardening stage that occurs through the interactions of glissile dislocations with forest dislocations, stage III is characterized by a decreasing hardening rate associated with the dynamic recovery of dislocations, and finally stage IV, which describes the small but sustained hardening that occurs at very large strains [140, 141]. Furthermore, the work hardening response of Mg can be further influenced and complicated by deformation twinning [38, 19]. Thus, a better understanding and modeling the work hardening response of materials that twin is important to accurately represent the deformation behavior of Mg over a wide range of strains.

Various hardening laws have been incorporated into models, such as Taylor-type [142, 143], Voce-type [144], and dislocation density (DD) based hardening [145, 33]. However, these models lacked the spatial resolution required to capture the effects of local grain-to-grain or twin-grain interactions and were inability to predict micromechanical field gradients across these boundaries that can influence the mechanical response [104, 64, 9, 21], microstructural evolution [75, 76], and texture evolution [22, 23]. Here, a dislocation-density-based constitutive hardening law developed by Beyerlein and Tomé in 2008 [145] has been incorporated into the full-field EVP-FFT framework [cite JMEP and AM]. The presented model is able to spatially resolve the evolution of dislocation densities and the CRSS of individual slip systems under deformation. The resulting heterogenous internal stresses and strain fields can then be predicted with intragranular resolution.

The CRSS for slip, τ^s_{crit} in Equation 2.4, for each slip system s is allowed to evolve as a function of strain rate and temperature. Below we provide a brief summary of the constitutive law formulation, however, for a more details approach we refer the reader to [145]. The resistance to slip on system s is determined through a sum of the following factors:

$$\tau^s_{crit} = \tau^s_o + \tau^s_{debris} + \tau^s_{forest} \tag{2.8}$$

where τ^s_o is the Peierls stress, which is an intrinsic resistance to slip, τ^s_{debris} represents the resistance to slip due to arrangements of dislocation substructures, and τ^s_{forest} captures the entangling of gliding dislocation by arrays of sessile dislocation lines. The creation of dislocation debris can involve the interactions between various slip modes and occurs through dislocation interactions that leave sessile dislocation segments. Accordingly, τ^s_{debris} in Equation 2.8 is expressed as

$$\tau^s_{debris} = K\mu b^s \sqrt{\rho^{debris}} \log \frac{1}{b^s \sqrt{\rho^{debris}}} \tag{2.9}$$

where K is a material constant values at 0.086 [146], b^s is the Burgers vector of slip systems s, μ is the shear modulus of the material, and ρ^{debris} is the total debris dislocation density. ρ^{debris} is calculated through the sum of debris contributed by each active slip system

$$\partial\rho^{debris} = q \sum_s f^s \frac{\partial \rho^{debris}_{rem}}{\partial \gamma^s} d\gamma^s \tag{2.10}$$

In the above, q is the rate coefficient for how quickly dislocation debris can accumulate and is set to 4 [145]. The density ρ^s_{rem} is the remnant dislocation density of each slip system that contributes to the formation of debris [147, 148]. f^s is a term that describes

debris dislocation storage rates, which increases with the amount of debris collected [149] as

$$f^s = A^s b^s \sqrt{\rho^{debris}} \tag{2.11}$$

In the above, A^s is related to the interaction length between dislocations and can be made to scale with temperature [150]. τ^s_{forest} in Equation 2.8 represents the resistance to slip due to arrays of forest dislocations that block dislocation glide [151, 152, 153] and can be written in the form

$$\tau^s_{forest} = \chi \mu b^s \sqrt{\rho^s} \tag{2.12}$$

Here, χ is a dislocation interaction coefficient and is set to 0.9 [154]. In this work, dislocations of slip system mode, such as basal, prismatic, or pyramidal, can only be hardened by forest dislocations from the same type. The stored forest dislocation densities evolve via a competition between dislocation generation term with coefficient k^s_1, that describes the trapping of gliding dislocations by forest dislocations and a thermally controlled annihilation term that represents the dynamic recovery of stored dislocations [155, 150], as follows:

$$\frac{\partial \rho^s}{\partial \gamma^s} = k^s_1 \sqrt{\rho^s} - k^s_2(\dot{\varepsilon}, T)\rho^s \tag{2.13}$$

where the coefficient for dynamic recover, k^s_2, is given by

$$\frac{k^s_2}{k^s_1} = \frac{\chi b^s}{g^s}\left(1 - \frac{kT}{D^s b^3}\ln\frac{\dot{\varepsilon}}{\dot{\varepsilon}_o}\right) \tag{2.14}$$

In the above, k, $\dot{\varepsilon}$, $\dot{\varepsilon}_0$, D^s, and g^s are the Boltzmann's constant, the strain rate at each Fourier point, a reference strain rate (set to be 10^7 1/s) [145], the drag stress [156, 157]

and a normalized activation energy [158] of slip system s.

Chapter 3

Twinning pathways enabled by precipitates in AZ91

3.1 Introduction

Magnesium (Mg) alloys are exceptionally lightweight structural metals (density, $\rho \approx 1.74 \frac{g}{cm^3}$), being approximately 30% lighter than aluminum and 75% lighter than steel. This property alone makes them highly attractive candidates for many structural applications where lighter components can mean greater energy efficiency and lower costs [12, 11]. Furthermore, Mg is abundant and recyclable, making it environmentally sustainable [11]. However, many common Mg alloys are not sufficiently strong for typical industrial applications since their tensile yield strengths lie between 80-120 MPa [159][35], far below the tensile yield strength of 350 MPa of high-strength steels [14] and below 100-240 MPa that of most aluminum 6000 series alloys [13]. In order to increase their strengths, various mechanisms have been employed to restrict the motion of dislocation glide in Mg alloys. A recent study showed that Mg alloys containing Zn and Ca can form Guinier-Preston (GP) zones to achieve alloys whose combination of ductility and strength

are comparable to aluminum 6000 series alloys [15]. More commonly, precipitates can be dispersed throughout the matrix and grain boundaries that block dislocation slip, leading to reported increases in yield strengths up to 156-324 MPa [10].

A number of studies have been carried out to understand slip-precipitate interactions. It is commonly found that precipitates interact with dislocations by acting as hard non-shearable obstacles that block the motion of the dislocations through the matrix grain [99, 36]. Accordingly, the increase in the stress required for plastic flow has been approximated by Orowan looping, where the precipitate size, shape, habit plane and spacing play important roles in determining the amount of strengthening provided [160, 82, 161, 81, 4, 97]. Alternatively, some studies have investigated shearable precipitates, wherein the precipitate displayed signs of being sheared by impinging dislocations [161, 162, 163, 164]. Precipitate shearing tends to occur when the shear planes of the precipitate and matrix grain are well aligned, a condition that happens more often for basal a dislocations than non-basal dislocations in Mg alloys [161]. In addition to slip, Mg alloys also commonly deform by twinning [54]. Twinning deformation occurs through the coordinated directional shearing of a subregion of a grain along a particular crystallographic twin plane. The resulting twin domain is reoriented with respect to the parent grain, such that the parent and twin have a mirror symmetry across the twin plane [54]. Twinning introduces sub-grain domains and the associated boundaries in the microstructure, as well as heterogeneous stress and strain fields within and in the vicinity of twin domains [66, 165]. In AZ91, $\{10\bar{1}2\}$ tensile twinning deformation can occur at room temperature and large twin volume fractions up to 35% have been observed by 2% strain [100]. Due to the severe consequences of twinning on the microstructure and local micromechanical fields, the structural properties of Mg alloys are strongly dependent on their twinning behavior. Thus, understanding interactions between twins and precipitates is paramount to designing precipitate-rich Mg alloys with high strength.

In contrast to slip, twin-precipitate interactions have received less attention. Unlike slip, twins are three-dimensional domains that form through a sequence of steps, including nucleation, propagation and thickening of the twin domain [54]. The twin-precipitate interactions during each of these steps are unique and important for determining the development of the overall twinned microstructure and mechanical properties of the alloy. In general, experimental studies have found the volume fraction of twins remain consistent, regardless of precipitate volume fractions [42, 90]. However, the presence of precipitates correlate well with an increase in the density of twins and a decrease in twin size, implying that precipitates can enhance multiple twin formation while suppressing twin thickening [100, 91, 95, 166].

Twin-precipitate interactions that involve twin nucleation have been investigated by computational methods. Tang et al. used molecular dynamics (MD) simulations to show that twin-precipitate interaction sites can initiate twinning dislocation loops that lead to a reduction in the resolved shear stress needed to nucleate twinning dislocation partials under strain rates of 106/s at 283 K [167]. Using MD simulations, Fan et al. showed that basal dislocations and stacking faults can nucleate at the twin-precipitate interfaces causing local plastic relaxation [98]. As a result, they were able to rank the effectiveness of precipitate shapes on hardening, showing that spheres have the strongest hardening, followed by plates and then rods [98].

A majority of studies in the literature investigate twin-precipitate interactions that affect twin thickening, where a distribution of precipitates block the lateral migration of the twin boundary [160, 97, 167, 98]. Some models have been proposed that have treated twinning synonymously with slip and described the strengthening by Orowan bowing of twinning dislocation partials around the precipitates [95, 166, 25]. Barnett et al. extended this idea by representing the twinning dislocations as a wall of super-dislocations, which yielded closer approximations to experimentally observed values of strengthening [96].

This model was later supported by dislocation-dynamics (DD) simulations [94]. Jain et al. used transmission electron microscopy (TEM) combined with visco-plastic self-consistent modeling to study the role of long-range elastic backstresses developed by precipitates on tensile twins [42]. Liu et al. used crystal plasticity phase-field simulations to show that precipitate size and habit-plane alignment with the twin boundary play critical roles on the resolved shear stress required for twin thickening [97]. Recently, by employing crystal plasticity based finite element method, Siska et al. simulated the twin-precipitate interaction in a Mg alloy to study the effect of precipitates on twin boundary migration [39]. They showed that precipitates can indirectly suppress the twin thickening process by hardening the slip modes that would normally relax stresses around the twin [39].

Unlike twin-precipitate interactions involving the interaction between precipitates and migrating twin boundaries, considerably less studies focus on the effects of interactions of twin-tips and precipitates during propagation. The ability of precipitates to potentially divert, blunt, or aid the nucleation of new twins near the interaction site can affect twinning microstructure (e.g., morphology and variant selection), and the accommodation of plasticity. Understanding how these interactions progress in time is difficult to identify with local post-mortem analyses, especially when information is collected from many different samples. To gain statistically significant information in this regard, most recently Xie et al. [5] investigated the effect of precipitates on different stages of $\{10\bar{1}2\}$ tensile twinning in a Mg-9 wt.% Al alloy micropillar using precision electron diffraction. They used a sample that contained a heterogeneous distribution of basal type precipitates, facilitating the ability to capture the different stages of twin-precipitates interactions within the same scanned area. In doing so, they were able to isolate twin-precipitate interactions during propagation in a region where twin thickening was limited. They observed that basal-plate precipitates can arrest propagating twin tips but seem to allow

new twins to nucleate on the other side of the precipitate. They considered regions in the interior volume of the micropillar in addition to near the surface and found that precipitates tend to promote multiple twin formation, in line with observations reported in the literature [100, 91, 95, 166].

The focus of this study is to elucidate the interactions between twin-tips and precipitates that control the microstructural evolution during the propagation stage of twinning. A full-field elasto visco-plastic fast Fourier transform (EVP-FFT) model is used to calculate the local stress fields around twin/precipitate configurations involving commonly observed basal-type precipitates and the $\{10\bar{1}2\}$ tensile twin in AZ91 alloy [5, 84]. The twin plane resolved shear stress (TRSS) in the vicinity of the twin boundary, twin tip, and around the precipitates are used to determine the local driving forces available for different bypass mechanisms and gain some insight into which one is likely to occur. For most cases, the twin thickness is much finer than the length of the precipitate.

The impingement of a single propagating twin near the center and edges of plate-shaped basal precipitates is simulated. The thickness of the precipitate, relative to the thickness of the twin, is shown to have a strong effect on the likely outcome of the interaction or bypass mechanism. The findings support that central-impingement is more effective at blocking twin propagation than edge-impingement. In both cases, highly localized twin stresses develop around the impingement site that can serve as sites for new twins to nucleate. These results may help to identify cases in which complex network structures of twins that apparently "cross" precipitates can emerge. To continue propagating, it is not likely that the twin would thicken or migrate around the precipitate but would rather reform on the other side of the precipitate. The effects of relative precipitate thickness on the number, location and variant of twins that can form in this situation are investigated.

3.2 Model set-up

In this work, the material system is the AZ91 Mg alloy containing Mg17Al12 precipitates. AZ91 has a hexagonal close-packed (HCP) crystal structure and the elastic constants C_{11}, C_{12}, C_{13}, C_{33} and C_{44} are 59.75, 23.24, 21.7, 61.7 and 16.39 GPa, respectively [168]. The initial CRSS for AZ91 for the prismatic $\langle a \rangle$, basal $\langle a \rangle$ and pyramidal-type I $\langle c + a \rangle$ slip modes were constant throughout the simulation and set to 100, 35, and 160 MPa, respectively [35]. Only the twinning shear transformation is simulated, with no pre- or post-twin straining. Thus, strain hardening was not considered since it is not expected to significantly influence the twinning shear transformation process and allows for easier interpretation of the twin-precipitate interaction induced micromechanical fields. The $Mg_{17}Al_{12}$ precipitate has a body-centered cubic (BCC) crystal structure, and the elastic constants C_{11}, C_{12}, and C_{44} are 86.8, 29.0, and 20.0 GPa, respectively [169]. In the simulation, the precipitate is treated as an elastically deforming body. It has been observed experimentally that even when twins fully engulf these precipitates they do not shear or plastically deform [99, 170].

The simulation size is 3 x 600 x 600 voxels and consists of a 50-voxel thick buffer layer (dark blue) that encompasses the parent grain. The buffer layer approximates the response of a polycrystalline medium with a uniform distribution of crystal orientations (i.e., random texture), and is sufficiently thick to prevent the micromechanical fields from overlapping due to the periodic boundary conditions. The simulations are designed to elucidate the influence of $Mg_{17}Al_{12}$ basal precipitates on $\{10\bar{1}2\}$ tensile twin development within AZ91 alloy. Figure 3.1 illustrates the periodic simulation cell in all simulations, depicting a tensile twin (red) lamella impinging on a $Mg_{17}Al_{12}$ β-phase precipitate (orange) within the center of a parent grain (light blue).

The crystallographic orientation of the parent grain, in the Bunge convention, is

$(0°, 90°, 0°)$, which aligns its c-axis with the y-direction. The orientation of the parent grain is represented by the hexagonal inset in the top left, Figure 3.1a. Based on the experimental observations, the basal precipitate assumes a thin plate-shape and lies on a habit plane that is parallel to the basal plane of the matrix grain [84, 87, 88]. The precipitate and the matrix share the Potter orientation relationship, commonly observed in electron microscopy, given by $(0001)_{Mg}$ 2° from $(011)_{\beta}$, $[2\overline{1}\overline{1}0]_{Mg}$ // $[1\overline{1}1]_{\beta}$], and $(01\overline{1}1)_{Mg}$ // $(110)_{\beta}$ [99, 84, 88]. Accordingly, the crystallographic orientation of the precipitate for the selected parent grain orientation is given by $(39.23°, 114°, 63.43°)$, in the Bunge convention. The angle of incidence of the twin on the basal precipitate depends on the twin type and its variant. In this work, the variant explicitly simulated is the $(01\overline{1}2)[0\overline{1}11]$ tensile twin, with both its twin plane normal and twin shear direction lying in the y-z plane. In this way, there is no out-of-plane twinning shear in the x-y and x-z planes, and thus allowing for a 2D model setup and lower computational costs. The selection of another $\{10\overline{1}2\}$ tensile twin variant or orientation of the precipitate within the Potter orientation relationship is not expected to yield significantly different results.

With periodic boundary conditions, the microstructure is columnar with the cross-section shown in Figure 3.1a. While a 3D simulation is possible with the EVP-FFT model, it is not necessary since the simplified 2D microstructure can reasonably approximate the majority of twin-precipitate impingement events. More importantly, the crystallography of the $\{10\overline{1}2\}$ tensile twin and basal precipitates selected for this work permits simulating the interactions in 2D. Typically, little is known about the twin geometry in the out-of-plane of the viewing surface, as these are not readily described in the literature due to the 2D nature of electron-microscopy-based techniques. For these reasons, the 2D version is valid, with the added benefit of permitting more attention to be paid to the relative size of the twin with respect to the precipitate dimensions in the in-plane direction. The results can be extrapolated in the out-of-plane directions where the relative twin thickness and

the out-of-plane dimension of the precipitate would be important.

The twin thickness, t_t, and precipitate thickness, t_p, are shown in Figure 3.1a. The geometry of the plate-shaped precipitates is such that it is large in two dimensions (z- and x-directions) and can be approximated as infinite in comparison to the thickness of newly propagating twins in this studying. Thus, the simplified 2D model is sufficient, as modeling the third infinitely large dimension (x-direction) is not expected to change the trends observed in this work. The small dimension of the precipitate (y-direction) is varied to demonstrate how the precipitate thickness can influence twin propagation. The EVP-FFT formulation does not intrinsically contain any physical length scales, and thus relative sizes between the twin-tip thickness and precipitate thickness are used to correlate with experimentally observed microstructures. We have chosen a twin thickness of 22 voxels and a range of precipitate thicknesses from 3 to 88 voxels, resulting in relative precipitate thicknesses with respect to twin-tip thickness that range from $0.14-4.0$. In the micrographs presented in the literature, it can be observed that precipitate thicknesses range from $20-400$ nm [99, 5, 101]. By considering a large precipitate thickness of 400 nm represented by 88 voxels, our simulations would correspond with precipitate thicknesses in the range of $13.6-400$ nm and a twin thickness of 100 nm, within reasonable approximations of early-stage twin propagation.

In the calculations that follow, focus is given to the interaction of the twin tip with precipitates during twin propagation. Newly formed twins that first propagate across the twin-free grain are usually thin compared to the grain size and plate-shape precipitates. Thus, the twin is more likely to impinge somewhere in the central portion of the precipitate, away from the edges. Here two general, yet distinct, situations are presented: central impingement and near-edge impingement.

3.3 Precipitate effects on twin stresses

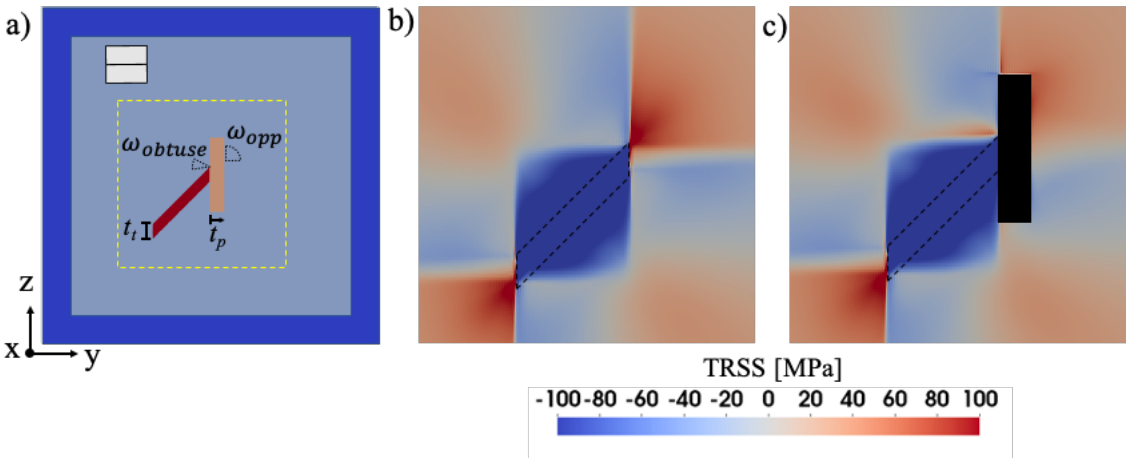

Figure 3.1: The calculated TRSS fields without and with a basal-plate $Mg_{17}Al_{12}$ precipitate. a) Schematic of the simulation set-up. A polycrystalline buffer layer surrounds the parent grain of AZ91 Mg alloy. The $Mg_{17}Al_{12}$ precipitate lies on the basal plane of the parent grain with a $\{10\bar{1}2\}$ tensile twin impinging on it. The orientation of the parent grain is illustrated by the hexagonal inset. Peak TRSS values develop in regions ω_{opp} and ω_{obtuse} are marked with black dotted lines on both sides of the precipitate. b) The TRSS field when a twin develops without a precipitate nearby. c) The TRSS field when a twin impinges on a precipitate. The twin boundary is outlined in dashed black lines.

The local stress state around the twin, after it has impinged on a precipitate is used to infer how the precipitate would affect twin propagation and thickening. When a twin develops inside a crystal, due to the crystallographic reorientation and local shearing imposed by the twin, the twin alters the stress state of the crystal compared to the twin-free state. Figure 3.1a shows the twin and a precipitate lying on the basal plane and oriented such that the twin tip would impinge on the center of the precipitate. The precipitate is five times longer than its thickness, and the twin thickness is equal to the thickness of the precipitate.

Figures 3.1b and 3.1c compare the calculated twinning resolved shear stress (TRSS) fields without and with the precipitate, respectively. This stress component is the stress state projected onto the twin plane along the twinning shear direction to determine the

driving force for twin development, including propagation and thickening. A positive TRSS supports twin propagation and thickening, while a negative TRSS acts against it (an anti-twinning stress) [54]. In the precipitate-free case, TRSS of about +100 MPa localize in a small region ahead of the twin tip, favoring twin-tip propagation. Along the twin boundary, however, TRSS of about −125 MPa develop, which hinders twin thickening. Figure 3.1c shows that with a hard precipitate, the forward stresses ahead of the twin-tip, in the region ω_{opp}, decrease by approximately 25% to approximately +75 MPa, compared to the precipitate-free case. Additionally, the high stress region in ω_{opp} becomes less localized. The anti-twinning stresses along the twin boundary, however, are similar to the precipitate-free case. With the precipitate, in order for the twin to continue propagation, it would have to reform on the other side of the precipitate. Compared to continued twin-tip propagation without the precipitate, a larger critical stress is clearly required. With the lower driving stress and requirement to reform a new twin in ω_{opp} and backstresses along the twin boundary, the precipitate hinders the twin from both propagating and thickening.

In addition to ω_{opp}, located on the opposite side of the precipitate from where the twin impinges, another highly localized TRSS is generated in a region at ω_{obtuse}, where the twin and precipitate come together at an obtuse angle, shown in Figure 3.1a. Here, the TRSS reaches approximately +65 MPa, compared to −20 MPa in the same region without the precipitate. These results are qualitatively in line with trends observed in recent work by Siska et al. [39], who used Finite Element Methods (FEM) to study tensile twins bounded between basal precipitates in AZ91 alloy. Since the precipitates are elastically deforming bodies that do not twin or shear, twinning in the matrix grain can only continue through the nucleation of a new twin in ω_{opp} or ω_{obtuse} , or through the thickening of the initial twin [99, 82, 171]. We discuss these three possibilities below.

3.4 Formation of multiple twin variants

Twin variants	b	n
V1	$[\bar{1}011]$	$[10\bar{1}2]$
V2*	$[0\bar{1}11]$	$[01\bar{1}2]$
V3	$[1\bar{1}01]$	$[\bar{1}102]$
V1a	$[10\bar{1}1]$	$[\bar{1}012]$
V2a	$[01\bar{1}1]$	$[0\bar{1}12]$
V3a	$[\bar{1}101]$	$[1\bar{1}02]$

Table 3.1: Crystallographic twin shear direction, b, and twin plane normal, n, of the $\{10\bar{1}2\}$ tensile twin variants. The variants V1a, V2a and V3a are the co-zone variants of variants V1, V2, and V3, respectively. * Denotes the primary twin variant which is explicitly simulated in this work.

The foregoing TRSS fields correspond to a single twin variant impinging on the precipitate. However, it is also commonly observed that multiple variants can develop in grains of deformed precipitate-strengthened Mg alloys [90, 95, 5, 172]. To analyze the possibility for the formation of multiple variants as a result of the twin/precipitate interaction, we consider the same tensorial stress field generated by the twin lamella and precipitate as before, but calculate TRSS fields corresponding to all six crystallographic $\{10\bar{1}2\}$ tensile twin variants, see Table 1, where V2 is the primary variant which is explicitly simulated in this work. Each of the twin variants are related to each other by rotation symmetry, and thus, the arbitrary choice of any one of the twin variants as the primary variant would result in equivalent resolved shear stresses among the other five variants. V2 was selected to be the primary twin variant because its twin plane normal and twin shear direction lie in-plane (in the Y-Z plane). The TRSS of each of the six variants, V, is calculated as $m^V : \sigma$, where m^V is the symmetric part of $b^V \otimes n^V$, and b^V and n^V are the shear direction and plane normal direction of each twin variant, respectively.

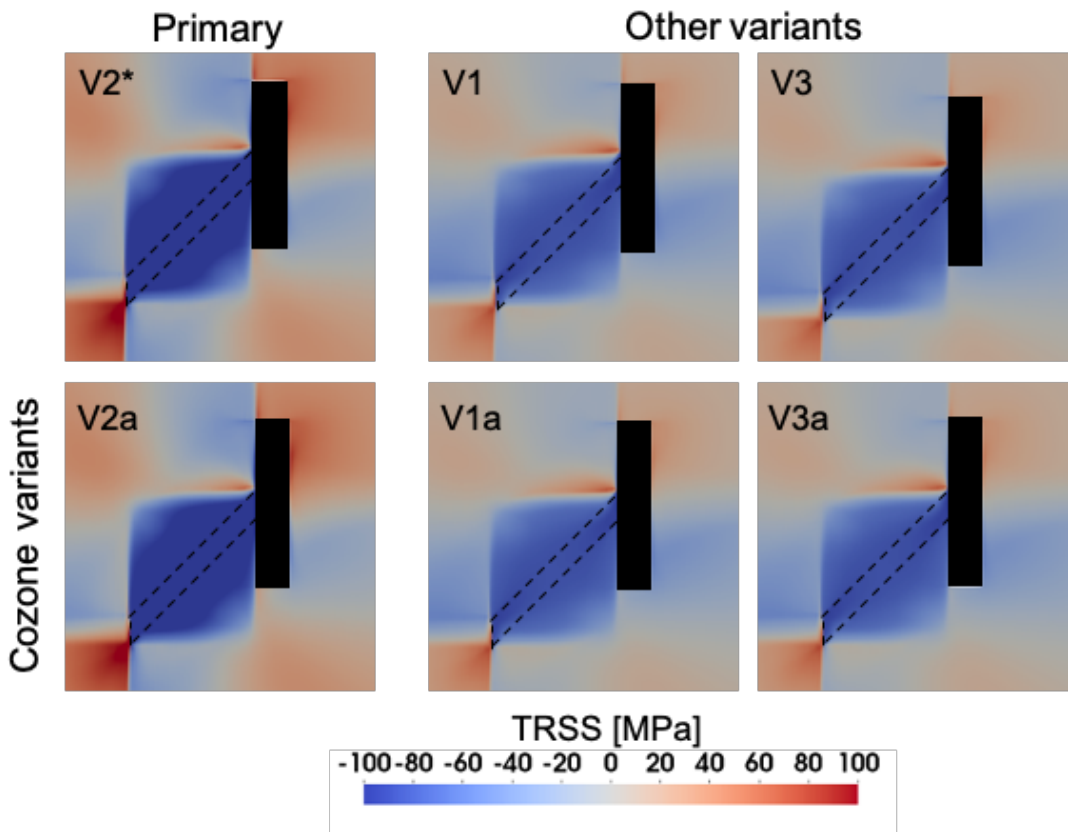

Figure 3.2: TRSS fields for three tensile twin variants (top row) and their respective cozone variants (bottom row) due to the impingement of tensile twin variant V2 on a basal plate precipitate. The crystallographic details of these variants are listed in Table 1. * Denotes the primary twin variant which is explicitly simulated in this work.

Figure 3.2 presents these TRSS fields for all six tensile twin variants. The top row shows the TRSS fields for variants V1, V2 and V3 and the bottom row, their respective cozone variants. The TRSS fields of cozone variant pairs (i.e., V2 and V2a) are nearly identical. The TRSS fields of all variants experience qualitatively similar trends to that observed for V2. Among all, twin V2 and its cozone variant experience the largest intensities of backstresses near the twin boundary and highest stresses ahead of the twin tip at ω_{opp}. The formation of another twin in ω_{opp} is, therefore, likely to be of the same variant as the initial variant or its cozone variant (V2 and V2a in this case). If a second twin of the same V2 variant were to form at ω_{opp}, the impinging twin would appear to

propagate straight "across" the precipitate. On the other hand, if the variant of this second twin is the cozone variant V2a, the twin would seem to kink. Such a structure associated with twin/precipitate junctions has been observed experimentally and referred to as a zig-zagged chain or quilt-like structure [5]. Interestingly, a stress concentration has developed on the side of the twin/precipitate junction where the twin and precipitate intersect at an obtuse angle, at ω_{obtuse}. Analysis of the TRSS in this region finds them to be positive and heightened above the average stress in the grain. Further, in the ω_{obtuse} region, the other variants exhibit higher TRSS compared to the impinging twin and its cozone variant, suggesting that a variant other than V2 or V2a could emanate from the impingement site. These calculations suggest that the interaction between a single impinging twin and a precipitate can trigger the development of other twin variants on both sides of the precipitate, aiding in the development of a complex 3D twin network structure.

3.5 Effect of precipitate width on multiple twin formation

Prior work had discussed the importance of the twin thickness relative to the precipitate length [99], but calculations of the TRSS fields indicates that the thickness of the precipitate, t_P, should also be important. By comparing Figure 3.1b and 3.1c, we observe a shielding effect on the TRSS for the twin (V2) in ω_{opp} provided by the precipitate. It is the result of the elastically deforming rigid precipitate resisting the shear of the impinging twin and limiting the development of stress concentrations in the matrix on the other side of the precipitate. The extent of shielding is related to precipitate thickness t_p.

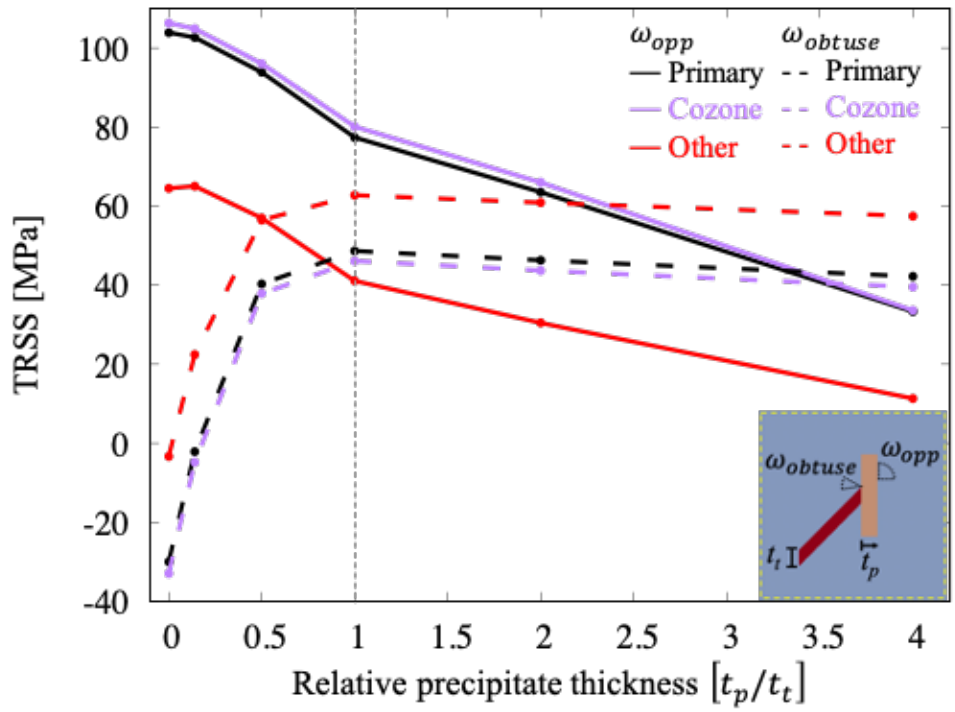

Figure 3.3: The change in average TRSS taken in ω_{obtuse} and ω_{opp} with the precipitate thickness, t_P, normalized by the twin thickness t_t. The regions ω_{obtuse} and ω_{opp} are illustrated in the figure inset.

To examine the effect of t_p, we study the local driving stresses on either the opposing side in the line of twinning shear, in ω_{opp}, or the same side as the twin/precipitate junction, in ω_{obtuse}. These are the two sites where the twin is most likely to form after impinging the precipitate. We carried out a series of twin-precipitate interaction calculations for various precipitate thicknesses ranging from 0.14 to four times the thickness of the twin, t_t. Figure 3.3 shows the variation in the averaged TRSS in ω_{opp} (solid lines) and in ω_{obtuse} (dashed lines) with varying $\frac{t_p}{t_t}$. The TRSS is averaged in a quarter circle region in ω_{opp} and in a conical region in ω_{obtuse}, as schematically shown in the Figure 3.3 inset. The values of the primary twin variant (V2) and its covariant (V2a) are marked in black and purple, respectively. Within both ω_{obtuse} and ω_{opp}, the TRSS for the primary and cozone variant have similar values, within 5 MPa of each other. The TRSS values of all the

other variants are nearly identical (within 5 MPa of each other), and thus, are averaged together and shown in red.

The results in Figure 3.3 show that as the relative twin thickness increases beyond the precipitate thickness (i.e., $\frac{t_p}{t_t} < 1.0$), then the twin is more likely to reform on the other side of the precipitate, and the precipitate has less shielding power. The average TRSS for V2 and V2a in ω_{opp} are higher than the average TRSS of all the variants in ω_{obtuse} when $\frac{t_p}{t_t} < 1.0$. Furthermore, the average TRSS values for the V2 and V2a variants range from about 75-110 MPa and are higher than the average TRSS of all the other variants by about 30 MPa in this range, indicating that a new twin would preferably form in ω_{opp} rather than ω_{obtuse} and would likely to be the same variant or the cozone variant as the impinging twin. In appearance, the twin would seems to "cross" the precipitate, although it is more like "hopping" over the precipitate, since the precipitate itself does not twin [99, 173]. This scenario is similar to the apparent crossing reported in studies of twin-twin interactions [173, 174].

Figure 3.3 indicates the reverse trend for wider precipitates, as $\frac{t_p}{t_t} > 1.0$. As the relative twin thickness decreases further below the precipitate thickness the impinging twin is more likely to "rebound" from the precipitate, producing another variant on the same side as the twin/precipitate junction. When $\frac{t_p}{t_t} \geq 2$, the average TRSS of V2 and V2a in ω_{opp} and the average TRSS of all other variants in ω_{obtuse} are about equal, implying that nucleation on either site is equally likely. In contrast with ω_{opp}, in ω_{obtuse} the average TRSS for the primary twin and its cozone variant are lower than the other twin variants by about 15 MPa. Here, instead, the twin variants other than the primary variant and its cozone would be favored. In actuality, since the thicknesses of basal precipitates rarely exceed 50 nm [160, 171, 83] and the thickness of newly propagating twins near the twin tip are usually larger [5], it is expected that a twin nucleation would occur in ω_{opp}. The nucleation of a twin on the obtuse angle side is also consistent with previous reports of

twin-grain boundary interactions [175].

3.6 Staggered twin chain formation

The highly stressed region on the side of the precipitate opposite from the twin tip is extensive, being several times the twin thickness in length, making the exact location of the twin nucleation site difficult to observe. We examine the TRSS along a line Z' in the parent matrix of the precipitate/matrix boundary opposite from the twin/precipitate interaction site, seen in the Figure 3.4a inset. In Figure 3.4a, the vertical axis represents the position along Z' normalized by t_t, where Z' is centered along the line of twin shear. We observe that the location of the peak TRSS is offset from the line of twin shear by $0.41t_t$. In the example shown in the figure inset, the precipitate thickness equals the twin thickness. Repeating the calculation for other sizes of precipitates reveals that the location of peak TRSS varies with the precipitate thickness. Figure 3.4b presents the offset position of the maximum TRSS for various precipitate thicknesses, normalized by t_t. For reference, the normalized peak TRSS position for a precipitate free case is presented in dashed lines, measured at distances from twin tip equal to the various precipitate thickness studied here. Even without the precipitate (i.e., $\frac{t_p}{t_t} = 0$), the maximum TRSS at the twin front is not directly aligned with the twin shear direction. Instead, it is offset from the line of shear by $0.45t_t$. It draws closer to the line of shear at further distances away from the twin tip, eventually reaching it at distances exceeding $2t_t$. The presence of the precipitate extends the peak offset, suggesting that the location where an outgoing twin would be likely to form on the other side of the precipitate would be misaligned from line of shear from the incoming twin. The degree of misalignment increases with decreasing t_p.

If the primary twin variant is nucleated at the offset location, the twin may appear

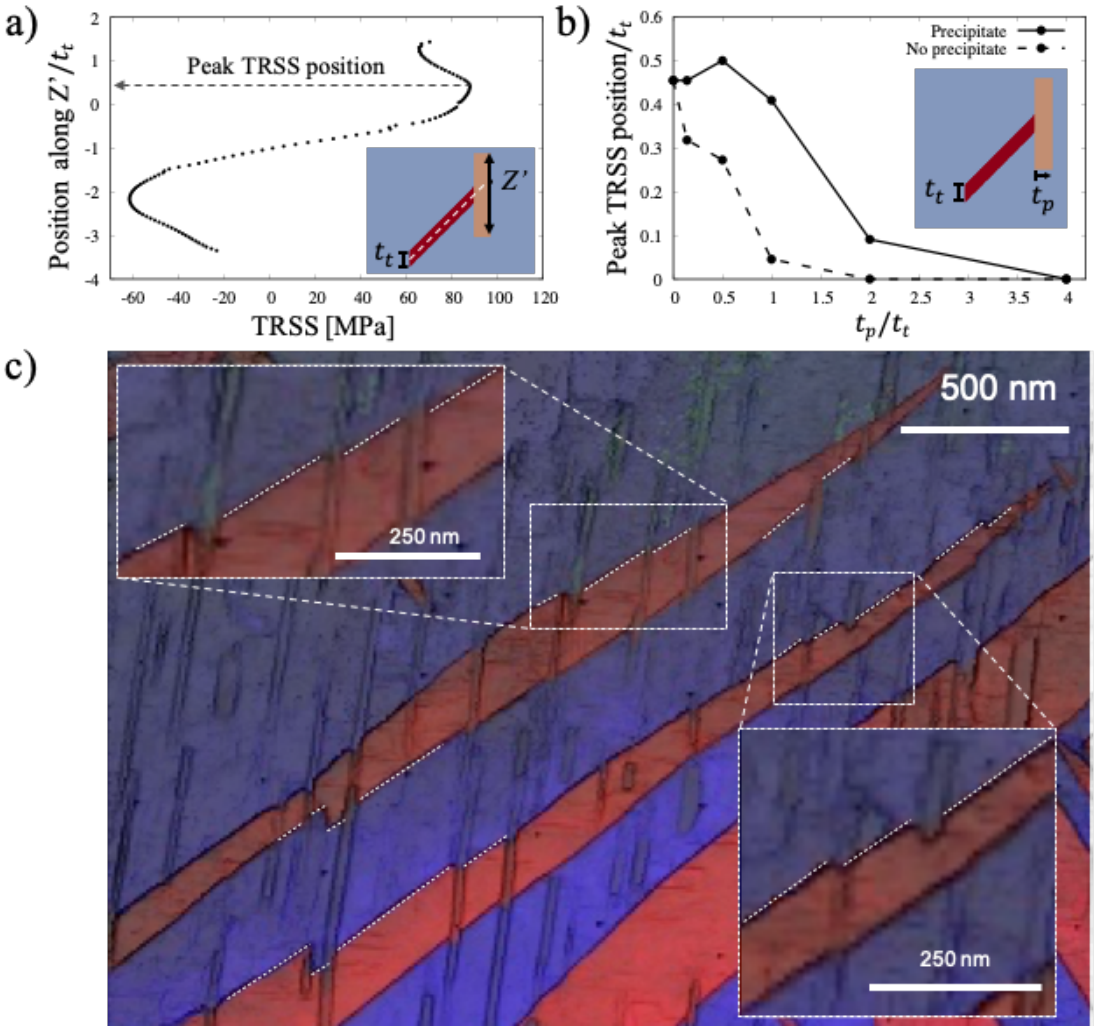

Figure 3.4: a) TRSS profile measured along Z' normalized by the twin thickness. Z' lies in the parent matrix along the precipitate-matrix boundary opposite from the impinging twin tip and is centered along the line of twin shear, as shown in the figure inset. Here, the precipitate thickness is equal the twin thickness. The figure shows that the peak TRSS is vertically offset from the line of twin shear. b) The normalized offset of the peak TRSS for various precipitate thicknesses is shown in solid lines. The dashed line shows the normalized offset of the peak TRSS for a precipitate-free case measured along vertical lines from twin tip. c) Precision Electron Diffraction (PED) micrograph of Mg-9Al micropillar sample exemplifying some adjacent twin boundaries that are offset from each other, forming staggered twin formations (highlighted by white dashed lines). The green circle shows an example of cozone twin variants formation at the precipitate interaction site. The micrograph was adopted and modified from Figure 1(d) of Xie et al. [5] with permission from Elsevier.

to "cross" the precipitate and the microstructure may develop a series of staggered twin chains disrupted by precipitates. In Figure 3.4c, an enlarged partial Precision Electron Diffraction (PED) micrograph taken from Figure 1(d) of Xie et al. [5] exhibits staggered twin chains in Mg-9Al that support these findings. The present numerical results are consistent with other experimental reports of twin-precipitate interactions as well, where staggered twin structures have been observed in microscopy [99, 100].

Since the TRSS fields of the primary twin and its cozone variant are nearly identical, the outgoing twin can be the same variant as the primary twin or its cozone variant or possibly both. The ability to nucleate either variant may lead to the development of the complex network structure of twins in a series of events. First, the nucleation of a few initial twins can propagate and interact with precipitates, inducing subsequent twins to nucleate. The subsequent twin can be the same variant, resulting in long twin chains. On the other hand, the cozone variant can nucleate, resulting in zig-zagged twin structures like the one seen in the green circle in Figure 3.4c [5]. This series of event could be responsible for the development of profuse interconnected twinned structures, rather than the independent nucleation of many individual twins.

3.7 Effect of precipitates on twin thickening

Figure 3.1b and 3.1c shows the backstresses that develop along the twin boundary. Here the backstress at a given point refers specifically to the difference between the TRSS before and after the twin developed. Particularly when they are negative, they represent an anti-twinning stress. Because these backstresses can be strong in the vicinity of the twin boundaries, thickening of the twin, by twin boundary migration is not favored [66, 176, 64]. Twin boundary migration would require sufficiently high applied stresses and would be favored in the event that propagation at the twin-tip has been blunted due

to obstacles, like precipitates and grain boundaries.

To study the effect of precipitates on twin boundary migration, in Figure 3.5 we show the volumetric average of TRSS in the twin plotted as a function of normalized distance, $\frac{d}{t_t}$, moving away from the impinging twin tip, see figure inset. For comparison, the TRSS profile for the precipitate-free case presented in black. The results indicate that, as expected, the precipitate causes the backstresses in the twin domain to intensify locally at the twin tip-precipitate interaction site, for instance decreases the TRSS from -128 to -133 MPa.

This precipitate effect on the backstress decreases when moving away from the interaction site, and eventually the TRSS reaches nearly -130 MPa corresponding to the precipitate-free case. This result suggests that twin thickening is restricted by precipitates, a trend that is consistent with several experimental observations [97, 90, 167, 177]. Prior experimental studies have shown the twin boundary migration is impeded by the presence of the elastically hard precipitates and must bow around the precipitates for the twin to thicken. Most recently, using crystal plasticity-based phase field model, Liu et al. [97] modeled the pinning of a twin boundary at precipitates and captured the increase in stress required for twin thickening. In the present work, a single twin-tip interaction is investigated rather than the cumulative interactions of twin boundary with multiple precipitates. Both cases, reveal that precipitates restrict twin thickening; however, the twin-tip effect is very localized near the interaction site.

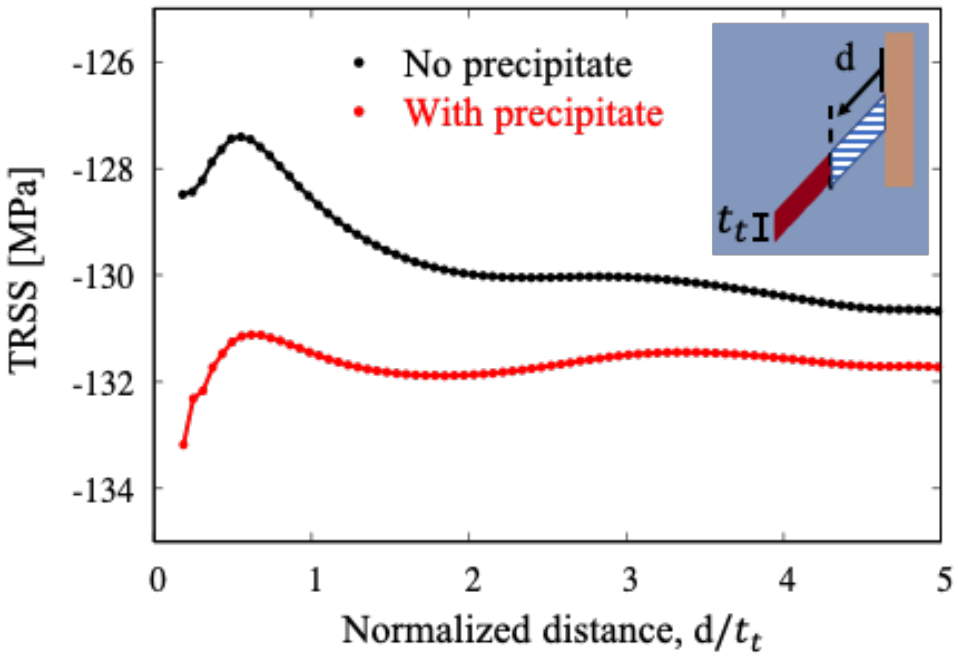

Figure 3.5: The red lines show the volumetric average TRSS in the twin domain as a function of distance, d, moving away from the twin/precipitate junction, as schematically shown in the figure inset. The black lines correspond to the TRSS with no precipitate present and d is measured from the twin tip. In both cases, the d is normalized by the twin thickness, t_t.

3.8 Effect of the twin-precipitate interacion site on twin network structure formation

Thus far, only the case in which the twin impinges near or at the center of the precipitate, far away from its edges, has been considered. The centeral impingement scenario is statistically more likely than edge-impingement when the impinging twin is thinner than the length of the precipitate. Yet the chance the twin could hit at the end of the precipitate is non-negligible and such an interaction could yield a different outcome since a complex stress state is generated at the end of the precipitate. To study this case, calculations are performed in the event that the twin intersects the precipitate at one of its ends, as illustrated in Figure 3.6a. Figure 3.6b shows the resulting TRSS field,

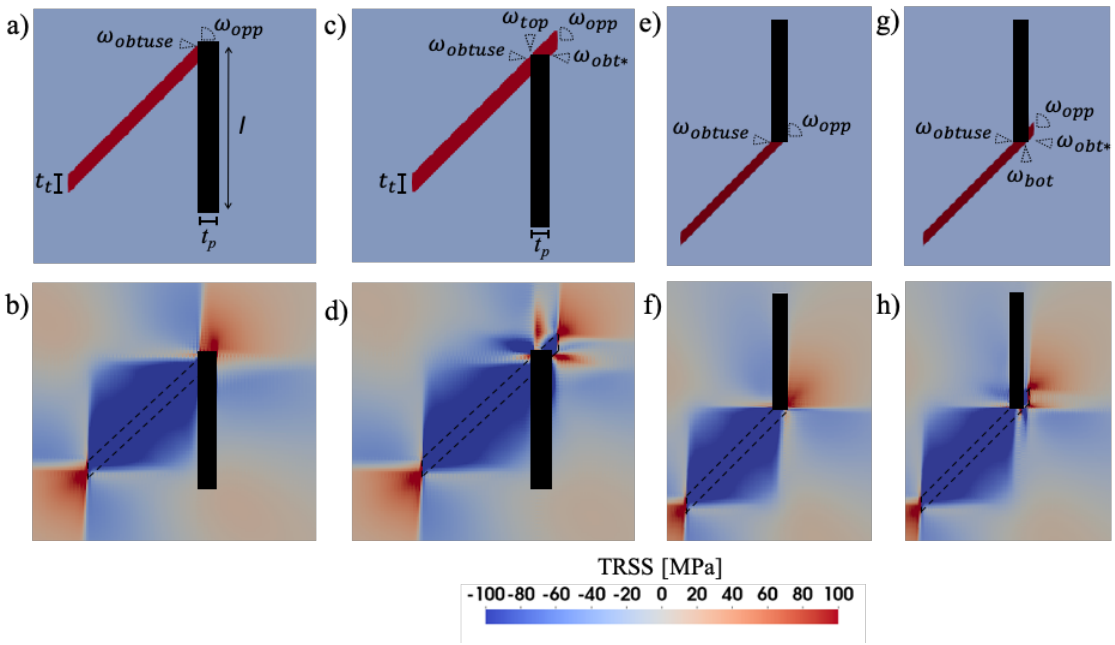

Figure 3.6: a) The twin impinging the upper edge of the precipitate. b) TRSS fields that develop from the twin impinging the upper edge of the precipitate. c) The twin propagating past the upper edge of the precipitate. d) TRSS fields that develop from the twin extending past the upper edge of the precipitate. e) The twin impinging the lower edge of the precipitate. f) TRSS fields that develop from the twin impinging the lower edge of the precipitate. g) The twin propagating past the lower edge of the precipitate. h) TRSS fields that develop from the twin extending past the lower edge of the precipitate.

which is significantly different than that for central impingement shown in Figure 3.1c. First, enhanced stresses on the obtuse angle of the twin-precipitate intersection ω_{obtuse} are still observed, albeit with a much weaker intensity. Second, the TRSS field ahead of the twin tip ω_{opp} appears much stronger, similar to the case in which the twin has not yet impinged on a precipitate (Figure 3.1b). Evidently, the precipitate is less effective at shielding when the twin impinges at its end, suggesting that the twin is still able to bypass the precipitate and continue propagating, consistent with TEM observations reported in the literature [99, 101].

Given the strong likelihood for continued twin propagation, as seen in Figure 3.6b, TRSS fields are calculated for the case when a small embryonic twin has extended past the

edge of the precipitate. Figure 3.6d presents the TRSS fields, in which three additional stress localizations can be seen, as denoted in Figure 3.6c. The first is the enhancement of the stresses at the previous obtuse angle at ω_{obtuse}, the second lies directly above the top edge of the precipitate, ω_{top}, and the third is the localization that develops where the outgoing twin and precipitate come together at an obtuse angle, ω_{obt*}. The two stress concentrations ω_{top} and ω_{obt*} at the new twin domain provide driving forces for both thickening and propagating. So unlike the parent twin, this new twin can thicken as it propagates, leading to the appearance of relatively large twin domains in the microstructure that "engulf" the precipitate [97, 167, 177]. Projection of these strong stress concentrations onto the other variants finds that the cozone and primary variant TRSS fields are nearly identical. Therefore, any of these three localized regions could just as likely form a co-zone variant.

In addition to twin impingement at the upper edge, twins may also impinge on the lower edge of the precipitate, as shown in Figure 3.6e. Again, the strong driving stresses ahead of the twin tip and not significantly reduced by the precipitate and it can be expected that the twin may continue propagating unhindered, as shown in Figure 3.6g. The respective TRSS fields that arise from bottom edge impingement and the extension of the twin past the precipitate are shown in Figure 3.6f and Figure 3.6h, respectively. Similarly to upper edge impingement, three additional stress concentrations can be observed in ω_{obtuse}, ω_{bot}, and ω_{obt*}. Here, however, the stress concentrations are less severe due to the relatively smaller outgoing twin domain. It is expected that as the twin continues propagating forward, these three stress localizations would continue to strengthen acting as twin nucleation sites, similarly to the upper edge impingement case.

The development of additional stress localizations at ω_{top}, ω_{bot} or ω_{obt*} act as sites where subsequent twins can propagate to form a network structure. This scenario is consistent with some signatures highlighted in circles in the in-plane inverse pole figure

(IPF) maps of the deformed AZ91 microstructure in Figure 3.7a [5]. To better distinguish between two variants, Figure 3.7b shows the same IPF map as Figure 7a but with a finer orientation spread. The twin variant corresponding to V2* $(01\bar{1}2)[0\bar{1}11]$ is magenta, while the one associated with V2a $(0\bar{1}12)[01\bar{1}1]$ is blue, as seen in Table 1. When closely observing the white circles in this orientation map, we see the situation where cozone lamellae have formed at the ends of precipitates, where the primary twin lamella has impinged on it. In Figure 3.7a, the yellow circle captures the continuation of a twin propagation past the edge of the precipitate, going from bottom-right to the top-left. Based on the calculations, we suspect that this twin may have nucleated in ω_{obt*}, where the outgoing twin and precipitate come together at an obtuse angle. Last, the green circle in Figure 3.7a suggests that two parallel twins could have formed near the edge of the precipitate.

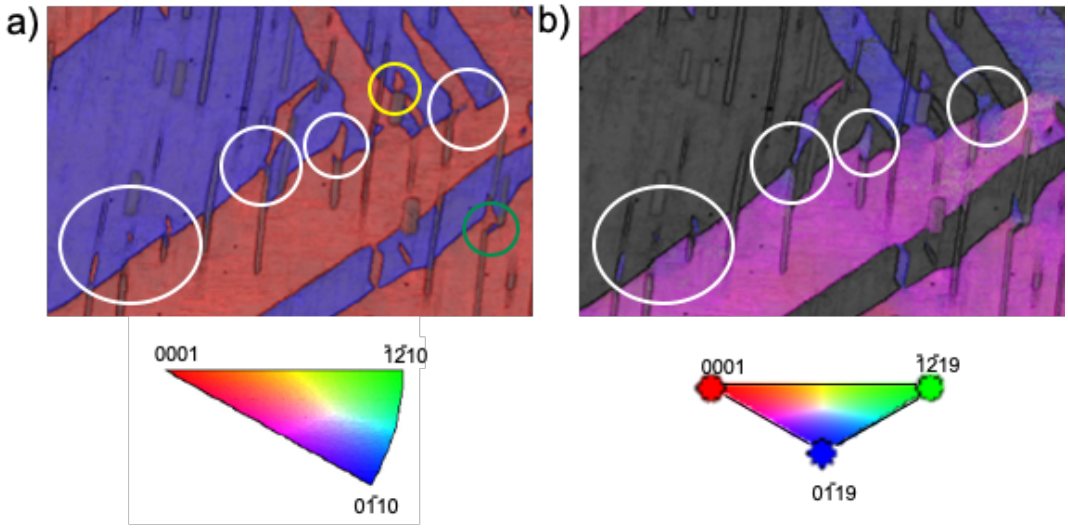

Figure 3.7: a) In-plane inverse pole figure (IPF) map of the compressed Mg-Al alloy. The circles highlight the various twin-tip/precipitate-edge interactions that could lead to the development of a complex network structure of twins. b) IPF map of the same region using a different color key to distinguish the twin variants. The micrograph was adopted and modified from Figure 1 of Xie et al. [5] with permission from Elsevier.

3.9 Remarks on twin propagation pathways

In the present work, the stresses that arise from a single newly formed twin impinging on an elastically deforming precipitate is considered. The evolution of the twin by either migration of the twin boundary or the nucleation of another twin on the other side of the precipitate is an interesting topic and worthy of investigation in a separate work. Currently, there are many unknowns related to the interactions between a single newly propagated twin and a precipitate. No attempt is made here to quantify the nucleation stress of the twin and the barrier required to nucleate a new twin after the initial twin impingement. Such predictions of twin nucleation barriers and detailed kinetic mechanisms of twin nucleation are possible with an atomistic model that takes into consideration defect concentrations and boundary structure [178, 60, 57, 165]. Instead, the mesoscale model used here focuses on the events that occur after a twin has formed and predicts the driving stresses produced around an isolated twin/precipitate interaction. The results provide insight into how the twinned microstructure can develop, irrespective of external considerations, such as local defect structure and external forces. Furthermore, the analysis provided can be generalized to other elastically deforming precipitates with similar dimensions to the plate-shaped basal precipitates studied here.

Based on this study, Figure 3.8 proposes various twinning pathways that can arise and explain the varied complex twin network structures seen in precipitate-hardened Mg alloys. If the twin impinges near the center of the precipitate, the incident twin is effectively pinned, and four pathways develop as depicted in Figure 3.8a. First, the terminated twin may thicken upon further macroscopic loading. Second, a new twin of the same variant can nucleate on the opposite side of the precipitate. Third, a cozone variant can nucleate on the opposite side of the precipitate. Last, a new twin of the cozone variant is likely to form where the twin and precipitate intersect at an obtuse angle. Alternatively,

when the twin impinges near the edge of the precipitate, then the precipitate may not effectively block the initial twin, allowing the twin to continue propagating forward, as illustrated in Figure 3.8b and 3.8c. In this case, our results suggest four possible pathways for both upper edge impingement and lower edge impingement. First, the outgoing twin may be thicker and more blunted than the initial twin due to the additional closely spaced stress localizations that surround the incoming twin tip. Second, an additional twin of the same variant may nucleate closely spaced to the outgoing twin on the opposite side of the precipitate. These two outgoing twins may eventually coalesce, leading to the appearance of a thicker twin. Third, a twin of the cozone variant may nucleate where the initial twin and the precipitate intersect at an obtuse angle. Last, a twin of another variant may nucleate, again where the outgoing twin and precipitate intersect at an obtuse angle. These twinning pathways are not limited to a single twin-precipitate interaction, but rather, can be extended to all propagating twins that impinge on a precipitate and twins that nucleate as a result. As shown in Figure 3.3, relatively high levels of TRSS in ω_{opp}, ranging from 70–110 MPa, can arise solely from the formation of the twin itself, excluding external loads. Consequently, the addition of favorable external loads (i.e., an externally imposed loading direction with respect to the grain orientation that would give positive resolved shear stress for twinning) could further support these conclusions. It is through a cascade of self-catalytic twin propagation and twin tip-precipitate interaction events that can lead to the development of twin network structures.

In general, the findings support that basal precipitates that are thicker, in the $\langle c \rangle$-direction of the parent matrix, are more effective at reducing twinning. This is due to the greater shielding effect provided by the precipitate that blocks the driving stress to nucleate another twin in ω_{opp}. Furthermore, the driving stress in ω_{opp} has been quantified for various precipitate thicknesses to illustrate the extent of the shielding. The ability to reduce the number of twins by increasing precipitate thickness could potentially be

achieved through careful alloying and heat treatment. Furthermore, longer basal precipitates, in the basal plane, can also greatly reduce twinning. This is because, for a given twin volume fraction, smaller precipitates provide more edge interaction sites, increasing the likelihood for twin-tip/precipitate-edge interactions, which can result in multiple high TRSS "hotspots" where new twins can nucleate.

3.10 Summary

In this study, a full-field EVP-FFT model was used to study the effects of twin-tip/precipitate interactions and the influence of these effects on the development of the final twinned microstructure. Although often overlooked, twin-tip propagation is an important stage to consider because the microstructure undergoes significant and rapid changes that will ultimately impact the final twin structures. The analysis is focused on the $\{10\bar{1}2\}$ tensile twin interactions with plate-shaped basal precipitates in AZ91 Mg alloy. It is understood that twin-tip propagation occurs rapidly until the twin-tip is arrested by an obstacle (e.g., precipitates) or by a grain boundary. However, it is unclear what happens next and why. By simulating the isolated impingement of a single twin on a precipitate, key microstructural parameters that influence twin development are identified for the first time.

The precipitate size and the twin tip-precipitate interaction site are important in determining how effective the precipitate is at blocking twin propagation, which twin variants can nucleate, and where new twins can nucleate. In most cases, it is expected that the new twins would tend to nucleate in ω_{opp}, opposite from the twin impingement site, where the TRSS concentration is highest. However, for thicker precipitates, the shielding effect is greater, reducing the propensity for a new twin to nucleate in ω_{opp} while simultaneously increasing the propensity for twins to nucleate in ω_{obtuse}, where the

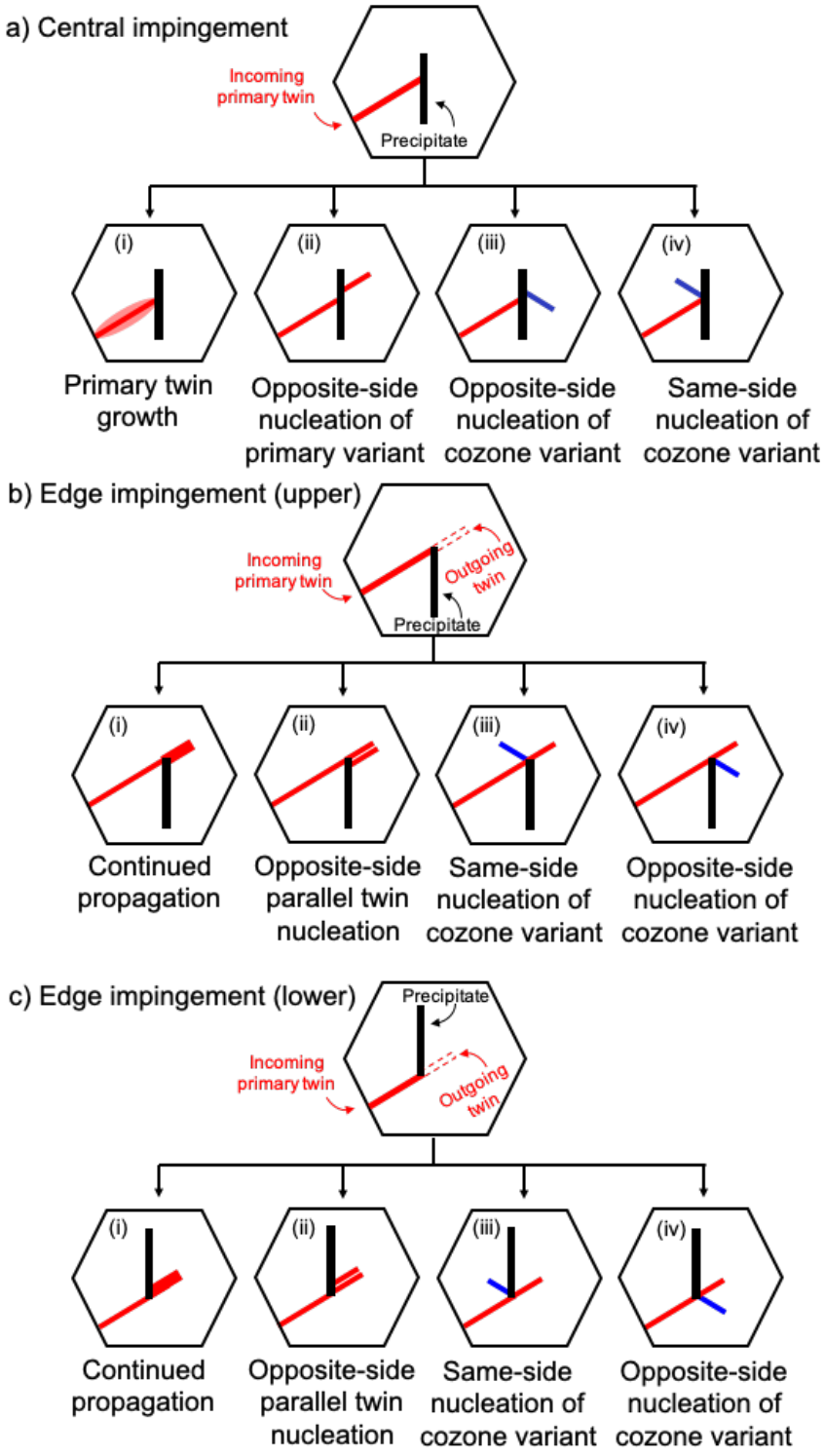
a) Central impingement
Incoming primary twin
Precipitate
(i)
(ii)
(iii)
(iv)
Primary twin growth
Opposite-side nucleation of primary variant
Opposite-side nucleation of cozone variant
Same-side nucleation of cozone variant
b) Edge impingement (upper)
Incoming primary twin
Outgoing twin
Precipitate
(i)
(ii)
(iii)
(iv)
Continued propagation
Opposite-side parallel twin nucleation
Same-side nucleation of cozone variant
Opposite-side nucleation of cozone variant
c) Edge impingement (lower)
Precipitate
Incoming primary twin
Outgoing twin
(i)
(ii)
(iii)
(iv)
Continued propagation
Opposite-side parallel twin nucleation
Same-side nucleation of cozone variant
Opposite-side nucleation of cozone variant

Figure 3.8: Schematic of the twinning pathways that occur after the twin (red) impinges on the precipitate (black). a) If the twin impinges near the center of a precipitate it is blocked, then to accommodate more strain: (i) the impinging twin can thicken, (ii) a new twin of the same variant (red) can nucleate on the opposite side, likely offset from the twin/precipitate junction, (iii) a cozone variant twin (blue) can nucleate on the opposite side of the precipitate, or (iv) a cozone variant twin can nucleate at the twin/precipitate junction on the side where the twin and precipitate meet at an obtuse angle.b) If the twin impinges near the upper edge of the precipitate, the twin may continue to propagate forward. As a result: (i) a thicker outgoing twin that is more blunted than the original one. (ii) two parallel twins of the same variant as the primary twin can nucleate, (iii) a cozone variant can nucleate above the top edge of the precipitate, or (iv) a cozone variant twin can nucleate where the outgoing twin and precipitate meet at an obtuse angle. c) If the twin impinges near the lower edge of the precipitate, the twin may continue to propagate forward. As a result: (i) a thicker outgoing twin that is more blunted than the original one. (ii) two parallel twins of the same variant as the primary twin can nucleate, (iii) a cozone variant can nucleate above the bottom edge of the precipitate, or (iv) a cozone variant twin can nucleate where the outgoing twin and precipitate meet at an obtuse angle.

twin and precipitate come together at an obtuse angle. For relatively thick precipitates, $\frac{t_p}{t_t} > 2$, the driving stresses that aid twin nucleation in ω_{opp} and ω_{obtuse} become comparable and thus, nucleation at either site is equally likely.

The site where the twin impinges on the precipitate can also greatly influence subsequent twin development. When a twin impinges near the center of precipitates, the incoming twin is effectively blocked by the precipitates and instead of continued propagation, new twins can nucleate in ω_{obtuse} and ω_{opp} in order to accommodate strain instead. It is also possible for the twin to impinge near the edge of the precipitate. In this case, the propagation of the incoming twin is not significantly blocked, and the incoming twin can continue. The TRSS fields that develop in the matrix after the initial twin propagates past the edge of the precipitate are unique and offer additional twin nucleation sites (ω_{obtuse}, ω_{top}, and ω_{obt*}) where the stresses are enhanced and localized. In both cases, the interaction between the twin and precipitates results in the possible multiplication of twin bodies throughout the microstructure. Additionally, twin thickening is also possible,

albeit, considerably more difficult due to the high backstresses in the twin and near the twin boundaries that resist thickening.

At relatively low strains during the early stages of deformation, thin twins begin to proliferate the microstructure and the interactions between propagating twins and precipitates influences the number of twins that form and their distribution. Controlling the twinning behavior is vital in understanding the deformation behavior of Mg alloys, since twinning often causes the material to fail prematurely. The revealed interactions between propagating twins and precipitates in AZ91 can help to guide alloy design and optimize heat treatment processing for the engineering of Mg alloys with superior mechanical properties through the control of size, geometry and habit plane of precipitates found in the matrix.

Chapter 4

Twin growth mechanism enabled by precipitates in AZ91

4.1 Introduction

Interest in hexagonal close-packed (HCP) magnesium (Mg) alloys in structural applications has risen over the last few decades due to their low density, high specific strength, abundance, and recyclability [12, 11]. A common strategy to bolster the mechanical properties of Mg alloys, such as AZ91, is to form a dispersion of precipitates throughout the microstructure that blocks the glide of dislocations [179, 4, 160, 162, 36]. For instance, the precipitates that form in AZ91 alloy are either thin lath-shaped basal or rod-shaped prismatic $Mg_{17}Al_{12}$ precipitates with a body-centered cubic (BCC) crystal structure [84, 88]. The habit plane of basal- and prismatic-precipitates is parallel to the basal and prismatic planes of the parent hcp phase, respectively. Plastic deformation of the AZ91 alloy under relatively low strains and at room temperature is accommodated by both dislocation slip and deformation twinning [88, 35]. The amount of twinning that develops can control the ductility, mechanical stability, strain-hardening response, and

texture evolution [180, 181, 104, 182, 183, 86]. In comparison to precipitate-dislocation interactions, the interactions between the precipitates and twins are much less understood but clearly of equal importance in understanding the deformation behavior of the AZ91 alloy.

The development of twins generally consists of three sequential stages: nucleation, propagation, and growth. Precipitates have been shown to have a distinct influence on each stage [99]. It has been suggested that precipitate/matrix interfaces can serve as nucleation sites since their defect and stress concentrations are higher compared to the matrix [60]. Consistent with this notion, some studies have reported a greater number of twin lamellae but similar twin volume fractions in materials with precipitates and without them [100, 184, 90]. In twin tip propagation, precipitates can act as obstacles, causing the tip to fully arrest or to skew from the twin habit plane as it bypasses the precipitate [99, 39]. The location of the twin impingement on the precipitate and the thickness of the twin with respect to the precipitate size have been shown to determine the path taken by the twin after interacting with the precipitate [8]. In twin boundary migration, it is commonly reported that the precipitates retard twin growth by acting as hard obstacles that pin the migration of twin boundaries [100, 177, 91, 95, 185, 96, 101]. However, it is also frequently observed that plastically deformed AZ91 microstructures contain many wide twin domains that sometimes entirely engulf precipitates [99, 171]. How relatively large twins can grow in a field of precipitates and the role played by precipitates in twin growth have yet to be clarified. Understanding the mechanisms of precipitate bypass and growth of deformation twins is of importance in controlling the microstructural evolution and mechanical behavior of AZ91.

Recently, many studies have reported that precipitates can increase the barrier for twin growth, thereby hardening twinning [95, 97, 83, 94, 82]. The basic question regarding the mechanisms by which a twin domain can still grow and engulf the precipitates has

not been addressed. Most studies have considered the migration of the coherent twin boundary and their interactions as they become pinned by precipitates. The twins in these studies are assumed to be fully propagated at instantiation, thus they do not capture the effects of twin propagation. Also, the role of dislocations on the twin growth process in connection with precipitates has not been adequately studied. Only recently, via crystal plasticity calculations, Siska et al. [39] reported that precipitates could change the critical resolved shear stress (CRSS) for slip, thereby affecting twin growth. However, this study was conducted using a phenomenological hardening law for the CRSS for slip that is unrelated to dislocation content and ignores slip interactions.

In precipitate-free materials the mechanism for twin boundary migration is controlled by the interaction of the twin boundary with dislocations from the parent matrix [71, 186, 187, 188, 189]. For example, the dissociation of basal dislocation at the $\{10\bar{1}2\}$ tensile twin boundaries in Mg develops facets that facilitate the migration of the twin boundary in the twin plane normal direction through a combination of twinning dislocation glide and climb along the facets [190]. As indicated by these studies, the presence of suitable defects in combination with favorable driving stresses are needed to advance the twin boundary.

In this work, the interactions between $Mg_{17}Al_{12}$ plate-shaped basal precipitates and $\{10\bar{1}2\}$ tensile twins at different stages of twin development in AZ91 are studied. An elasto-viscoplastic fast Fourier transform (EVP-FFT) model with a dislocation-density (DD) based hardening law is employed to calculate the spatial distribution of internal micromechanical fields and dislocation densities corresponding to each interaction. The results indicate that twins interacting with precipitates will grow asymmetrically, with one twin boundary remaining relatively parallel to its crystallographic twinning plane and the other forming a serrated structure that deviates from its crystallographic plane. These findings help to explain the twin morphologies near precipitates observed in transmission

electron microscopy (TEM) observations of deformed AZ91 [171, 5]. A mechanism is proposed that enables the growth/thickening of an early-stage thin twin that is arrested by a precipitate by the formation and propagation of a second twin on the other side of the precipitate.

4.2 Characterization of AZ91 slip strength hardening model parameters

To perform the explicit twin-precipitate interaction simulations, the DD-based hardening model parameters of the dominant slip modes are required. An EVP-FFT model, presented in Chapter 2.4, was employed to calibrate the material parameters associated with the DD hardening law for AZ91 alloy by fitting with experimental data. Experimentally measured uniaxial tensile stress-strain curves at 293 K and 463 K for a strain rate of 1×10^{-4} 1/s from Dini et al. [6] is considered for model calibration.

Figure 4.1a shows the FFT unit cell that represents AZ91 alloy polycrystalline microstructure. The model unit cell is comprised of 128 equiaxed grains with a uniform distribution of crystallographic orientations and approximately 7.5% volume fraction of $Mg_{17}Al_{12}$ precipitates, colored in black [6]. The unit cell is discretized into 64x64x64 voxels; accordingly, every grain is represented by approximately 2048 voxels. The Mg17Al12 precipitates are of BCC crystal structure and share a Potter orientation relationship with the parent grain crystallographic orientation that it resides in, described by $(0001)_{HCP}$ 2° from $(011)_{BCC}$, $[2\bar{1}\bar{1}0]_{HCP}$ // $[1\bar{1}1]_{BCC}$, and $(01\bar{1}1)_{HCP}$ // $(110)_{BCC}$ [84, 88, 99]. The $Mg_{17}Al_{12}$ precipitates are treated as elastically deforming domains, while the AZ91 matrix was allowed to deform by a combination of anisotropic elasticity and visco-plasticity.

The elastic constants C_{11}, C_{12}, and C_{44} of the $Mg_{17}Al_{12}$ precipitates at different

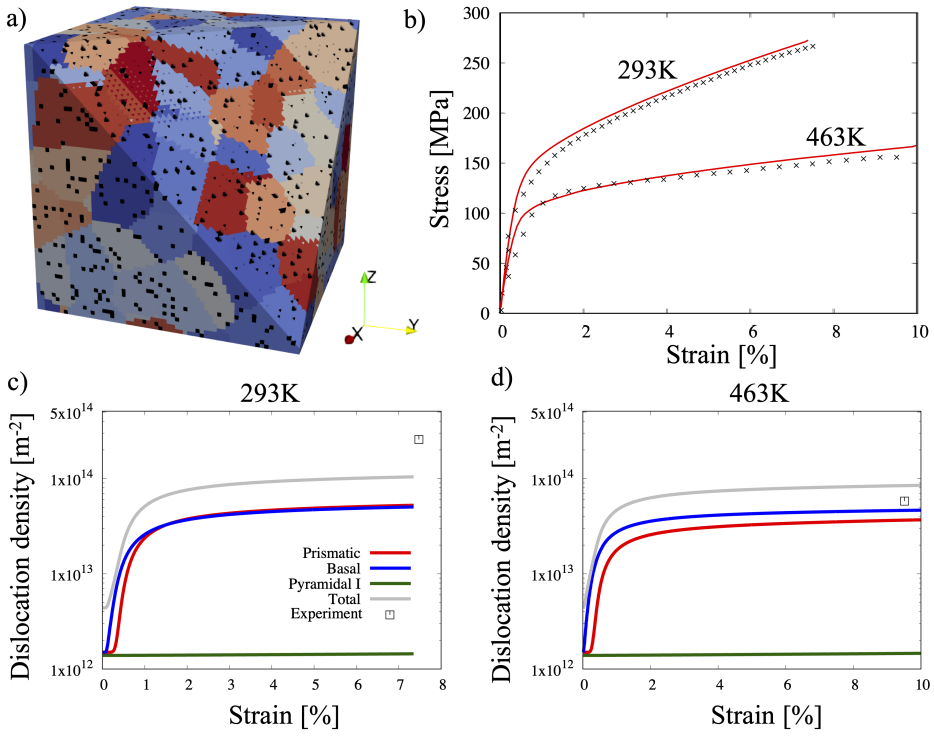

Figure 4.1: a) Visualization of the polycrystalline AZ91 simulation cell used to obtain the DD constitutive law parameters. The unit cell consists of 128 equiaxed grains with a 7.5% volume fraction of Mg17Al12 precipitates, shown in black. b) Comparison of the predicted uniaxial tensile stress-strain response (in red) to experimentally obtained curves (in black) from Dini et al. [6] at 293 and 463 K. In the model calculations, a strain rate of 1×10^{-4} 1/s is imposed in the x-direction. Comparison at c) 293K and d) 463K of the predicted total (gray), prismatic (red), basal (blue), and pyramidal-I (green) dislocation densities by the EVP-FFT model with those measured (square marker) by Dini et al. [7].

temperatures are not available, and thus, values calculated from Density Functional Theory (DFT) were used corresponding to 86.8, 29.0, and 20.0 GPa, respectively, for both temperatures [169]. The anisotropic elastic coefficients C_{11}, C_{12}, C_{13}, C_{33}, C_{44} of AZ91 were approximated by the coefficients of pure Mg at 293 K and 463 K with values of 59.0, 25.5, 21.5, 61.0, 16.7 and 57.0, 25.4, 21.1, 58.0, 15.0 GPa, respectively [191]. The shear modulus, μ, used in Equations 2.9 and 2.12, for AZ91 at 293 K and 463 K were set to equal to C_{44}, which is 16.7 and 15.0 GPa, respectively [192]. For plastic slip in the AZ91

	$\alpha = 1$	$\alpha = 2$	$\alpha = 3$
	prismatic $\langle a \rangle$	basal $\langle a \rangle$	pyramidal-I $\langle c + a \rangle$
τ_0^α [MPa]	100	35	160
b^α	3.231e-10	3.231e-10	6.0771e-10
$\dot{\varepsilon}_0$ [s^{-1}]	1.0e+07	1.0e+07	1.0e+07
ρ_0 [m^{-2}]	1.50e+12	1.50e+12	1.50e+12
ρ_{debris} [m^{-2}]	1.0e-01	1.0e-01	1.0e-01
A^α_{293K}	20	0	0
A^α_{463K}	0	10	0
k_1^α [m^{-1}]	9.0e+09	3.5e+09	1.0e+07
g^α	5.0e-03	5.0e-03	1.0e-03
D^α [MPa]	5.0e+03	5.0e+03	9.0e+03

Table 4.1: Dislocation density-based constitutive model parameters that are found by fitting to the experimentally obtained stress-strain response of AZ91 alloy under uniaxial tension at 293K and 463 K.

matrix, three slip modes were made available: prismatic $\langle a \rangle$, basal $\langle a \rangle$ and pyramidal-I $\langle c+a \rangle$ slip. Twinning deformation was not accounted for in the parameterization since its contribution was observed to be negligible by Dini et al.[7]. The simulation begins with the initial values of the CRSS for prismatic, basal, and pyramidal-I slip modes for AZ91 from Bhattacharyya et al.[35] with self and latent hardening set to be 0.15 [193]. Figure 4.1b compares the calculated stress-strain response (red solid lines) to the experimentally measured curves (symbols). The corresponding constitutive law parameters for all three slip modes are listed in Table 4.1. The evolution of the total (gray), prismatic (red), basal (blue) and pyramidal-I (green) dislocation densities with respect to applied strain at 293K and 463K are presented in Figure 4.1c and 4.1d, respectively, along with the measured densities (designated by a square marker) by Dini et al. [7]. Although the EVP-FFT model was calibrated using only the stress-strain response, the predicted densities also fall

within reasonable agreement of experimentally measured values at both temperatures.

4.3 Model set-up

In this work, twins are simulated explicitly through the reorientation of a predefined twin domain and the incremental development of the characteristic twinning shear homogeneously within the twin domain [66]. Accordingly, the $\{10\bar{1}2\}$ tensile twin domain voxels are reoriented 86.3° about $\langle\bar{1}2\bar{1}0\rangle$ and uniformly sheared by the characteristic twinning shear of 12.9%. The precipitate domains are also predefined domains with crystallographic and material properties of the commonly observed $Mg_{17}Al_{12}$ plate-shaped precipitates that lie on the basal plane of the parent matrix. Figure 4.2 depicts the simulation setup with two precipitates of the same size: precipitate-1 and precipitate-2 in orange and red, respectively. The twins and precipitates are embedded in an AZ91 matrix (light blue). The crystallographic orientation in the Bunge convention of the parent grain is chosen to be $(0°, 88.16°, 0°)$, and it is illustrated by the hexagonal inset in Figure 4.2. Following the frequently observed Potter orientation relationship [84, 88, 99], the crystallographic orientation of the precipitates is assigned to be $(39.23°, 114°, 63.43°)$. Other orientation relationships and variations in orientation may exist between the matrix and precipitates and can be easily accounted for in the model. In the present work, the most commonly observed orientation relationship was considered for simplicity.

The simulation cell size is discretized into 3 x 550 x 550 voxels. The twin thickness, t, and precipitate width in the Y-direction are both four voxels, appropriate for representing thin, newly propagating twins. In experiments, the aspect ratio of precipitates can be seen to vary between 1-100 [5]. Thus, the precipitate length in the Z-direction is taken as 40 voxels that corresponds to the aspect ratio of eight. Further, the precipitate length was chosen in order to keep the twin impingement site far away from the edges, since

these events make up a majority of twin-precipitate interactions. Near edge impingement can also occur, however, is far less likely and can lead to the development of complex stress states [8]. Seven different precipitate spacings, d, were considered, ranging from 4 to 200 voxels, representative of what is commonly observed in deformed AZ91 [5].

The parent matrix is surrounded by a buffer layer (dark blue) of 50 voxels thick in the Y and Z directions, with uniformly distributed crystallographic orientations. This buffer layer approximates the response of a polycrystalline medium and shields the parent matrix from overlapping fields due to the periodic boundary conditions. There is no buffer layer in the X-direction. The simulation uses periodic boundary conditions, which causes the microstructure to adopt a columnar microstructure. This microstructural simplification is appropriate to use when studying the interactions of twins with thicknesses that are much smaller than the dimensions of the precipitates in the X and Z-direction, such as twins during the early stages of propagation being studied here. Furthermore, the crystallography of the twin, with its twin plane normal and twin shear direction in-plane, allows us to consider the fields in a 2D slice, as shown in Figure 4.2, since there are no gradients in the out-of-plane direction.

We adopt a simplification of the intricate microstructures found within twin and precipitate-hardened AZ91 alloy. The real microstructure may contain many twins and precipitate with geometries that are more complex than those represented here. However, the idealized model scenario permits the isolation of the interactions between two sequentially formed twins without the additional complications from other precipitates and twins. The model setup describes situations that may occur just as a twin has finished propagating in the twinning shear direction and has been arrested at a precipitate. Previously, such calculations have shown that depending on the precipitate-1 thickness with respect to the twin-1 thickness, a second twin, twin-2, may form on the other side of precipitate-1 and may eventually become arrested by another precipitate, precipitate-2

[8]. When faced with an array of precipitates, twins may continue to successively impinge on one side of each precipitate and reform on the other side in order to continue propagating. However, it is often observed that twins can also thicken and eventually engulf precipitates as they propagate through an array of precipitates. The influence of precipitates and precipitate spacing on twin thickening after impingements have yet to be investigated. The calculations that follow aim to identify the likely growth mechanisms of twin-1 and twin-2 and the role of the inter-precipitate spacing that stands in their way.

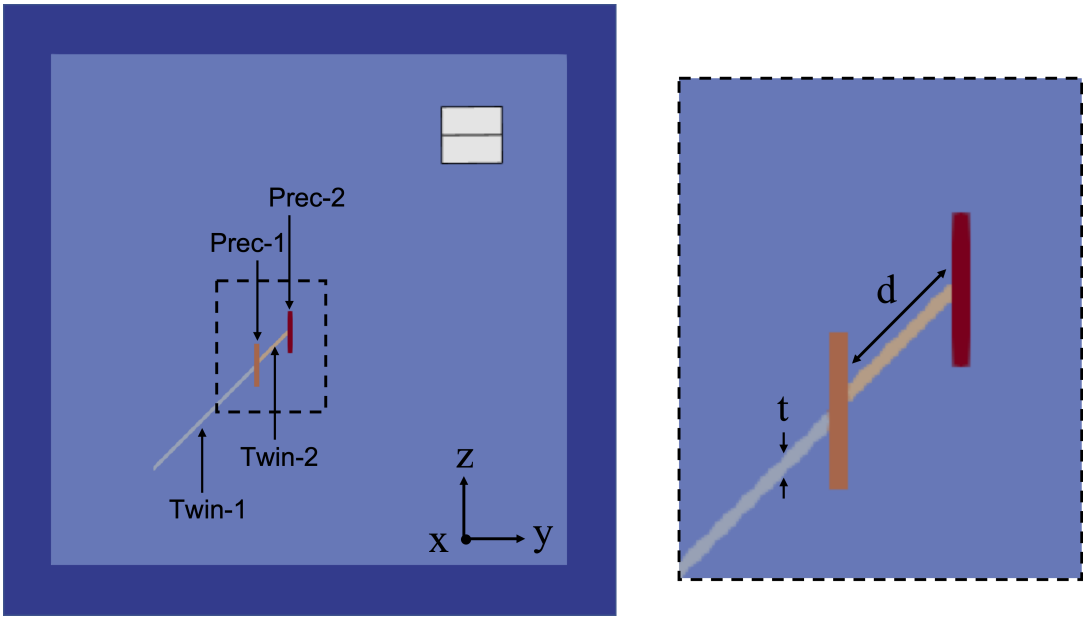

Figure 4.2: Simulation setup consisting of a single crystal AZ91 (light blue) surrounded by a polycrystalline buffer layer (dark blue). Within the parent grain, twin-1 impinges upon precipitate-1, causing twin-2 to form between precipitate-1 and precipitate-2. The crystallographic orientation of the parent grain is represented by the hexagonal inset in the top right. A zoomed-in region around the precipitates is outlined by black dashed lines for closer inspection.

4.4 Effects of precipitates on localized plasticity in twin-free crystals

Uniaxial compression strain is applied in fine strain increments to a twin-free, precipitate containing crystal in the a-axis-direction of the parent grain. To determine the path taken by a twin approaching the precipitates, the twin plane resolved shear stress (TRSS), a relevant driving stress component for twin formation or twin boundary propagation, is examined. At 4% applied strain, a TRSS of approximately 30 MPa is produced in the parent matrix, appropriate for the formation of tensile twins [194, 42, 43]. The stresses are inhomogeneous and result from the mismatch in elastic and plastic properties between the elastically hard precipitates and elasto-visco-plastically deforming AZ91 matrix [66, 176]. Plastic deformation is seen to concentrate in the matrix around the hard bcc precipitates, regardless of precipitate spacing. Figure 4.3 shows the distribution of the average CRSS values after initial 4% compression for each slip mode in the parent matrix in a small region around the precipitates outlined by dashed lines in Figure 4.2. For all three slip modes, the CRSS increases or hardens the most along the short sides of the precipitates and the least along the long sides of the precipitates. Basal slip experiences the most significant hardening. The lowest CRSS values were 2.9 times greater than its initial CRSS (44.8 MPa). Larger resistances to plastic deformation around the precipitates can result in higher stresses and stress concentrations in the parent grain with the addition of approaching deformation twins.

Figure 4.4 shows the TRSS field the twin-free, precipitate containing crystal at 4% compression strain. Along the short sides of the precipitates, the TRSS is approximately -81 MPa and resists twinning. The long sides of the precipitate/matrix interface experience enhanced positive TRSS, which would aid twin development, with the peak at the center reaching up to 32 MPa, more than three times higher than the surrounding

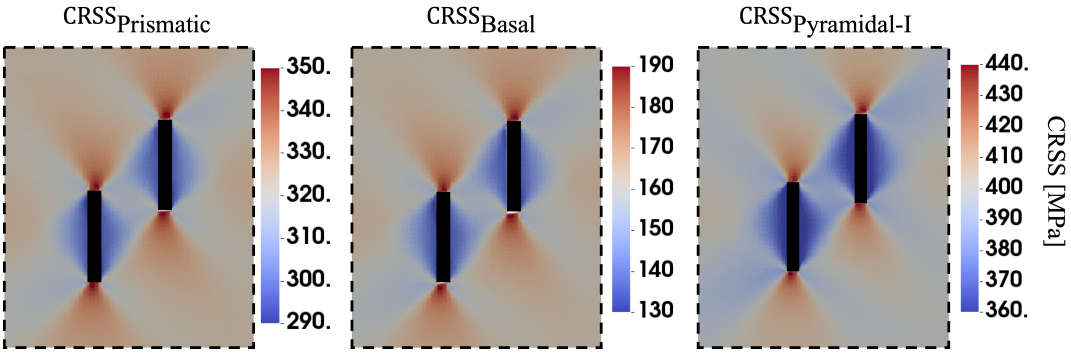

Figure 4.3: Average CRSS values of prismatic, basal, and pyramidal-I slip modes around the precipitate after an initial 4% strain in the X-direction (out-of-plane) parallel to the a-axis of the parent matrix, demonstrating significant local hardening around the precipitates.

matrix ($\sim$ 9 MPa). If an incoming twin impinges the short ends of the precipitates, its stress field would interact with an anti-twinning contribution from the precipitate, possibly resisting the propagation of the twin. In contrast, it would encounter less resistance should it impinge the center of the long side of the precipitate. The positive TRSS on the long sides of the precipitates can also favor the nucleation of twins from the precipitate interfaces, which supports the experimentally observed increase in the twinning density with the precipitates [90, 95]. This situation, however, is not considered further here. Rather, the interaction of the twin tip with the precipitates is studied to understand its effect on propagation and growth of already formed twin domains.

4.5 Stress fields around preciptiates and twins

To determine the role of precipitates on twinning, deformation twins are introduced to the crystal containing precipitates under a fixed macroscopic loading. As illustrated in Figure 4.4b, while under 4% compressive strain, twin-1 propagates up to precipitate at its center. In this case, twin-1 has a much smaller thickness, $t = 4$ voxels, than the precipitate length, $l = 40$ voxels, in the Z-direction. Figure 4.4b presents the calculated

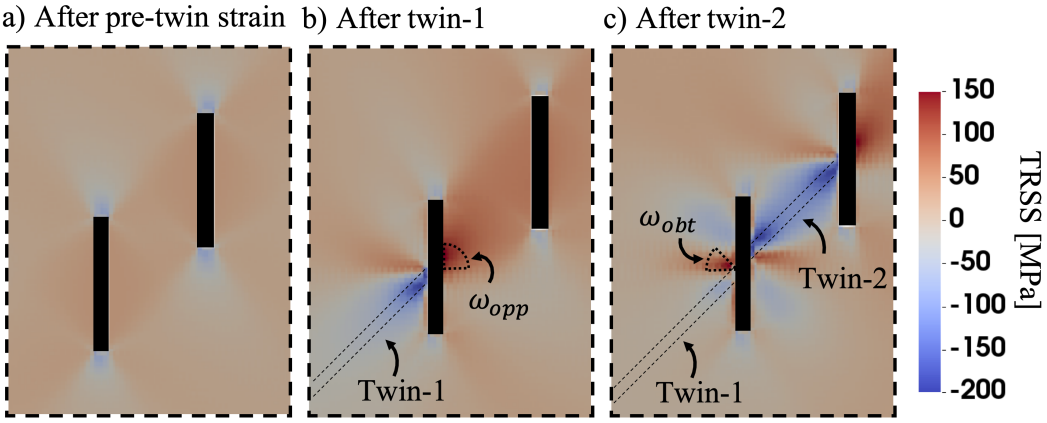

Figure 4.4: TRSS distributions around precipitates: a) After an initial 4% compression in the a-axis of the parent matrix. Positive TRSS develop along the long sides of the precipitate, supporting the development of twins, while negative TRSS arise along the short sides of the precipitates, resisting twinning. b) After the formation of twin-1, a localized stress concentration developed in ω_{opp}, suggesting the likely formation of twin-2 in this region. Strong backstresses arise around twin-1, resulting in negative TRSS around twin-1, indicating that growth is difficult. c) After the formation of twin-2, TRSS is augmented in ω_{obt}, showing that twin-2 can aid in the growth of twin-1 by increasing the driving stresses for twin boundary migration near the precipitate that they co-impinge upon.

TRSS field as a result of the interaction. A TRSS concentration forms on the opposite side of the precipitate, in the region ω_{opp}, reaching up to 155 MPa, about five times greater than that from the initial macroscopic loading alone ($\sim$32 MPa). Consequently, a new twin of the same variant along the precipitate/matrix boundary near ω_{opp} could result from the twin/precipitate intersection [8]. The TRSS in the region in between the two precipitates are shown in Figures 4.5c and 4.5d by two red profiles. These two lines will eventually become the upper and lower twin boundaries of another twin, twin-2, that emerges due to the twin-1 interaction with precipitate-1. Near ω_{opp}, corresponding to the left side of Figures 4.5c, and 4.5d, the TRSS is enhanced greatly from $\sim$ 32 MPa before twin-1 impingement (gray points) to values between $135 - 150$ MPa after twin-1 impingment (red points). The five-fold increase in driving force supports forming of a second twin-2 of the same variant as the first.

Figures 4.5a and 4.5b examine closely the calculated TRSS profiles in the parent matrix along the upper and lower twin boundaries of twin-1, which are relevant for twin boundary migration during the twin growth stage. Along the entire upper and lower boundary of twin-1, the TRSS is negative, indicating resistance against twin boundary migration and the need for more applied deformation for twin growth. Here, we classify the decrease in TRSS stresses resulting from the reaction of hard, elastic precipitate to the twin shear as backstresses [176]. The largest backstresses are experienced near the precipitate, corresponding to the right side of Figures 4.5a and 4.5b. Since the backstresses are much less at the upper twin-1 boundary than lower twin-1 boundary at the twin/precipitate junction site, it is anticipated that twin-1 would expand asymmetrically, initiating from the upper boundary first.

Based on the foregoing observations, calculations are performed for the situation in Figure 4.2, in which twin-2 is formed where the peak TRSS had developed and extended between precipitate-1 and precipitate-2 and made with equal thickness as twin-1. In the simulation, this process occurred under the same macroscopic loading after the formation of twin-1. Reminiscent of twin-1, the leading tip of twin-2 causes a rise in TRSS of up to ~ 155 MPa on the opposite side of precipitate-2, seen in Figure 4.4c. Severe backstresses result in intensely negative TRSS in the vicinity of twin-2 boundaries. Specifically, along twin-2 boundaries, the magnitude of the TRSS is nearly -160 MPa where twin-2 impinges upon both precipitate-1 and precipitate-2 at an acute angle, that is, on the left of the upper boundary and right of the lower boundary, see blue profiles in Figure 4.5c and 4.5d. The lower twin-2 boundary near precipitate-1 develops slightly higher TRSS due to its closer alignment with the peak TRSS concentration generated by twin-1 [8]. It is reduced to -100 MPa near the center of the twin. At the same time, the backstresses along the boundaries of twin-1 are relieved by the formation of twin-2, shown by the blue markers in Figures 4.5a and 4.5b. The TRSS in the upper and lower twin boundaries of

twin-1 near precipitate-1 increase by as much as 100 MPa. The backstresses along the upper boundary of twin-1 are relieved more than the lower boundary of twin-1 and reach up to 150 MPa in ω_{obt}, see Figure 4c, much greater than the $\sim$ 32 MPa that existed after the initial straining.

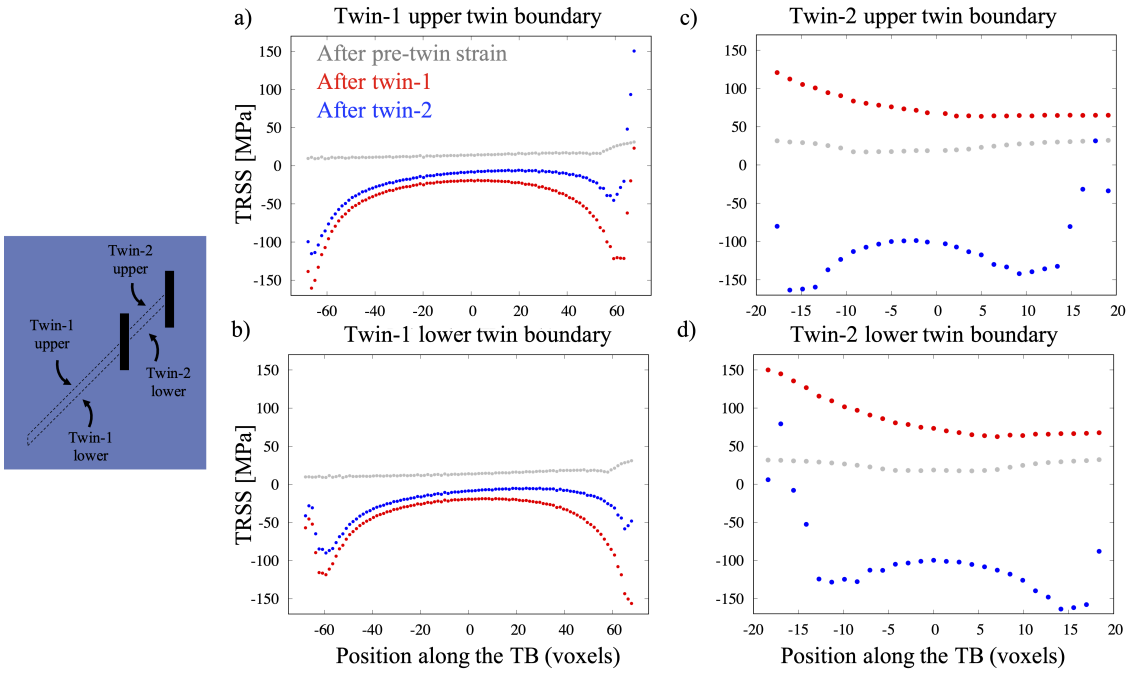

Figure 4.5: Predicted TRSS along the a) upper and b) lower twin boundary of twin-1 and the c) upper and d) lower twin boundary of twin-2. The figure inset schematically illustrates the twin-1 and twin-2 boundaries. Gray markers represent the TRSS along the twin boundaries after an initial 4% compression in the a-direction, i.e., before twinning. Red and blue markers correspond to the TRSS after forming twin-1 and twin-2, respectively, for the same macroscopic loading.

The augmented twin stresses from twin-2 on twin-1 suggest a two-step mechanism for the growth of twins that are interacting with precipitates. First, twin-1 must propagate and impinge upon a precipitate, triggering the nucleation and propagation of twin-2 on the other side of the precipitate. Secondly, twin-2 encourages the growth of twin-1 along the upper boundary near the precipitate that they co-impinge upon. With the formation of twin-2, little to no additional applied stresses would be needed for the growth of twin-1.

The mutual aid between twin-1 and twin-2 allows for the migration of twin-1 boundary around precipitate-1. This result is similar to the observation reported in Kumar et al. [175], where the effect of twin-twin interaction at the grain boundaries on twin growth is studied.

4.6 Effect of precipitate spacing on twinning stresses

Thus far, the precipitate spacing d has been fixed. The effects of d on twin-1 growth is investigated next. Figure 4.6 shows the evolution of the TRSS along the twin-1 boundaries after each step in the interaction process: 1) the initial 4% a-axis compression (gray), 2) the formation of twin-1 (red) only, and 3) the formation of twin-1 and then twin-2 (blue). In all cases, twin-2 extends from the first precipitate to the second and has length d. The average TRSS in the two regions shown in Figure 4.6a are studied: at the twin-tip/precipitate junction (solid lines) and in the center of the twin lamellae (dashed lines). Each region is equal to the twin thickness. In the second step, when the twin first intersects the precipitate, the TRSS fields around twin-1 under external load are insensitive to the spacing d. It appears that the heterogeneous stress fields around precipitate-2 are too far away to influence the TRSS fields at twin-1, even for the closest spacing of $\frac{d}{t} = 1$. Figure 4.6b shows that for all d/t ranging from 1 to 50, the average TRSS along the upper boundary reduced from $\sim +20$ MPa (gray dashed lines) to ~ -20 MPa in the center (red dashed lines) and from $\sim +30$ MPa (gray solid lines) to ~ -50 MPa at the twin tip (red solid lines) after twin-1 impinges on precipitate-1. In Figure 4.6c, for the lower boundary of twin-1, we observe a reduction in TRSS to ~ -20 in its center and to ~ -130 MPa at its tip. Thus, we find that migration of the lower boundary near the twin tip is more limited than that of the upper boundary.

The spacing d has an important influence on the stress field once twin-2 has formed

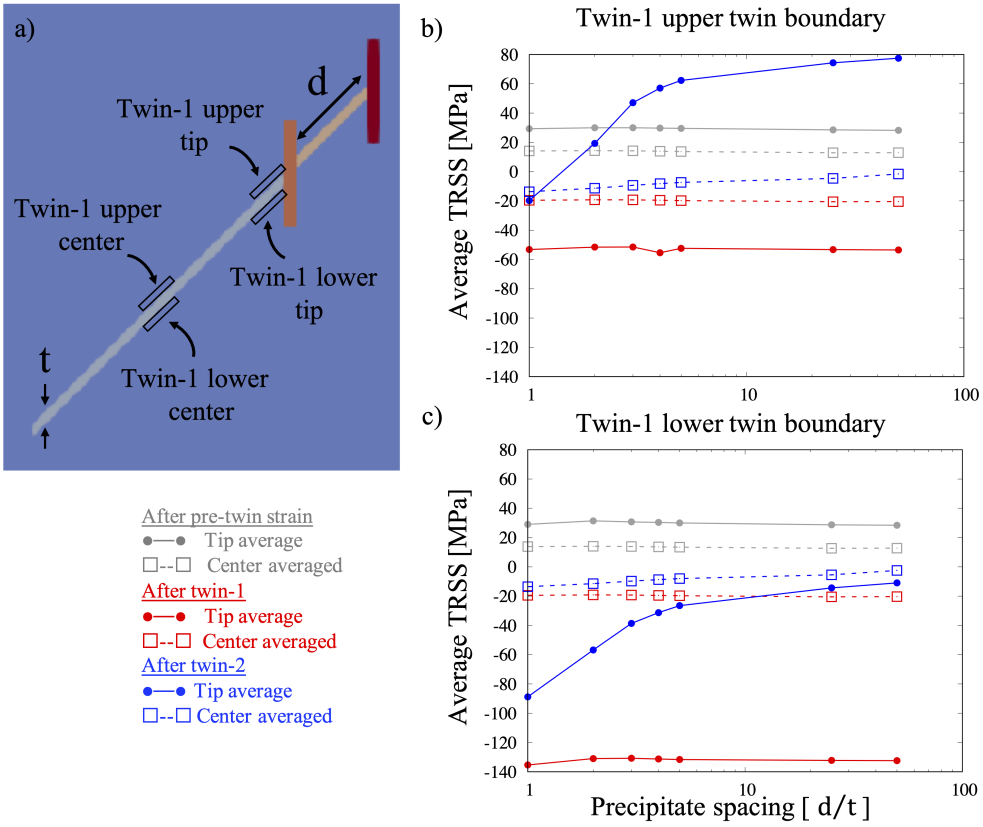

Figure 4.6: a) An enlarged view of the simulated twin-precipitate interaction region. The fields along the upper and lower boundaries of twin-1 near the center of twin-1 and near the precipitate-1 interaction site are outlined by black boxes to be considered for further detailed analysis. The variation in average TRSS taken along the (b) upper and (c) lower twin boundary of twin-1 near the center and the impingement site as a function of precipitate spacings, d, normalized by the twin thickness, t. The average TRSS values after an initial 4% compression (prior to the formation of twin-1), after the formation of twin-1 (prior to the formation of twin-2), and after the formation of twin-2 are shown in gray, red, and blue lines, respectively. Solid and dashed lines represent the averages taken near the impingement site and center of the twin-1, respectively.

and extended to precipitate-2. For tight precipitate spacings, $d = 1t$ to $5t$, the average TRSS along the top boundary of twin-1 increases rapidly from ~ -20 to 62 MPa near the tip (solid blue lines) and modestly from ~ -20 to -7 MPa near the center (dashed blue lines) of twin-1, seen in Figures 4.6b. The larger d, the greater the enhancement by twin-2 on twin-1, with the largest effect near the tip. For $d > 5t$, the enhancement saturates with TRSS values reaching up to $\sim +80$ and -2 MPa at the tip and central regions, respectively. Similar trends are observed along the lower boundary of twin-1, however, the TRSS values remain negative and less favorable for twin boundary migration. As shown in Figure 4.5, for all d/t cases, both upper and lower boundaries of twin-2 remain resistant to twin boundary migration, and consequently are not shown here. Although the subsequently formed twin-2 may not thicken, it can support the migration of the upper boundary of twin-1 when d is large, enabling twin-1 to grow around the precipitate. Without twin-2, the ability of a twin-1 to thicken independently and bypass the precipitate is unlikely due to the large backstresses that develop when the twin becomes constrained at both tips. To sum, with precipitate spacings $d \geq 5t$ a two-step precipitate bypass mechanism is possible. In principle, this boundary migration mechanism for circumventing precipitates can continue with each new precipitate encounter. After twin-2 impinges precipitate-2, another twin, twin-3, can form on the opposite side of precipitate-2, resulting in the relief of the backstresses on twin-2 back and helping it to grow.

4.7 Effect of precipitate spacing on dislocation densities

In addition to the sufficiently high stresses, dislocation activity in the matrix has also been proposed to help aid twin boundary migration [188, 195, 196, 197, 68, 198]. The strain fields calculated in the simulations are associated with slip activity, which provides insight into the slip modes favored to accommodate the twin shear. Figure 4.7 depicts the dislocation density fields that arise during the different stages of the simulation: after the pre-twin strain, after forming twin-1, and after forming twin-2. In Figure 4.7, the precipitates are colored in black. After pre-twin straining, a heterogeneous distribution of dislocations emerges around the precipitates, with dislocation densities much greater than the initial value of 1.5×10^{12} m^{-2} for all slip modes. Prismatic activity in the parent matrix was the greatest, resulting in densities that grew by two orders of magnitude. Greater densities of prismatic dislocations developed near the short edges of the precipitates than compared to the long edges of the precipitates, as seen in Figure 4.7a. The opposite trends are seen for the pyramidal dislocation densities, resulting in more dislocations along the long edges of the precipitates than the short edges, seen in Figure 4.7c. The development of basal dislocations was concentrated at the corners of the precipitates.

After forming twin-1, prismatic dislocation densities remained relatively constant, and additional pyramidal dislocations were generated only in the twin near the impinging twin tip. The basal dislocation field experiences the greatest change, with increased densities all along the precipitate/matrix boundary and large concentrations of dislocation appearing inside the impinging twin tip and in ω_{obt}. After twin-2 forms, again, prismatic dislocation densities do not change. Evidently, twinning does not significantly influence prismatic slip activity. Pyramidal dislocations were primarily generated at the twin tips of twin-2 and twin-1 tip that co-impinges on precipitate-1. The formation of

twin-2 caused basal dislocations densities to increase significantly inside and around each tip of twin-2. Furthermore, additional basal dislocations can be observed in the twin-1 tip that co-impinges the precipitate and, in the region ω_{obt}.

Next, a closer inspection of the regions near the center of the twin-1 and near the twin-1 and precipitate-1 interaction site, as outlined in black boxes in Figure 4.6a, is presented. For the following analysis, only the upper boundary of twin-1 is considered since it has favorable stresses to support its migration, as seen in Figure 4.6. The increase in average dislocation density for each slip mode, i, due to the formation of twin-2 is calculated as,

$$\Delta\Gamma_i = \frac{1}{N_i}\sum_{s=1}^{N_i}(\rho_s^{after\,twin-2} - \rho_s^{before\,twin-2}) \tag{4.1}$$

where ρ_s is the dislocation density of slip system, s, in the region either near the twin center or impingement site. N_i is the number of slip systems in each mode: prismatic, basal, or pyramidal-I.

Figure 4.8 shows the change in the total average stored dislocation densities per slip family, $\Delta\Gamma_{prismatic}$, $\Delta\Gamma_{basal}$,and $\Delta\Gamma_{pyramidal-I}$, that accrues due to the formation of twin-2 for d between $1t$ to $50t$. The results show that twin-2 does not generate additional dislocation densities of any kind near the center of the twin-1, indicated by hollow box symbols in Figure 4.8. However, near the twin-1 tip, the total stored basal dislocation density increases by $\sim 6 \times 10^{12}$ for even the smallest precipitate spacing considered, $d = 1t$, and increases up to $\sim 7.2 \times 10^{12}$ for $d = 50t$, shown by solid markers in Figure 4.8b. The total stored pyramidal I dislocations also increased with the formation of twin-2, however, to a much lesser degree. The increase in total stored pyramidal-type I dislocation densities ranges from $\sim 0.9\times10^{10}$ to -2.7×10^{10} for the corresponding d ranges from $1t$ to $50t$, seen in Figure 4.8c. Pyramidal-type I densities steadily increased with increasing d. The development of twin-2 is observed to increase the local concentration

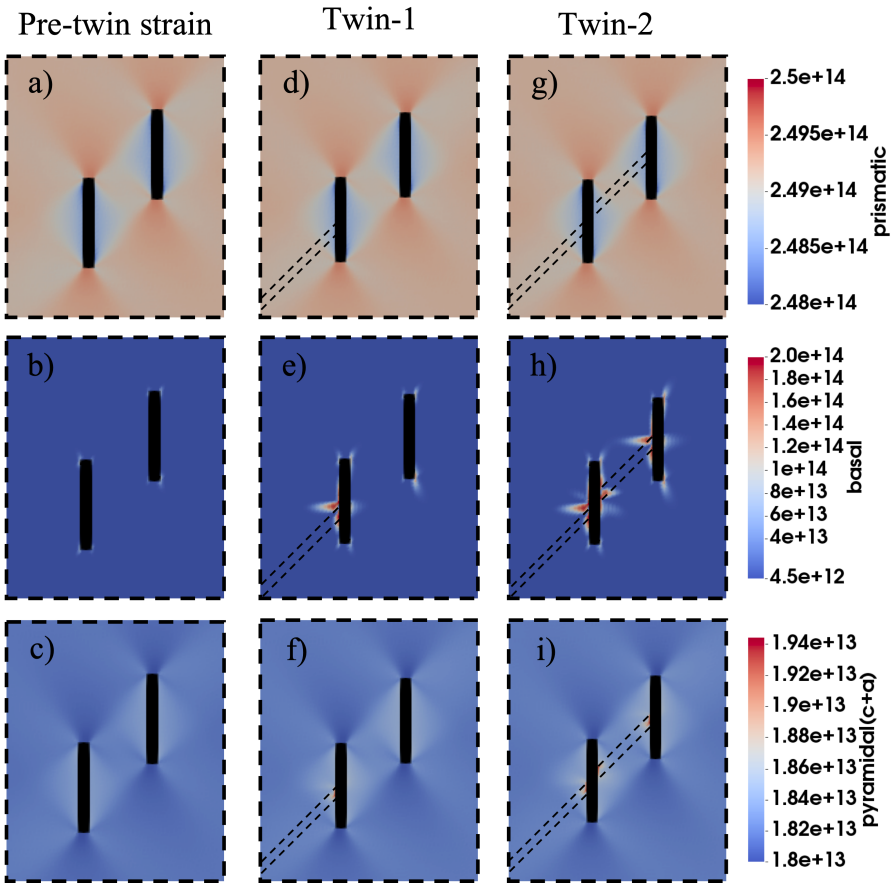

Figure 4.7: The total prismatic, basal, and pyramidal-I dislocation densities that arise after each stage of the simulation (pre-twin straining, formation of twin-1, and formation of twin-2). The twin boundaries are outlined by black dashed lines, and precipitates are covered by black boxes.

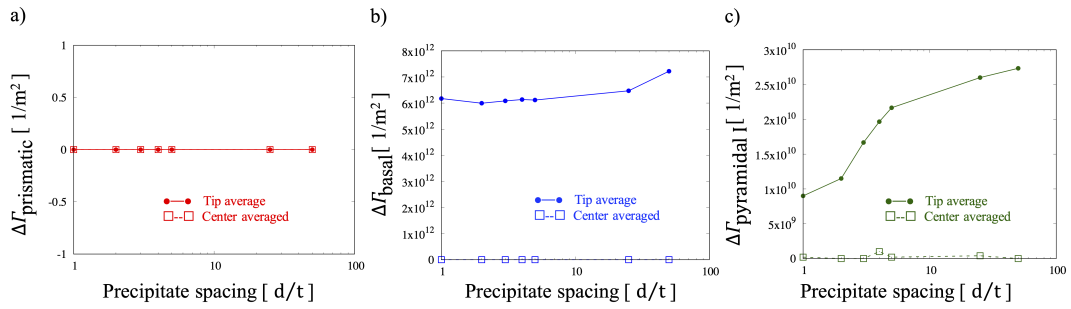

Figure 4.8: Increase in total stored dislocation density due to the formation of twin-2 at the tip of twin-1 near precipitate-1 and center of twin-1 boundary (see Figure 4.6a) for (a) prismatic, (b) basal, and (c) pyramidal-I slip modes. Please note, the horizontal axis is plotted on a log scale.

of defects in ω_{obt}. Overall, the interaction between twin-2 and precipitate-1 provides not only driving stress favorable for twin-1 growth (shown in Figure 4.6), but also supplies the dislocation structures that can support the growth of twin-1 in the region ω_{obt}.

4.8 Two-step twin growth mechanism

It is generally thought that twin growth in precipitate hardened Mg-alloys is difficult because the elastically hard precipitates can pin migrating twin boundaries. This notion mostly does not account the effect of precipitates on twin front propagation. Instead, most of these studies directly start with a fully propagated twin and the migration of the twin boundaries through twin thickening in the twin plane normal direction [66]. Here, a mechanism is identified that allows twins to thicken around an array of precipitates, beginning with a newly propagating twin. Typically, the twin is thought to be arrested; however, when the approaching twin is of comparable thickness as the precipitate, the proposed two-step mechanism provides an alternative and easier approach for twins to engulf precipitates, distinct from the studies that only treat twin growth as the translation of the entire twin boundary in the twin-plane-normal direction [96, 97, 193, 167].

The analysis suggests that the two-step bypass mechanism could explain the experimentally observed asymmetric twins and serrated morphology of twin boundaries in the presence of precipitates [5]. When twin-1 expands around the precipitate, its growth is easier along one side. For all the precipitate spacings considered here, the upper boundary gains sufficient driving forces to migrate while the lower twin boundary does not. Twin growth would initiate where twin-1 and the precipitate come together at an obtuse angle, leading to the formation of serrated twin boundary structures, as schematically illustrated in Figure 9a. Such serrated twin boundary structures are observed in the post-mortem TEM micrographs of heavily twinned AZ91 with dispersions of $Mg_{17}Al_{12}$

basal-plane precipitates, see Figure 4.9b [8]. Serrated features are exhibited by white arrows and relatively straight twin boundaries are highlighted by white dashed lines, consistent with our simulations. The two-step twin growth mechanism described here helps to explain how large twin domains develop through the interactions of propagating twins and precipitates.

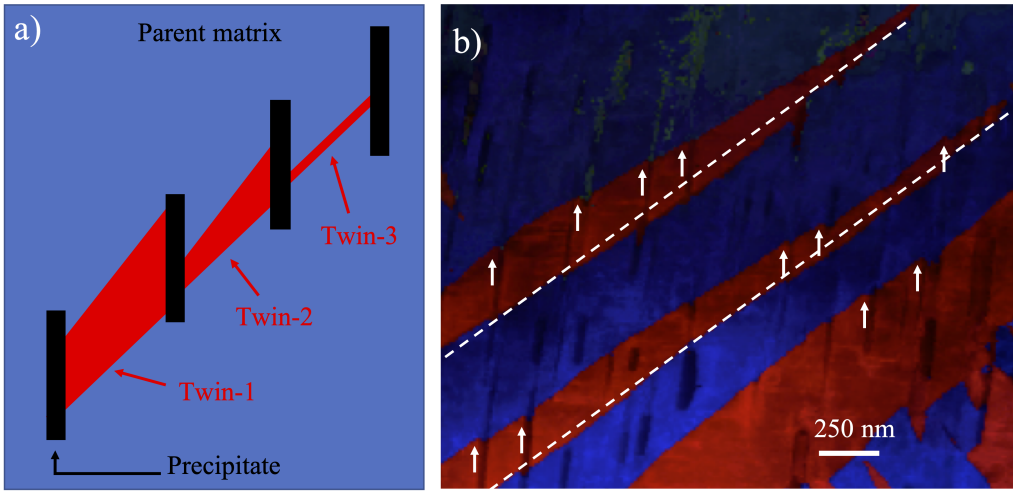

Figure 4.9: a) Schematic representation of three successive twins and the migration of their twin boundaries. b) TEM micrograph showing serrated structures, pointed out by white arrows, and twins that have grown preferentially along a single twin boundary while the other boundary remains relatively flat, highlighted by dashed white lines. Micrographs adopted with permissions from Elsevier, Leu et al. [8].

There is also the possibility that a second twin of the same variant could independently formed, and it intersects with the same precipitate as the first twin but on two opposing sides of the precipitate. If this were the case, then the site where the second twin intersects the precipitate could occur anywhere along the long side of the precipitate. Two twins independently intersecting the same precipitate may help to mutually relieve their backstresses if the location of their intersection sites were positioned near each other and on opposite sides of the precipitate. Any misalignment of the two independent twins could cause preferential growth of one of the twin boundaries over the other depending on how the two twins are offset from each other.

4.9 Conclusions

An elasto-viscoplastic fast-Fourier transform (EVP-FFT) model has been used to calculate the micromechanical fields and dislocation content associated with the interaction of a twin lamella and a precipitate at various stages of twinning. It is reasoned that an initial thin twin can impinge upon a precipitate and cause another twin to form on the other side of the precipitate. The interactions between the precipitate with the impinging twin and the subsequent twin change the local stress fields and dislocation content. The key findings are summarized below:

- Precipitates can help facilitate twin growth by a two-step mechanism. First, the initial propagation and impingement of a twin on a precipitate causes a local stress concentration to develop on the opposite side of the precipitate. Secondly, the formation and propagation of another twin from the far side of the precipitate counteract the backstresses that develop from the impingement of the initial twin. The augmented twin stresses along the boundaries of the initial twin and support its growth without any additional external macroscopic loading.

- The amount of relaxation provided by the newly formed second twin on the first twin is related to the length of the second twin, which, in precipitate-hardened AZ91, is mostly determined by the precipitate spacing, d, a microstructural feature that can be controlled through alloying and heat treatment. A precipitate spacing that is five or more times the twin thickness allows for nearly the greatest enhancement of the driving stresses for twin growth.

- In addition to driving stresses, the propagation of twin-2 also increases basal a and pyramidal-I $\langle c + a \rangle$ dislocation densities near the twin-1 impingement site, where twin-1 growth is likely to initiate. The proposed two-step mechanism thus supplies

twin-1 with both large driving stresses and appropriate dislocations near the twin boundaries that can facilitate twin growth.

Chapter 5

The effects of free surfaces on deformation twinning in HCP metals

5.1 Introduction

Deformation twinning in hexagonal close-packed (HCP) crystalline metals, like Mg and Ti and their alloys, is a prevalent mode of plastic deformation due to the scarcity of easy dislocation slip modes. Unlike crystallographic slip, deformation twins develop as 3D subcrystalline domains, which are significantly reoriented from the matrix crystal and impose a finite amount of shear. $\{10\bar{1}2\}$ tensile twins in Mg and Ti, for instance, reorient the crystal by 86.3° and 86.4° and their characteristic shears are 12.9% and 17.4%, respectively. Consequently, twin domains can generate heterogeneous internal stress within a crystal that can affect strain hardening, overall mechanical response, and trigger damage[199]. Thus, understanding the changes induced in the microstructure and micromechanical fields by twinning is important for establishing the structure-property relationship of HCP metals that twin.

A variety of experimental techniques, including neutron diffraction, X-ray diffraction,

and scanning (SEM) and transmission electron microscopy (TEM) in conjunction with digital image correlation (DIC) have been employed to understand the effect twins have on the evolution of internal stresses [102, 103, 41, 9, 104, 64]. X-rays allow for non-destructive investigation of the internal microstructure, however, it can be limited in its spatial resolution and interaction volume [105, 106]. Electron microscopy techniques offer higher resolution, faster data acquisition, and can collect data over larger areas of the specimen; however, the sample preparation required for these techniques introduces free surfaces near the areas of interest [106]. Due to the nature of the electron microscopy techniques, the interaction volume of the electrons and the sample surface are bounded due to the limited penetration depths of the electrons, often less than 100 μm for SEM and less than 1 μm for TEM [106]. For this reason, sample preparation requires the removal of sections of the material until the region of interest is within 100 μm of the free surface for SEM or the creation of thin films with a thickness below 1 μm from the bulk sample for TEM. In both cases, the sample preparation process introduces one or two free surfaces near the region of interest for SEM or TEM, respectively.

The regions of a sample adjacent to free surfaces are physically less constrained than the regions within the bulk, thus prompting unique material behavior. A few works have studied the influence of free surfaces on dislocations and the overall mechanical strength and ductility. For example, Greer et al. suggested a "starvation model" that explains, for thin samples, that the rate of dislocation loss at the free surface can exceed the dislocation multiplication rate, resulting in a limited amount of dislocations available to carry out plastic deformation, consequently hardening the material [108, 107, 109]. Others have described a "truncation model", whereby the truncation of Frank-Read sources by the free surfaces lead to single-ended dislocation sources with shorter dislocations line lengths that increase flow stress [102, 200, 201]. Experimental TEM evidence has indicated that the escape of dislocations through free surfaces can result in stress, strain and dislocation

density gradients between the bulk and surface of the sample [110, 111, 112]. The global response of the specimen can be dominated by the surface regions when the sample dimensions are reduced. These results are supported by computational finite element method (FEM) analysis [113]. Furthermore, TEM has shown that free surfaces can directly influence the distribution of dislocation pile-ups near the free surface, which could consequently influence plastic response of the material when compared to the bulk [114].

Computational efforts have also been made to describe the effects of free surfaces on dislocation behavior. Atomistic studies have shown that, in thin samples, the image forces on dislocations near free surfaces are different and can cause the Peierls stresses for dislocation motion to be lower and dislocation mobility to be higher than in the bulk [115, 116, 117, 118, 119]. Similar conclusions have been drawn using molecular dynamics (MD) based methods [121, 120]. Molecular dynamics simulations have also shown that the stress required for dislocation nucleation near free surfaces are lower than the bulk [115]. Dislocation dynamics simulations have also been implemented in order to capture image force effects on near-surface dislocations that assist in their fast ejection from the surface [123, 124]. Crone et al. explained that voids, another source of free surfaces, in Al provided weaker strengthening effects than predicted by classical calculations of Lothe due to long-range image forces that act on the entire dislocation further away from the free surface [125, 126]. While free surface effects on dislocation behavior has been a topic of research for some time, the same treatment of free surfaces effects has not yet been extended to deformation twinning. One study by Datta et al., using first-principles, found that twins in Ni are harder to nucleate in thin films than the bulk due to the localization of the electronic structure near free surfaces [127]. Unlike dislocations, the dimensions of twins can be grain-scale, which can result in extensive long-range changes in the local stress states [66]. Any effect of surfaces on local twin stresses can translate

to a change in their propagation and growth. The experimentally measured stresses and strains via SEM or TEM could be significantly different when compared to the interior of the bulk sample. Thus, the observations and analysis derived from near free surface techniques on lab scale samples may not directly translatable to the bulk.

In this work, a mesoscale crystal plasticity-based model is employed to quantify free-surface effects and identify those specific regions around the twin that may be the most affected and can influence further twin development. Free surface relaxations are shown to enhance the stresses along the twin boundary and ahead of the twin tip that would support propagation and growth under applied deformation. The results also find that additional slip modes are activated as a result of the free surface. Comparison with measurements of twin stresses in Ti demonstrates the substantial effect of free surface on in-plane stress fields. These findings can help in bridging properties between lab-scale samples and their bulk counterparts, and potentially reconcile differences between modeling predictions and experimentally measured twin characteristics, such as stress and volume fraction.

5.2 Modeling free surfaces

In the EVP-FFT framework, virtual free-surface formation is simulated in two steps, closely mimicking the sample preparation process. First, the imposed macroscopic load is lifted from the deformed unit cell. Then, a region of virtual material is "removed" via relaxation under zero macroscopic stress until an equilibrium state is reached. The former enforces the unloaded state of the specimen and is achieved in the EVP-FFT simulation by maintaining zero macroscopic stress. The material removal via relaxation is accomplished by reducing the elastic stiffness in the removed region of unit cell towards zero, which approximates the response of a pseudo-vacuum. While the periodic

boundary conditions are enforced, the presence of this pseudo-vacuum region mechanically disconnects each unit cell from its periodic repetitions in the free surface normal direction. By decreasing the elastic stiffness, the material becomes super compliant and the related stresses decrease rapidly. In turn, these stresses affect the plastic strain in the remaining material and new micromechanical fields are recalculated until a new energetic equilibrium is reached. The simulation cell is re-equilibrated over five steps, during which the free surface normal stresses are relaxed to zero. There are no appreciable differences in the micromechanical fields with additional relaxation steps past five steps.

The aforementioned method for free surface creation and relaxation was used to represent a situation that appears in either SEM or TEM analysis. In the SEM case, a 2D plane of interest is selected from the center of the bulk simulation cell. All material on one side of the 2D plane are then removed, as described above, to introduce a free surface. The calculated values along the newly created free surface are considered to be affected by the free surface, like those measured experimentally. These predicted free-surface fields only pertain to a thin volume of material near the free surface, as regions far away from the free surface are expected to experience different fields. Accordingly, the values along the same 2D plane within the bulk material, before the free surface creation, represent the bulk response of the material. Similarly, in the TEM case, a thin sheet of material (three voxels thick) is selected from the center of the 3D simulation cell. All materials above and below the thin sheet are removed, introducing two free surfaces. The calculated fields represent free-surface fields, while those generated in the same 2D plane before material was removed are referred to as bulk fields. In contrast with SEM samples, the predicted free-surface fields pertain to the entire TEM sample, since the foil is sufficiently thin such that there are no appreciable gradients in the micro-mechanical fields in the through-thickness direction.

5.3 Material properties

The model only requires two sets of material parameters, the elastic constants and CRSS values for the allowed slip modes. Two materials, pure Mg and commercially pure Ti (grade II), are considered in the calculations that follow. The elastic constants C_{11}, C_{12}, C_{13}, C_{33} and C_{44}, of Mg are 59.75, 23.24, 21.7, 61.7 and 16.39 GPa, respectively [168]. The prismatic $\langle a \rangle$, basal $\langle a \rangle$ and pyramidal $\langle c + a \rangle$ slip modes are made available with constant CRSS of 35.7, 3.3, and 86.2 MPa, respectively [194]. Strain hardening is not considered and, therefore, the CRSS values remain constant throughout the simulation. For Ti, the elastic constants C_{11}, C_{12}, C_{13}, C_{33} and C_{44} are 162.4, 92.0, 69.0, 180.7 and 46.7 GPa, respectively [168]. The CRSS values for the prismatic $\langle a \rangle$, basal $\langle a \rangle$ and pyramidal $\langle c + a \rangle$ slip modes are 90.5, 170.0 and 210.0 MPa, respectively [202].

5.4 Twin formation inside a bulk grain

First, a model twin microstructure is used to examine the changes induced by free surface creation on the micromechanical fields around a twin in two different scenarios: after unloading from the deformed state that induced the original twin and after additional external loading. In both cases, the fields from within the bulk and in a TEM film are compared.

Figure 5.1a shows the 3D model simulation cell containing one $\{10\bar{1}2\}$ tensile twin (in red) embedded in a Mg grain (in gray). A buffer layer surrounding the cell is used to represent the response of the surrounding polycrystalline material. Periodic boundary conditions are applied in all directions. The cell size is 174x174x174 voxels and the buffer layer is 24 voxels thick, sufficiently large to minimize effects of overlapping fields from periodic images. The orientation of the grain, in Bunge convention, is (0°, 46.7°,

0°) orienting the c-axis of the parent crystal aligned at a 46.7° angle counter-clockwise away from the +Z-direction in the YZ plane, as shown in the hexagonal inset in Figure 5.1d. Following the twin/matrix orientation relationship, the $(01\bar{1}2)$ twin variant is oriented with its twin-plane normal parallel with the Z-direction and the $[0\bar{1}11]$ twin-shear direction along the Y-direction.

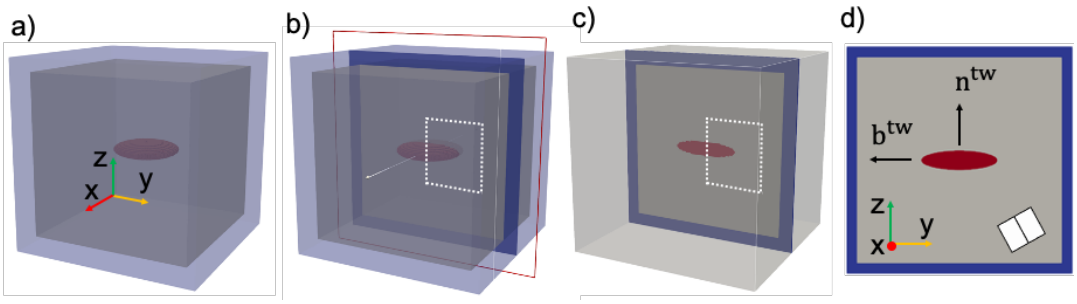

Figure 5.1: Schematic representation of an oblate spheroid twin embedded in a Mg grain. a) The ellipsoidal twin (red) is formed in a parent matrix grain (gray). The parent matrix is surrounded by a homogeneous layer (blue) with uniformly distributed crystal orientations that approximates a polycrystalline medium. b) The red outline highlights the 2D slice, parallel to the Y-Z plane, taken from the center of the simulation cell. The values on this slice represent the bulk material response. c) A thin film is formed by taking a central section out of the 3D simulation. The layers in front and behind the thin film are "removed" by setting their elastic properties to be super compliant. d) A 2D view down the center of the twin. 2D slices can be taken from either the bulk (from Figure 1b) or at a free surface (from Figure 1c). The crystallographic orientation of the parent matrix is shown in the hexagonal inset.

The grain without the twin is first subjected to a shear strain of 0.2% in the YZ-direction, resulting in a twin-plane resolved shear stress (TRSS) of about 38 MPa. To form the twin, the predetermined twin domain is reoriented according to its twinning relationship with the parent matrix orientation, while under the applied strain. The geometry of the twin resembles an oblate spheroid with a minor axis of 15 voxels and a major axis of 60 voxels long. A characteristic twin shear of 12.9% is then slowly incremented on the twin plane in the twin shear direction in order to form the twin over 2000 steps. In each step, the strain and stress tensor fields are calculated everywhere in

the simulation cell using the EVP-FFT formulation presented in Chapter 2.

5.5 Stress relaxation during free surface formation

The stress fields on a 2D plane of interest within the bulk of the material and from the same plane taken along the free surface are compared. A small region centered around the twin tip, outlined in white dashed lines in Figure 5.1b and 5.1c, is taken for inspection; this subsection is truncated on the left side at the center of the twin. In Figure 5.2, the left column shows the stress fields in the bulk, the middle column shows those on the free surface, and the right column shows the difference between the two. The twin boundary is outlined in black for clarity.

The top row, Figure 5.2a-c, shows the normal stress out-of-plane in the X-direction, σ_{xx}. The second row, Figure 5.2d-f, and third row, Figure 5.2g-i, show the in-plane normal stress components in the Y-direction and Z-direction, σ_{yy} and σ_{zz}, respectively. The positive regions, in red, indicate a tensile stress, while the negative regions, in blue, represent compressive stresses. Inside the twinned region in the bulk, σ_{xx} is compressive (Figure 5.2a), while σ_{yy} is near zero (Figure 5.2d) and σ_{zz} is tensile (Figure 5.2g). Both above and below the center of the twin, the stresses are tensile. The regions above the twin tip are tensile, while below the twin tip they are mostly compressive. Along the free surface, the σ_{xx} field is uniformly zero everywhere (Figure 5.2b), as expected for a free surface. The other two shear stress components, σ_{xy} and σ_{xz}, are also uniformly zero, as expected, but not shown in the interest of space. In the free surface sample, we find that the σ_{yy} and σ_{zz} fields are nearly identical (Figure 5.2e and 5.2h), and compared to the same fields in bulk, the intensity of these stresses has reduced (Figure 5.2d and 5.2g).

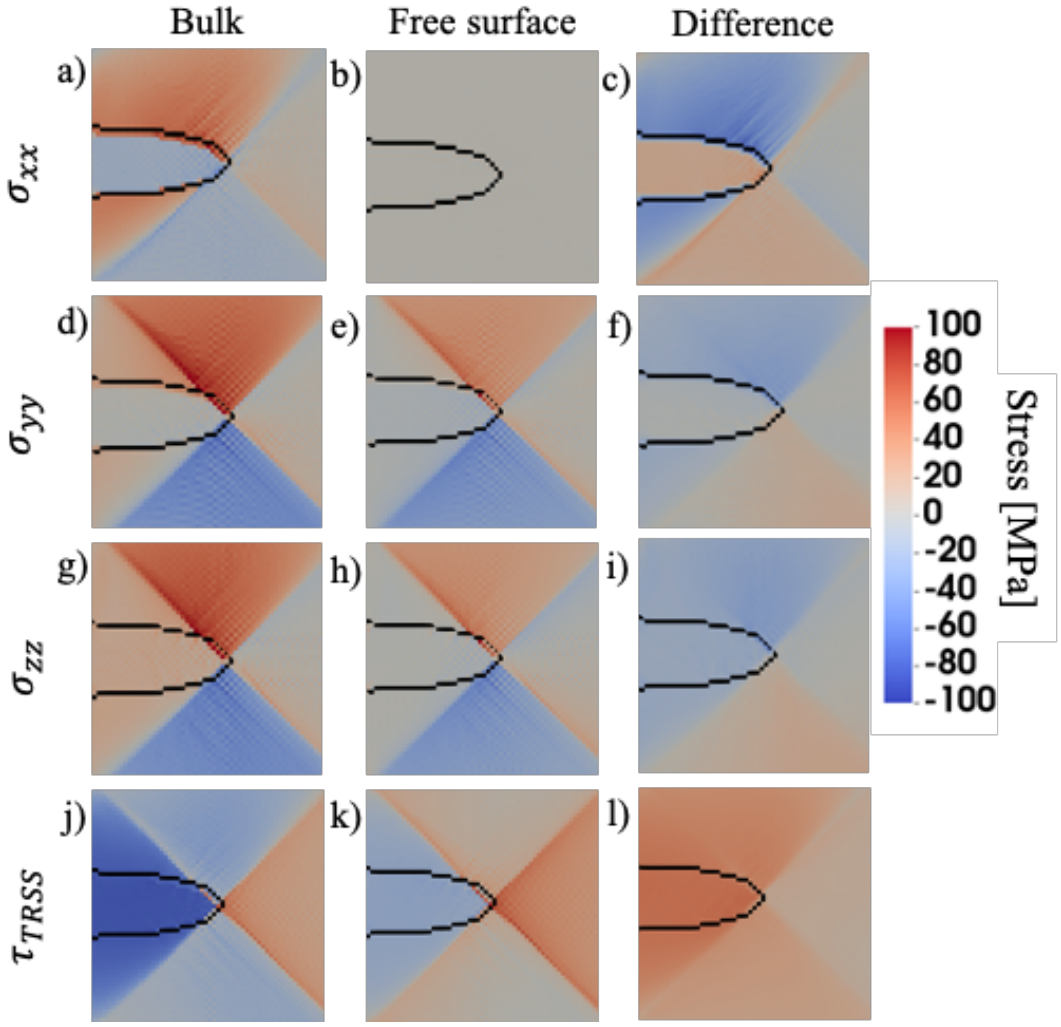

Figure 5.2: Comparison of the simulated σ_{xx}, σ_{yy}, σ_{zz} and τ_{TRSS} stress field distribution found within the bulk (left column) and within the thin film (middle column). The right column shows the difference in stress levels between the bulk and the thin film. a-c) corresponds to σ_{xx}. d-f) corresponds to σ_{yy}. g-i) corresponds to σ_{zz}. j-l) corresponds to τ_{TRSS}.

5.6 TRSS fields in the bulk vs at the free surface

Figures 5.2j and 5.2k show the twin plane resolved shear stress, τ_{TRSS}, fields around a twin lying in the bulk and at the free surface, respectively. Both fields are heterogeneous in stark contrast to the homogeneous τ_{TRSS} field of $\sim$ 38 MPa across the crystal before the twin was formed. In the case of the bulk twin, the τ_{TRSS} in regions inside and immediately

surrounding the twin are negative, meaning that they act in the anti-twinning sense. The drop in stress from 38 MPa before twinning to the severe anti-twinning values (e.g., −85 MPa) signifies a strong "backstress" [203, 132, 176]. When generated along the twin boundary, this backstress restricts thickening of the twin or growth normal to the twin plane. At the same time, a positive τ_{TRSS}, ~ 60 MPa, develops in the crystal in front of the twin and is the strongest directly at the twin tip. This "forward stress" drives the twin tip to propagate. These results agree well with previously reported works [203, 132, 185].

The τ_{TRSS} field in the thin film for the same 2D plane shows many interesting differences compared to those in the bulk. As seen in Figure 5.2l, the TRSS fields in the thin film have increased everywhere compared to the bulk, in ways that generally support twin tip propagation and thickening. Notably, the strong forward stress concentration directly in front of the twin increases to 70 MPa from ~ 60 MPa, and the regions above and below the twin tip that were previously negative (anti-twinning) in the bulk have become positive (for twinning). Inside the twin domain and near the twin boundaries, where the values of the backstress were the most severe, the TRSS fields have increased to about −30 MPa, reaching values almost three times higher in thin film than that in the bulk.

5.7 Plastic accommodation in the bulk vs at the free surface

The stresses generated both inside and outside the twin region are sufficient to locally activate slip. In the case of the twin in the bulk, Figure 5.3a-c identifies the total shear strain from each slip mode in Mg: basal $\langle a \rangle$, prismatic $\langle a \rangle$, and pyramidal-I $\langle c + a \rangle$ slip modes. Generally, basal slip in the surrounding parent matrix accommodates most of

local deformation imposed by the twin. Relatively large amounts of basal slip accumulate in regions that radiate diagonally from the twin tip (Figure 5.3a), while prismatic slip is limited (Figure 5.3b) and pyramidal-I slip is only activated inside the twin region (Figure 5.3c).

To identify the types of dislocations that would be promoted ahead of the (stationary) twin under further loading and/or twin development, Figure 5.3d-f presents the fields of maximum absolute resolved shear stress (RSS) among the slip systems belonging to each slip mode. The maximum RSS serves to indicate the slip system most likely to activate, however, not the only system that could be activated. It can be seen in Figure 5.3d that the driving stress for basal slip is highly concentrated in regions that lie diagonally from the twin tip and are close to the CRSS of 3.3 MPa, suggesting basal activation is likely. Basal slip is not likely, however, in the twin domain, where the driving stress is almost zero. The RSS field for prismatic slip in Figure 5.3e is split into two regions separated by a diagonal centered at the twin tip. In neither regime is prismatic slip likely. The stresses in the upper left region reach ~ 21 MPa and within the twin are ~ 25 MPa, both below the CRSS of 35.7 MPa. The RSS field for pyramidal-I slip is moderately high within the twin, in the matrix near the twin boundary, and concentrated at the twin tip, as seen in Figure 5.3f; however, they are still well below the CRSS of 86.2 MPa, indicating that they are not likely to be activated. According to this analysis, basal slip was the only slip mode that the twin stress fields promote in the bulk.

Starting with the twin in the bulk, the creation of free surfaces is simulated by relaxing the stresses in the out-of-plane directions to zero to mimic the conditions of a thin film. Figure 5.3g-i presents the total plastic accommodation by each slip mode of the microstructure that occurred only from the introduction of the free surfaces. As seen in Figure 5.3g, the free surface creation develops concentrated regions of basal slip activity that lie diagonal from the twin tip. Similarly, plastic strain accumulated by prismatic

slip in a region extending diagonally across the twin tip, moving from the bottom-left to top-right, see Figure 5.3h, although to a much lesser degree than basal slip. A little plastic strain by pyramidal slip is predicted to accumulate in a concentrated region just at the twin tip, Figure 5.3i.

In contrast to bulk RSS fields (Figures 5.3d-f), Figure 5.3j-l show the maximum absolute RSS distributions in the thin film for the most stressed basal, prismatic, and pyramidal-I slip systems. These RSS fields help to identify the slip activity promoted by twinning in the thin film. Similarly to the bulk case (Figure 5.3d), in the thin film (Figure 5.3j) the maximum RSS for basal slip is strongly concentrated in fine regions emanating diagonally from the twin tip, with values at the CRSS of 3.3 MPa. Additionally, moderately high levels of RSS develop in the parent matrix but little driving stress for basal slip develop within the twin region itself. The prismatic RSS fields for the thin film (Figure 5.3k) have completely reversed from those in the bulk (Figure 5.3e). The driving stresses in the upper left region, that were previously high in the bulk, have been reduced while the regions in the bottom right, that were previously low, have been enhanced. In Figure 5.3k, the RSS almost reaches the CRSS, suggesting prismatic slip activity in a concentrated region radiating diagonally from the twin tip. Lastly, Figure 5.3l shows the maximum RSS distribution for pyramidal slip in the thin film. In the bulk (Figure 5.3f) the regions of maximum pyramidal RSS that were previously highest were inside twin domain. In contrast, in the thin film (Figure 5.3l) the pyramidal RSS values in the twin are relatively low, around 25 MPa. At the same time, the stress concentration at the twin tip in the parent crystal has increased to about 65 MPa. However, it is still not sufficient to activate pyramidal slip. Thus, in the thin film, both prismatic slip and basal slip are activated ahead of the twin, unlike in the bulk, where only basal slip was activated.

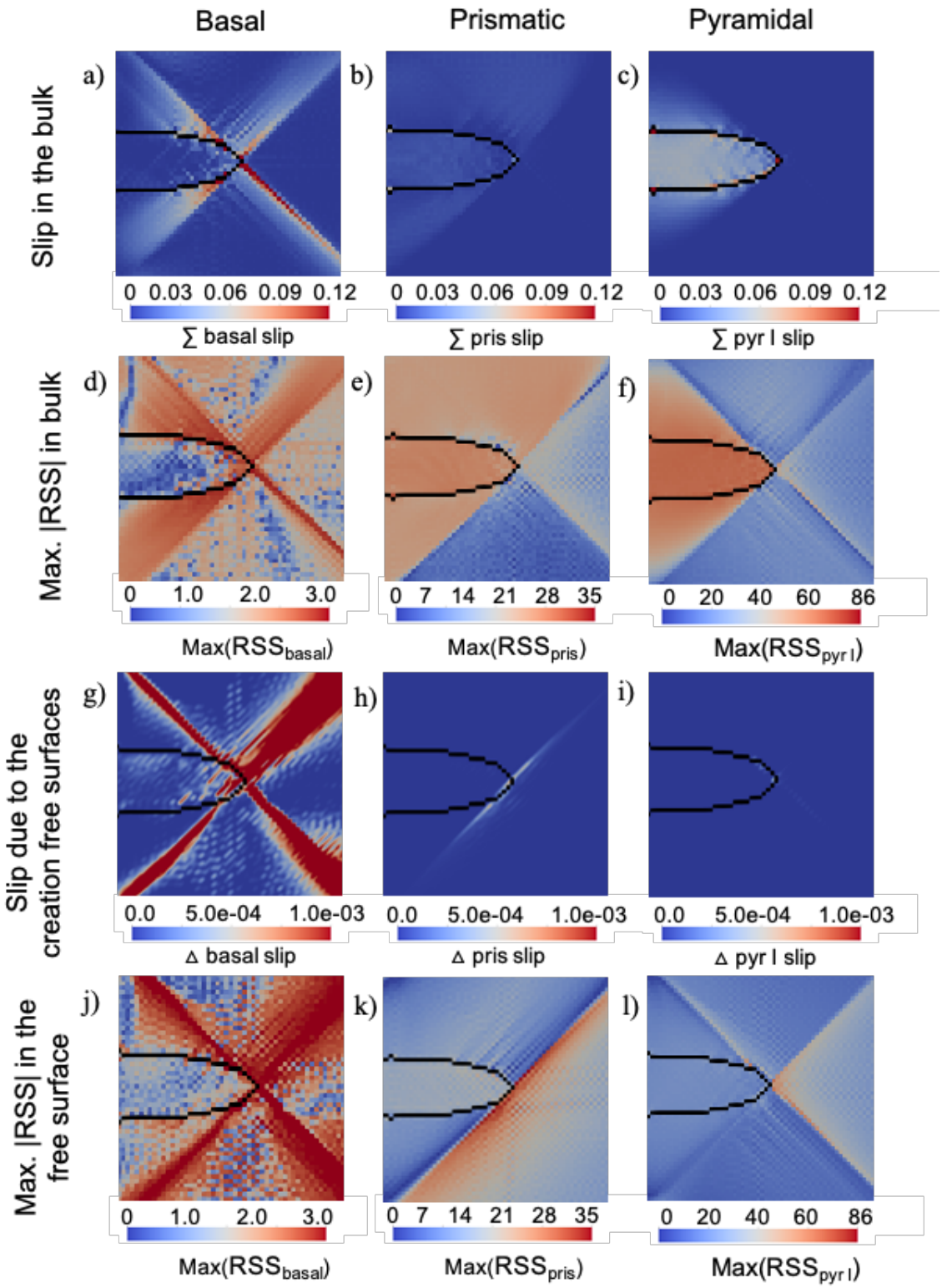
Basal
Prismatic
Pyramidal
Slip in the bulk
a)
b)
c)
0 0.03 0.06 0.09 0.12
∑ basal slip
∑ pris slip
∑ pyr I slip
Max. |RSS| in bulk
d)
e)
f)
0 1.0 2.0 3.0
0 7 14 21 28 35
0 20 40 60 86
Max(RSS basal)
Max(RSS pris)
Max(RSS pyr I)
Slip due to the creation free surfaces
g)
h)
i)
0.0 5.0e-04 1.0e-03
Δ basal slip
Δ pris slip
Δ pyr I slip
Max. |RSS| in the free surface
j)
k)
l)
Max(RSS basal)
Max(RSS pris)
Max(RSS pyr I)

Figure 5.3: The total accumulated slip that develops as a result of the initial externally applied load and the formation of the twin. The values represent the sum of the accumulated slip amongst all a) basal, b) prismatic, and c) pyramidal type-I slip systems. The distribution of maximum absolute RSS amongst the (d) basal, (e) prismatic, and (f) pyramidal systems in the bulk. The total plastic slip accumulated only during the free surface relaxation process for g) basal, h) prismatic, and i) pyramidal slip. The distribution of maximum absolute RSS in the (j) basal, (k) prismatic, and (l) pyramidal systems in the free surface.

5.8 Twin thickening in the bulk vs in a thin film

Next, the difference in the propensity for twin propagation and growth between the twin in the bulk and in the thin film under additional externally applied load is investigated. In simulation, the same shear is applied to both the bulk sample, Figure 5.1b, and the thin film sample, Figure 5.1c. Figure 5.4 compares the TRSS fields that develop from deforming the bulk sample with those from deforming the thin film. In both cases, an external shear of 0.2% is applied along the Y-direction (parallel to twinning shear) in the Z-plane (parallel to the twinning plane). The two fields show many differences. In the bulk, the TRSS is negative inside the twin matrix and along the lateral regions of the twin just outside the twin boundary in the parent matrix, with values of about -34 MPa. At the same time, the TRSS in the thin film is positive everywhere inside the twin and the surrounding parent matrix, with values of about 40 MPa. In the bulk, the values were negative for these same regions. In both cases, a cone-shaped stress concentration region develops at the twin tip, reaching values of 70 MPa and 88 MPa for the bulk and thin film cases, respectively. In the bulk case, the regions just above and below the twin tip are near zero, while the same regions in the thin film case reach up to 70 MPa. Thus, the twin loaded in a thin film has a higher propensity to propagate forward and grow thicker than the same twin loaded in bulk.

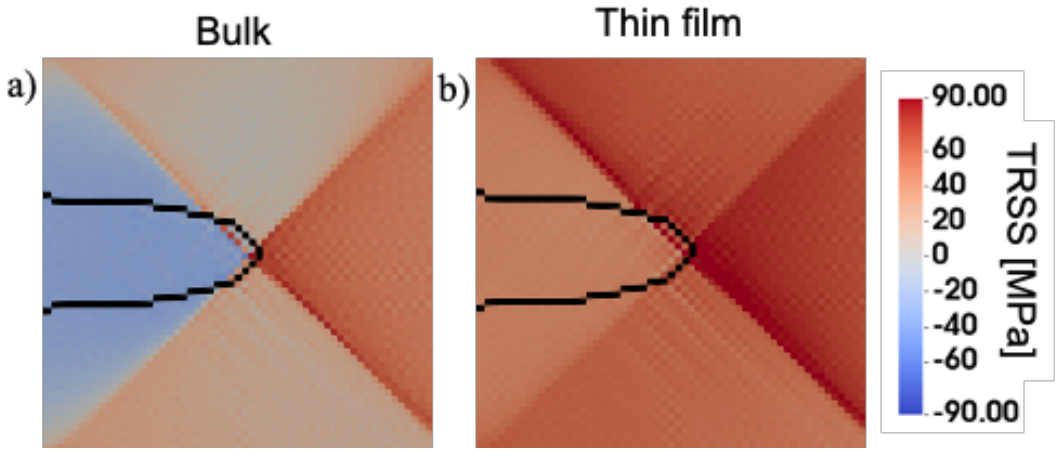

Figure 5.4: Comparison of the TRSS fields that develop with additional macroscopic YZ-shear straining applied after the twin has been formed. TRSS fields that develop when deforming the (a) bulk and (b) thin-film virtual samples.

5.9 Free surface effects on twin morphology

The calculated TRSS field changes shown in Figure 5.2l indicate that the local driving forces for twin development are altered by the free surface. Under the same continued loading, a twin in the bulk could, therefore, grow and adopt a different morphology than the same twin observed in the thin film. In the bulk, in Figure 5.2j, the twin domain and the parent matrix near and along the twin boundaries experience large back stresses, resisting twin thickening normal to the twin plane. The region in front of the twin, however, is highly positively stressed, promoting lengthwise twin tip propagation. In contrast, in the thin film, as depicted in Figure 5.2k, the regions inside the twin and along the twin boundaries experiences less anti-twinning stress. The backstresses in these regions are up to three times weaker in the thin film than in the bulk, providing less resistance to twin thickening. Consequently, twins in the bulk should have higher aspect ratios (i.e., thinner twins) than twins near free surfaces.

Reduced backstresses in the lateral regions of the twin imply that thickening of the twin near free surfaces would receive less resistance than inside the bulk, potentially re-

sulting in larger twin volume fractions near the surface under an applied load. This trend is consistent with some experimental observations of twins in AZ31 Mg alloys. The twin volume fraction obtained through near-free surface techniques, such as EBSD in an SEM, on AZ31 deformed to 0.2% strain is approximately 3.5% [204]. In the same material (same alloying and texture) and loading condition, neutron diffraction techniques measured a twin volume fraction more than 50% lower in the interior of an AZ31 alloy deformed to 0.2% strain [40]. While some differences may be expected due to the assumptions these techniques made in extracting twin volume fractions, they cannot explain the substantial drop. Free surface effects could have helped make twin growth easier by increasing the driving force for twinning all around the twin boundary.

Additionally, the analysis suggests that the shape of the twin tip could differ between the bulk twin and the thin film twin. In Figure 5.2k for the thin film, we observe that the regions directly above and below the twin tip in thin film have approximately 20 MPa TRSS. In the bulk case, however, the same regions in Figure 5.2d, have backstresses of about -35 MPa. The introduction of free surfaces may cause this region to twin, while if it remained in the bulk, this event would be unlikely. In this case, the newly developed positive TRSS immediately surrounding the twin tip could be sufficient to alter the twin morphology, resulting in a severely blunted twin tip in the thin film case when compared to the bulk.

5.10 Free surface effects on slip activity

The results in Figure 5.3a-c indicate that mainly basal slip accommodates the twin in the matrix while pyramidal slip occurs only in the twin and prismatic slip is limited everywhere. However, as seen in Figure 5.3g-i, by introducing free surfaces, basal and prismatic slip can be locally induced. The analysis points to a tendency for surface

characterization techniques to overestimate the amount of basal and prismatic slip around twin tips since some amount of dislocations will arise solely due to the free surface relaxation. This is further complicated by the disparity in the maximum RSS among prismatic and pyramidal slip systems in the bulk, Figure 5.3e-f, and in the free surface, Figure 5.3k-l. In the bulk, Figure 5.3e-f, the RSS for prismatic and pyramidal slip are insufficient to activate but are still substantial, within 20% of the CRSS. Under more complex microstructures and loading conditions, the regions with enhanced prismatic and pyramidal RSS may activate. However, these enhanced stresses diminish greatly in the free surface. Instead, other regions become more favorable for prismatic and pyramidal slip, Figure 5.3k and 5.3l, respectively. Recent work by Jiang et al., show both $\langle a \rangle$ and $\langle c+a \rangle$ dislocations are observed at the twin front during in-situ deformation that coincides well with the predicted regions of enhanced RSS on basal, prismatic, and pyramidal slip systems in the thin film, seen in Figure 5.3j-l [163]. Observations of plastic accommodation of twins made with near surface techniques may not be translatable to twin/matrix plastic behavior inside the bulk. Evidently, the stress fields around twins are complex and the introduction of free surfaces near twins can dramatically change the stress fields.

5.11 Free surface effects on twin propagation

Next, the stress fields that develop after additional external load is applied to both the bulk and thin film containing the same twin is discussed. Three interesting features indicate different twinning behavior due to the free surface. First, backstresses still persist in the twin and the nearby surrounding parent matrix of the bulk, inhibiting twin growth, seen in Figure 5.4a. At the same time, in the thin film, Figure 5.4b, the stresses in the same regions show no backstresses, implying that twins near free surfaces

can grow thicker with a more blunted twin tip. Secondly, the forward stresses at the twin tip are stronger in the thin film case than the bulk, implying that the driving force for twin propagation is higher as well. Lastly, the TRSS fields that develop in the thin film are not symmetric about the twinning shear direction, unlike the bulk case. In the bulk material, the strongest TRSS concentration occurs at the twin tip; however, in the thin film case, both the twin front and region above the twin tip experience strong stress concentrations.

Deforming the thin film caused the development of inhomogeneous stress distributions around the twin, especially near the twin tip. These local stress concentrations may be enough to initiate twins of different variants to emit from the twin boundary or cause section of the twin front to propagate earlier than others. This might help to explain why many twin embryos are seen to be emitted from twin boundaries during some in-situ deformation studies [163]. Additionally, the heterogenous driving forces may cause the twin tip to propagate asymmetrically about the twinning shear direction upon loading.

5.12 Free surface effects on twin boundary characteristics

Thus far, our analyses of twin growth have been based on the sign and severity of TRSS fields near and along the coherent twin boundaries (CTB) of the lamellae. However, in some parts of the twin, particularly near its tip region, the twin boundary structure can be faceted and comprised of basal-prismatic (BP) or prismatic-basal (PB) boundaries that separate CTBs [205, 206, 138, 207]. Unlike the CTBs, the formation and migration of BP and PB boundaries are controlled by the normal stresses acting on these planes. In Mg, the separation of basal and prismatic planes are 5.21 Åand 5.55 Å, respectively

[203]. Thus, to migrate BP or PB boundaries, the normal stresses need to be tensile or compressive, respectively. Figure 5.5 illustrates the stresses, σ_{BP} and σ_{PB}, normal to the BP and PB boundaries that drive their mobility, respectively.

TEM observations of PB/BP facets in twin boundaries report facets several nm long [205, 206, 208, 209, 189, 210]. These lengths are significantly greater than predictions by atomistic simulations, where the facets are on the order of 4-6 atoms long [209, 211, 189, 212, 198, 72]. TEM measurements on thin foils are influenced by the free surface, while most atomistic simulations employ periodic boundary conditions that better approximates a bulk response. To determine whether free surface effects can help to explain the observed differences, we calculate the σ_{BP} and σ_{PB} fields taken within a plane in the bulk with that from an identical plane in a thin foil. In Figure 5.5, the left column shows the σ_{BP} and σ_{PB} stress fields in the bulk, the middle column shows those on the free surface, and the right column shows the difference between the two. The red regions indicate a positive tensile stress, while the blue regions represent a compressive stress. As seen in Figures 5.5a and 5.5d, in the bulk, σ_{BP} and σ_{PB} along the twin boundary are compressive and tensile, respectively, which is unfavorable for the formation and migration of the facets. After the creation of the free surface, however, σ_{BP} increases by about 40 MPa and σ_{PB} decreases by about 70 MPa, Figures 5.5c and 5.5F, respectively. This suggests that introducing free surfaces can help migrate the facets, consequently leading to longer facets, schematically illustrated in Figures 5.5g and 5.5h. The more favorable stress conditions near free surfaces can thus help to provide an explanation for the discrepancies between measurement and atomistic simulation calculations of twin facet size.

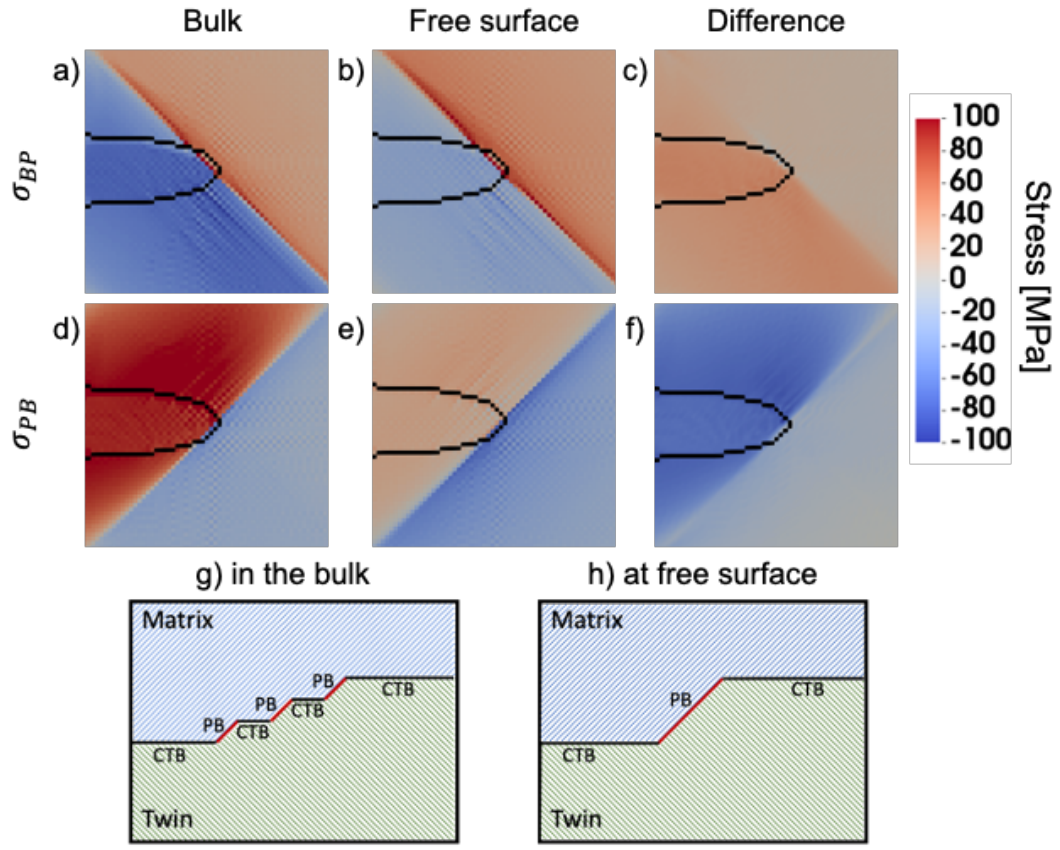

Figure 5.5: Distribution of normal stresses to PB and BP facets within the bulk (left column) and within the thin film (middle column). The right column shows the difference in stress levels between the bulk and the thin film. First and second rows correspond to stresses normal to BP and PB facets, respectively. Schematic representation of BP and/or PB facets in the bulk (g) and at the free surface (h).

5.13 Bridging free surface effects between lab-scale observations and bulk response

Additional surface relaxation calculations are performed in comparison with direct experimental measurements of twin stresses across a grain boundary in Ti [9]. Basu et al. employed a correlative technique using EBSD with DIC on commercial grade II titanium deformed at room temperature in an in-situ four-point-bend test [9]. The surface of the specimen was prepared for EBSD prior to deformation. Using DIC, they mapped the

grains in a small region of the microstructure in the twinned polycrystalline Ti sample, shown in the Figure 5.6a, taken from the tensile surface of the bent specimen strained to 18%.

This same region is digitized to create a pseudo-3D microstructure, consisting of columnar grains extending in the out-of-plane direction for simulation. The simulation cell size is $5x210x310$ voxels. For the twin in the model, the twin shear direction and twin plane normal lie in-plane as in the experiment [9]. The microstructure was compressed by 18% in the normal direction, out-of-plane. We consider two cases; the first one has a free surface on one side, formed by removing two layers in the out of plane direction, designed to compare directly with the EBSD-DIC measurement, and the second case considers the same twin but, hypothetically, in the bulk far from the free surface. Figure 5.6c compares the TRSS fields, taken along the line AB illustrated in the Figure 5.6b, crossing from a twinned region to the neighboring grain. The red symbols show the experimentally measured TRSS, the blue dots show the calculated TRSS in the free surface, and the black dots show the calculated bulk TRSS taken from a 2D slice at the center of the whole simulation cell. Compared to the experimentally measured values, the TRSS at the free surface (blue symbols) give a better comparison both qualitatively and quantitatively than those calculated within the bulk (black symbols).

The calculations show that the effect of the free surface is to lower the backstresses and stress concentrations produced in the neighboring grain at the twin/grain boundary junction. At the simulated free surface inside the twin but away from the grain boundary, TRSS levels of about -53 MPa are predicted, in good agreement with experimental observations of about -50 MPa. Calculated values inside the bulk predict TRSS levels of about -100 MPa. Experimentally, the negative TRSS inside the twin decreased moving towards the grain boundary. A small TRSS gradient is predicted along the free surface case, while almost no TRSS gradient arises within the bulk simulation. In the neighbor-

ing grain, the calculated free surface TRSS reaches a maximum of about 60 MPa and decreases moving away from the grain boundary. This decay is also in good agreement with experimental observation, where the maximum TRSS is about 50 MPa and decreases moving away from the grain boundary. Similar trends were observed in the bulk of the simulation, however, with a higher maximum of $\sim$ 90 MPa and a larger gradient. The results in Figure 5.6 help to validate the effectiveness of taking into account free surface effects in the accurate representation of simulated materials. Furthermore, this approach offers a way to gain insight that may help to bridge a connection between the results obtained from lab-scale samples and what can be expected in their bulk counterparts.

While overall good agreement is achieved when free surfaces are modeled, some quantitative differences are noted. The calculated near grain boundary stresses deviate slightly in value, a difference that can be attributed to the fact that the actual grain boundaries are much more complex and more morphologically rough than those represented in the model. The overlapping fields from nearby twins seen in EBSD were not included in the simulation and it is possible that these are non-negligible [65]. The modeling method introduces a perfectly flat free surface, one that does not account for any surface damage effects commonly associated with sample preparation, such as mechanical polishing, electrochemical polishing or ion beam milling and are highly dependent on the material itself [106, 213]. Both the deformation and sample preparation may have introduced some strain hardening, while, for simplicity, no strain hardening was considered in these calculations. Last, apart from in-plane sources, there is the influence of out-of-plane differences between the sample and model. Without information on the subsurface structure, the present model is quasi-3D columnar and the constraints on the surface grains from those neighbor grains below the sample surface may not be the same.

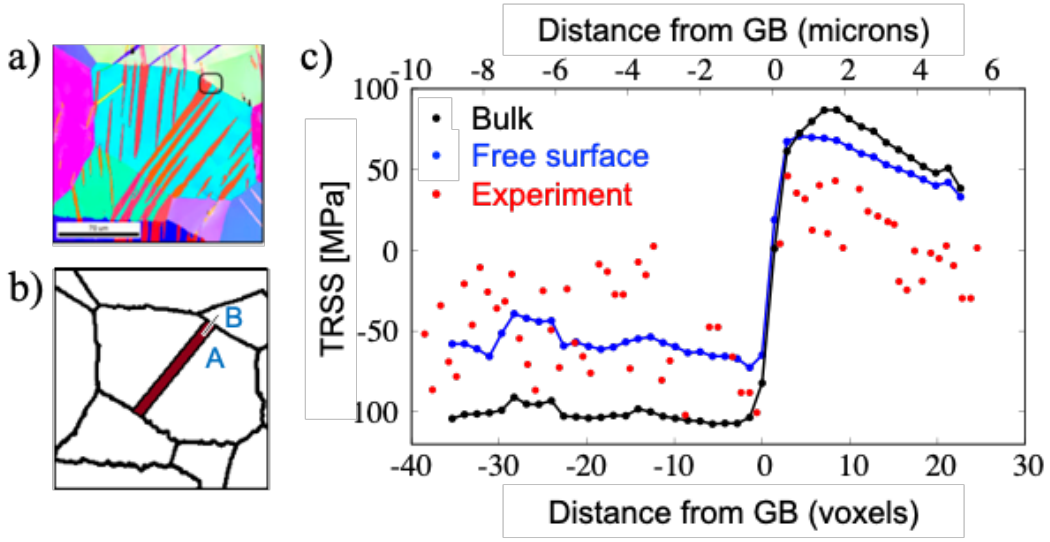

Figure 5.6: Comparison between the calculated and measured TRSS fields across a grain boundary in polycrystalline Ti. a) EBSD image of the region of interest taken from Basu et al. [9] with the twin tip and grain boundary circled in black. b) Shows the digitized microstructure used for the EVP-FFT simulation. Only one twin is simulated in order to isolate the stress fields produced from the twin. c) Comparison between calculated TRSS levels in the bulk (black) and at the simulated free surface (blue) and the experimentally measure values (red) measured along line AB seen in Figure 6b.

5.14 Summary

In this study, a full-field crystal-plasticity based elasto-visco-plastic fast-Fourier-transform (EVP-FFT) model was used to simulate the effects of free surfaces on the stress fields developing in and around a twin. The results help to forecast how these effects may influence slip activity and further twin propagation and growth. In close approximation to TEM sample preparation, a model thin film was sectioned from the center of the simulation cell by removing material on both sides of the film in order to simulate the creation of free surfaces. Material removal was accomplished by setting the materials on both sides the thin film to be elastically isotropic and super compliant, approximating the response of a vacuum.

The model provides for calculations of the micromechanical fields that would develop

during different stages typically involved in characterization. First, in the bulk sample after twinning, then in the thin film sample after free surface relaxation. Later, the bulk twinned material and the thin film material containing a twin are independently loaded to study how the twin may continue developing in each. Overall, the results predict different behavior between the bulk and thin film responses. The following conclusions are drawn:

1. Free surface relaxation, in general, increases TRSS fields inside and surrounding twin, thus enhancing twin tip propagation and twin thickening. Also, twin tip blunting and asymmetric propagation are promoted near free surfaces relative to the same twin in bulk. Twin volume fractions in the interior of the bulk may be much lower than commonly reported by microscopy observations.

2. Under further loading, the results suggest that twins near free surfaces would tend to assume a lower aspect ratio (twin length in shear direction/twin thickness in the normal direction) than in the bulk, resulting in thicker twins with blunted tips.

3. Twin boundary structure can be influenced by free surfaces. Basal/prismatic (BP) and prismatic/basal (PB) facets migration are promoted near free surfaces, resulting in longer facets than in the bulk. This may help to reconcile some discrepancies between TEM observations and atomistic simulations.

4. The introduction of free surfaces itself is sufficient to activate basal, prismatic and pyramidal slip in localized regions ahead of the twin. That is, basal slip is concentrated in two localized bands emanating diagonally from the twin tip. Prismatic slip is concentrated in a single thin band centered at the twin tip. Pyramidal-I slip is slightly produced at the twin tip.

5. The plastic response of the twin matrix and the surrounding parent matrix is different in the bulk when compared to a thin film.

   (a) Basal slip activates more readily in the thin film due to higher driving stresses.

   (b) Prismatic slip is possible inside the twin in the bulk, but less likely in twin in the thin film due to reduced driving stresses from free surface relaxation. Free surface relaxation activates prismatic slip at the twin tip in the thin film that would otherwise not be activated in the bulk.

   (c) Pyramidal slip is imminent inside the twin and the surrounding parent matrix in the bulk, but free surface relaxation reduces the driving stresses, making pyramidal slip in these regions unlikely in the thin film. At the same time, free surface relaxation enhances the driving force for pyramidal slip at the twin tip when compared to the bulk.

By simulating free surface relaxations, computed micromechanical fields become quantitatively and qualitatively more comparable to experimentally measured values taken from near free surface techniques, such as SEM and TEM. Elucidating the differences in these fields could help in translating experimentally measured values to bulk material behavior, which allows for an efficient and accelerated design of materials for industrial applications. This study focused on $\{10\bar{1}2\}$ tensile twinning in Mg and Ti, however, the findings of this study can be extended to other twinning modes in other material systems, since micromechanical fields originate from the twin reorientation and shear that is intrinsic among all twins, although to varying degrees.

Chapter 6

Conclusions and recommendations for future work

6.1 Summary and conclusions

Magnesium alloys have garnered much attention due to the growing need in the transportation industry, and other industries, where structural metals that are simultaneously strong and lightweight can provide tremendous benefits for improving energy efficiency [12, 17]. However, a major limiting factor that has prevented the widespread application of magnesium components has been its limited formability and, in general, complex deformation behaviors [17, 28]. Unlike traditional metals, such as steel and aluminum, magnesium alloys tend to deform by both dislocation mediated slip and twinning. The development of twins has been shown to strongly affect the microstructure, texture development [214, 215, 22, 23], ductility [46, 22], strength [214, 215], and stability [46, 24] of magnesium and its alloys.

The objectives of this research were to investigate the interactions between developing twins and commonly encountered microstructural features found in Mg alloys, such as

precipitates and free surfaces. An EVP-FFT model was used to isolate the interactions between individually and sequentially propagating twins during the early stages of twinning. The resulting stresses generated by the interactions have been quantified and local regions have been identified as likely sites for the nucleation of new twins. A new twin formed in one of these sites, across from the impinging twin, was shown to enable the growth of the primary twin by relaxing the backstresses around the twin and generating dislocations along the twin boundary. A two-step twin growth mechanism is proposed that enables the growth of large twin domains in a field of precipitates, whereby: first an incoming twin becomes arrested at a precipitate, then a second twin nucleates on the other side of the precipitate (across from the first twin). Key microstructural features, such as precipitate length, thickness, and spacing, are identified that influence that proliferation of twins in Mg alloys. With the advanced understanding of how twins interact with elastically hard precipitates, it is expected that results from this work may provide guidance in the design and processing of future Mg alloys with optimized precipitate distributions, geometry and sizes.

Finally, the effects of free surfaces on the stress fields and strain accommodation by slip around twins are revealed using the EVP-FFT model as well. It was shown that free surface relaxation can induce plasticity along the twin boundaries and at the twin tips. Free surfaces were shown significantly alter the stress states in and around twins, which strongly influences how the surround parent matrix can plastically accommodate the twin and the ability of the twin boundaries to migrate, which ultimately effects the geometry of the twin. Furthermore, it was shown that twins propagating in close-proximity to free surfaces may develop asymmetrically and with higher aspect ratios. By simulating free surface relaxation, the calculations yield closer predictions to experimentally measured values, proving additional confidence for the model to accurately represent material behavior. The differences in twinning and slip behavior at free surfaces compared to the

interior of a bulk specimen may aid the interpretation of analysis made using SEM and TEM techniques, that intrinsically have free surfaces effect. The model can be used as a tool to help bridge a connection between the lab-scale samples and bulk material behavior. The improvement and enhancement of the ability to model material behavior can help expedite the engineering of materials for industrial applications.

6.2 Recommendations for future work

The EVP-FFT modeling framework has been implemented to advance the understanding of how deformation twins interact with precipitates and free surfaces. However, there are remains many unanswered questions. The following ideas are recommended for future investigation:

1. Investigation of the interactions between 3D twin domains and precipitates. The present studies have involved twins whose twin plane normal and twin shear direction lie in-plane, thus allowing for a 2D columnar microstructure simplification with fields that match closely to those obtainable through SEM- and TEM-based techniques. However, twins are 3D by nature, can vary in size, be at various stages of development, and can develop complex geometries. The shape of the twin in the out-of-plane direction can influence the local stress fields that develop. The effect of the 3D geometry of the twin can be easily implemented into the EVP-FFT framework, however, at greater computational costs. The study could be complimented by non-destructive 3D X-ray or neutron diffraction analysis of twinned samples in order to capture the full internal stress/strain tensors.

2. Investigations of the interactions between larger propagating twins and precipitates. The present studies have involved the interactions with newly propagated

twins and precipitates. These twins are relatively thin in comparison to the large dimensions of the precipitates. The effects of larger in-plane and out-of-plane twin dimensions should be investigated to reveal the effects of precipitates on propagating with of varying sizes at different stages of development. Furthermore, the shape of the propagating twin front as it impinges a precipitate can influence the micromechanical fields that develop around the twin and precipitate. For relatively thin twins, the twin front can be approximated as a needle-like shape, however, for relative large twins, the twin front can be sharp or blunted. These effects need to be considered in order to fully understand how precipitates can influence twinning.

3. Investigations of different precipitate types and shapes.

   - The precipitates considered here involve the $Mg_{17}Al_{12}$ plate-shaped basal-precipitate. However, depending on the alloying and heat treatment processes [84, 4, 160], many other precipitates may also form, such as rod-shaped precipitates in Mg-Zn alloys [216] and plate-shaped precipitates on the prismatic planes [217]. The geometry, habit plane, size, and distribution of precipitates have been shown to have significant effects on their ability to strengthen dislocation slip [83, 81, 82]. Similar treatment needs to be extended towards precipitates effects on twinning. A study by Liu et al. [97] has begun investigating the effects of precipitate shape, orientation and distribution. An in-depth look at an isolated twin-precipitate interactions may also be insightful in revealing the important factors that influence twin development.

   - Precipitation occurs through both discontinuous precipitation, which takes place at grain boundaries, and continuous precipitation, which takes place in the parent matrix. In these studies, only precipitate found in the center of a grain has been considered, however, the interaction between twins and pre-

cipitates found at the grain boundary be more complicated due to the nature of the grain boundary and close-proximity of a neighboring grain. Recently, Anthony et al. [134] had shown that grain boundary precipitates of varying sizes and geometries can influence the likelihood for twin transmission across the grain boundary. Further investigations into grain boundary misorientation and grain boundary structure are needed.

- It is typically observed that the $Mg_{17}Al_{12}$ plate-shaped basal-precipitate deforms elastically [99, 169]. However, other precipitates, such as c-axis rod-shaped precipitates, have been observed to shear by basal slip [218]. It is important to consider both precipitates that deform elastically and plastically since it would influence their ability to relax internal stresses and harden against slip and twinning. In comparison to individual dislocations impinging against a precipitate, a propagating twin carries with it much larger shears and more intense stress concentrations. Thus, precipitate-twin interactions may shear precipitates more readily than precipitate-dislocation interactions.

4. Investigations of contraction twins. In this work and many others, tensile twins are the focus due to their prevalence at room temperature and strong effects on the overall mechanical behavior of the material. However, contraction twins are also important since they accommodate c-axis compression, an important consideration for industrial applications since the thinning of textured sheets inevitably involves shortening of the c-axis of some grains [51]. Contraction twins can appear as complex double twins and have been shown to cause unique premature failure [51]. The severity of internal micromechanical fields from contraction twins in combination with its relevance in industrial applications merits its further consideration for study.

5. Investigations of different material systems. The bulk of work presented here was concerned with the most common precipitate found in AZ91, due to its relevance as a lightweight structural material. However, ubiquity of the conclusions made from the study of precipitate-twin interactions in AZ91 presented here should be cross-referenced with other material systems where twinning is a prevalent deformation mode, such as in Ti and Zr. In doing so, important material properties that influence twin-precipitate interactions can be revealed. For example, Zr and Ti have different plastic deformation behavior, which could potentially alter the conclusions.

Bibliography

[1] H. Fan and J. A. El-Awady, *Molecular Dynamics Simulations of Orientation Effects during Tension, Compression, and Bending Deformations of Magnesium Nanocrystals*, *Journal of Applied Mechanics, Transactions ASME* **82** (2015), no. 10 1–11.

[2] H. Föll, "Twinning, shear deformation and martensite formation." `https://www.tf.uni-kiel.de/matwis/amat/iss/kap_5/illustr/s5_4_3.html`. Web page accessed on 2021-01-20.

[3] C. Guo, R. Xin, Y. Xiao, G. Liu, and Q. Liu, *Observation and analysis of the coexistence of two "opposite" twin modes in a mg-al-zn alloy*, *Materials Design* **102** (2016) 196–201.

[4] J. F. Nie, *Effects of precipitate shape and orientation on dispersion strengthening in magnesium alloys*, *Scripta Materialia* **48** (2003), no. 8 1009–1015.

[5] K. Y. Xie, D. Zhao, B. Leu, X. Ma, Q. Jiao, J. A. El-Awady, T. P. Weihs, I. J. Beyerlein, and M. A. Kumar, *Understanding the interaction of extension twinning and basal-plate precipitates in Mg-9Al using precession electron diffraction*, *Materialia* **15** (2021), no. 101044.

[6] H. Dini, N. Andersson, and A. E. Jarfors, *Effect of Mg17Al12 Fraction on Mechanical Properties of Mg-9%Al-1%Zn Cast Alloy*, *Metals* **6** (2016) 251.

[7] H. Dini, A. Svoboda, N. E. Andersson, E. Ghassemali, L. E. Lindgren, and A. E. Jarfors, *Optimization and validation of a dislocation density based constitutive model for as-cast Mg-9Engineering A* **710** *(2018) 17–26.*

[8] B. Leu, M. A. Kumar, K. Y. Xie, and I. J. Beyerlein, Twinning pathways enabled by precipitates in AZ91, Materialia **21** *(2022), no. November 2021 101292.*

[9] I. Basu, H. Fidder, V. Ocelík, J. T. M. De Hosson, and J. Th.M de Hosson, Local stress states and microstructural damage response associated with deformation twins in hexagonal close packed metals, Crystals **8** *(2017), no. 1 1.*

[10] *I. Baghni, W. Yinshun, L. Jiuqing, D. Cuiwei, and Z. Wei, Mechanical Properties and potential applications of magnesium alloys,* Transactions of Nonferrous Metals Society of China *(2003).*

[11] *T. Pollock, Weight Loss with Magnesium Alloys,* Science **328** *(2010), no. 5981 986–987.*

[12] *B. L. Mordike and T. Ebert, Magnesium Properties - applications - potential,* Materials Science and Engineering A **302** *(2001), no. 1 37–45.*

[13] *J. Kaufman,* Mechanical Properties Aluminum 6000 series. *1999.*

[14] *M. Singh, Application of Steel Automotive Industry,* International Journal of Emerging Technology and Advanced Engineering **6** *(2016), no. 7 246–253.*

[15] *T. Nakata, C. Xu, R. Ajima, K. Shimizu, S. Hanaki, T. T. Sasaki, L. Ma, K. Hono, and S. Kamado, Strong and ductile age-hardening Mg-Al-Ca-Mn alloy that can be extruded as fast as aluminum alloys,* Acta Materialia **130** *(2017) 261–270.*

[16] *S. Davis, S. Diegel, and R. Boundy,* Transportation Energy Data Book. *Oak Ridge National Laboratory, 34 ed., 2015.*

[17] *W. J. Joost and P. E. Krajewski, Towards magnesium alloys for high-volume automotive applications,* Scripta Materialia **128** *(2017) 107–112.*

[18] *I. Polmear,* Light Alloys From Traditional Alloys to Nanocrystals. *Butterworth-Heinemann, Burlington, 4th ed., 2006.*

[19] *S. R. Kalidindi, A. A. Salem, and R. D. Doherty, Role of deformation twinning on strain hardening in cubic and hexagonal polycrystalline metals,* Advanced Engineering Materials **5** *(2003), no. 4 229–232.*

[20] *C. Tomé, P. Maudlin, R. Lebensohn, and G. Kaschner, Mechanical response of zirconium—i. derivation of a polycrystal constitutive law and finite element analysis,* Acta Materialia **49** *(2001), no. 15 3085–3096.*

[21] *Z. Basinski, M. Szczerba, M. Niewczas, J. Embury, and S. Basinski, The transformation of slip dislocations during twinning of copper-aluminum alloy crystals,* Revue de mEtallurgie **94** *(1997), no. 9 1037–1044.*

[22] *M. R. Barnett, N. Stanford, P. Cizek, A. Beer, Z. Xuebin, and Z. Keshavarz, Deformation mechanisms in mg alloys and the challenge of extending room-temperature Plasticity,* J. of The Minerals, Metals Material Society (TMS) **61** *(2007), no. 8 19–24.*

[23] M. G. Jiang, C. Xu, H. Yan, G. H. Fan, T. Nakata, C. S. Lao, R. S. Chen, S. Kamado, E. H. Han, and B. H. Lu, Unveiling the formation of basal texture variations based on twinning and dynamic recrystallization in AZ31 magnesium alloy during extrusion, Acta Materialia **157** *(2018) 53–71.*

[24] M. R. Barnett, N. Stanford, P. Cizek, A. Beer, Z. Xuebin, and Z. Keshavarz, Deformation mechanisms in mg alloys and the challenge of extending room-temperature Plasticity, .

[25] D. J. Bacon, U. F. Kocks, and R. O. Scattergood, The effect of dislocation self-interaction on the orowan stress, Philosophical Magazine **28** *(1973), no. 6 1241–1263.*

[26] E. Orowan, Discussion on internal stresses, in Symposium on internal stresses in metals and alloys*, pp. 451–453, Institute of Metals London, 1948.*

[27] R. A. Lebensohn, A. K. Kanjarla, and P. Eisenlohr, An elasto-viscoplastic formulation based on fast Fourier transforms for the prediction of micromechanical fields in polycrystalline materials, International Journal of Plasticity **32-33** *(2012) 59–69.*

[28] P. Partridge, The crystallography and deformation modes of hexagonal close-packed metals, Metallurgical Reviews **12** *(1967) 169–194.*

[29] T. Obara, H. Yoshinga, and S. Morozumi, 11221123 Slip system in magnesium, Acta Metallurgica **21** *(1973), no. 7 845–853.*

[30] K. Y. Xie, Z. Alam, A. Caffee, and K. J. Hemker, Pyramidal I slip in c-axis compressed Mg single crystals, Scripta Materialia **112** *(2016) 75–78.*

[31] H. Fan and J. A. El-Awady, Towards resolving the anonymity of pyramidal slip in magnesium, Materials Science and Engineering A **644** *(2015) 318–324.*

[32] R. E. Reed-Hill and W. D. Robertson, Deformation of magnesium single crystals by nonbasal slip, Journal of Metals **9** *(1957), no. 4 496–502.*

[33] I. J. Beyerlein, R. J. Mccabe, and C. N. Tome, Effect of microstructure on the nucleation of deformation twins in polycrystalline high-purity magnesium : A multi-scale modeling study, Journal of the Mechanics and Physics of Solids **59** *(2011) 988–1003.*

[34] A. Chapuis and J. H. Driver, Temperature dependency of slip and twinning in plane strain compressed magnesium single crystals, Acta Materialia **59** *(2011), no. 5 1986–1994.*

[35] *J. J. Bhattacharyya, S. R. Kada, M. R. Barnett, and S. R. Agnew, Crystal plasticity and in-situ diffraction-based determination of the dislocation strengthening and load-sharing effects of precipitates in Mg alloy, AZ91,* Materialia **6** *(2019) 100308.*

[36] *S. R. Agnew, R. P. Mulay, F. J. Polesak, C. A. Calhoun, J. J. Bhattacharyya, and B. Clausen, In situ neutron diffraction and polycrystal plasticity modeling of a Mg-Y-Nd-Zr alloy: Effects of precipitation on individual deformation mechanisms,* Acta Materialia **61** *(2013), no. 10 3769–3780.*

[37] *A. Akhtar and E. Teghtsoonian, Solid solution strengthening of magnesium single crystals-ii the effect of solute on the ease of prismatic slip,* Acta Metallurgica **17** *(1969), no. 11 1351–1356.*

[38] *X. Y. Lou, M. Li, R. K. Boger, S. R. Agnew, and R. H. Wagoner, Hardening evolution of AZ31B Mg sheet,* International Journal of Plasticity **23** *(2007), no. 1 44–86.*

[39] *F. Siska, L. Stratil, J. Cizek, T. Guo, and M. Barnett, Numerical analysis of twin-precipitate interactions in magnesium alloys,* Acta Materialia **202** *(2021) 80–87.*

[40] *B. Clausen, C. N. Tomé, D. W. Brown, and S. R. Agnew, Reorientation and stress relaxation due to twinning: Modeling and experimental characterization for Mg,* Acta Materialia **56** *(2008), no. 11 2456–2468.*

[41] *H. Abdolvand and M. R. Daymond, Internal strain and texture development during twinning: Comparing neutron diffraction measurements with crystal plasticity finite-element approaches,* Acta Materialia **60** *(2012), no. 5 2240–2248.*

[42] *J. Jain, P. Cizek, W. J. Poole, and M. R. Barnett, The role of back stress caused by precipitates on 101-2 twinning in a Mg-6Zn alloy,* Materials Science and Engineering A **647** *(2015) 66–73.*

[43] *J. Wang, X. Wang, K. Yu, T. J. Rupert, S. Mahajan, E. J. Lavernia, J. M. Schoenung, and I. J. Beyerlein, Manipulating deformation mechanisms with Y alloying of Mg,* Materials Science and Engineering A **817** *(2021) 141373.*

[44] *M. H. Yoo, J. R. Morris, K. M. Ho, and S. R. Agnew, Nonbasal deformation modes of HCP metals and alloys: Role of dislocation source and mobility,* Metallurgical and Materials Transactions A: Physical Metallurgy and Materials Science **33** *(2002), no. 3 813–822.*

[45] *S. R. Agnew, M. H. Yoo, and C. N. Tomé, Application of texture simulation to understanding mechanical behavior of Mg and solid solution alloys containing Li or Y,* Acta Materialia **49** *(2001), no. 20 4277–4289.*

[46] *M. H. Yoo, Slip, twinning, and fracture in hexagonal close-packed metals,* Metallurgical Transactions A **12** *(1981), no. 3 409–418.*

[47] *M. R. Barnett, Twinning and the ductility of magnesium alloys. Part I: "Tension" twins,* Materials Science and Engineering A **464** *(2007), no. 1-2 1–7.*

[48] *M. Kang, N. Dixit, K. Hazeli, K. Xie, K. Hemker, and K. T. Ramesh, The mechanical behavior of single crystal and polycrystalline pure magnesium,* Mechanics of Materials **163** *(2021) 104078.*

[49] *P. Cizek and M. R. Barnett, Characteristics of the contraction twins formed close to the fracture surface in Mg-3Al-1Zn alloy deformed in tension,* Scripta Materialia **59** *(2008), no. 9 959–962.*

[50] *C. Cayron, Crystallography of deformation twinning in hexagonal close-packed metals Revisiting the case of the (56˚, a) contraction twins in magnesium,* Acta Crystallographica Section A: Foundations and Advances **73** *(2017), no. 4 346–356.*

[51] *M. R. Barnett, Twinning and the ductility of magnesium alloys. Part II. "Contraction" twins,* Materials Science and Engineering A **464** *(2007), no. 1-2 8–16.*

[52] *J. W. Christian and S. Mahajan, Deformation twinning,* Progress in Materials Science **39** *(1995), no. 1-2 1–157.*

[53] *J. W. Christian,* The theory of transformations in metals and alloys. *Newnes, 2002.*

[54] *M. H. Yoo and J. K. Lee, Deformation twinning in h.c.p. metals and alloys,* Philosophical Magazine A: Physics of Condensed Matter, Structure, Defects and Mechanical Properties **63** *(1991), no. 5 987–1000.*

[55] *I. J. Beyerlein and M. Arul Kumar,* The Stochastic Nature of Deformation Twinning: Application to HCP Materials. *Springer Nature Switzerland, 2018.*

[56] *M. R. Barnett, A. Ghaderi, J. Quinta Da Fonseca, and J. D. Robson, Influence of orientation on twin nucleation and growth at low strains in a magnesium alloy,* Acta Materialia **80** *(2014) 380–391.*

[57] *S. R. Niezgoda, A. K. Kanjarla, I. J. Beyerlein, and C. N. Tomé, Stochastic modeling of twin nucleation in polycrystals: An application in hexagonal close-packed metals,* International Journal of Plasticity **56** *(2014) 119–138.*

[58] *L. Capolungo and I. J. Beyerlein, Nucleation and stability of twins in hcp metals,* Physical Review B - Condensed Matter and Materials Physics **78** *(2008), no. 2 1–19.*

[59] *J. Wang, J. P. Hirth, and C. N. Tomé, Twinning nucleation mechanisms in hexagonal-close-packed crystals,* Acta Materialia **57** *(2009), no. 18 5521–5530.*

[60] *J. Wang, I. J. Beyerlein, and C. N. Tomé, An atomic and probabilistic perspective on twin nucleation in Mg,* Scripta Materialia **63** *(2010), no. 7 741–746.*

[61] *J. Wang, I. J. Beyerlein, J. P. Hirth, and C. N. Tomé, Twinning dislocations on 1011 and 1013 planes in hexagonal close-packed crystals,* Acta Materialia **59** *(2011), no. 10 3990–4001.*

[62] *B. M. Morrow, R. J. McCabe, E. K. Cerreta, and C. N. Tomé, In-situ TEM observation of twinning and detwinning during cyclic loading in Mg,* Metallurgical and Materials Transactions A: Physical Metallurgy and Materials Science **45** *(2014), no. 1 36–40.*

[63] *Q. Yu, J. Zhang, and Y. Jiang, Direct observation of twinning-detwinning-retwinning on magnesium single crystal subjected to strain-controlled cyclic tension-compression in [0 0 0 1] direction,* Philosophical Magazine Letters **91** *(2011), no. 12 757–765.*

[64] *L. Balogh, S. R. Niezgoda, A. K. Kanjarla, D. W. Brown, B. Clausen, W. Liu, and C. N. Tomé, Spatially resolved in situ strain measurements from an interior twinned grain in bulk polycrystalline AZ31 alloy,* Acta Materialia **61** *(2013).*

[65] *M. Arul Kumar, B. Leu, P. Rottmann, and I. J. Beyerlein, Characterization of Staggered Twin Formation in HCP Magnesium, in* TMS Magnesium Technology 2019*, pp. 207–213, TMS, 2019.*

[66] *M. Arul Kumar, A. K. Kanjarla, S. R. Niezgoda, R. A. Lebensohn, and C. N. Tomé, Numerical study of the stress state of a deformation twin in magnesium,* Acta Materialia **84** *(2015) 349–358.*

[67] *D. E. Spearot, L. Capolungo, and C. N. Tomé, Shear-driven motion of mg {10 1¯ 2} twin boundaries via disconnection terrace nucleation, growth, and coalescence,* Physical Review Materials **3** *(2019), no. 5 053606.*

[68] *A. Serra and D. J. Bacon, A new model for (1012) twin growth in hcp metals,* Philosophical Magazine A: Physics of Condensed Matter, Structure, Defects and Mechanical Properties **73** *(1996), no. 2 333–343.*

[69] *J. Wang, L. Liu, C. N. Tomé, S. X. Mao, and S. K. Gong, Twinning and de-twinning via glide and climb of twinning dislocations along serrated coherent twin boundaries in hexagonal-close-packed metals,* Materials Research Letters **1** *(2013), no. 2 81–88.*

[70] *B. Xu, L. Capolungo, and D. Rodney, On the importance of prismatic/basal interfaces in the growth of (1¯012) twins in hexagonal close packed crystals,* Scripta Materialia **68** *(2013), no. 11 901–904.*

[71] *F. Wang and S. R. Agnew, Dislocation transmutation by tension twinning in magnesium alloy AZ31,* International Journal of Plasticity **81** *(2016) 63–86.*

[72] *A. Ostapovets and R. Gröger, Twinning disconnections and basal-prismatic twin boundary in magnesium,* Modelling and Simulation in Materials Science and Engineering **22** *(2014), no. 2.*

[73] *J. Zhang, G. Xi, X. Wan, and C. Fang, The dislocation-twin interaction and evolution of twin boundary in AZ31 Mg alloy,* Acta Materialia **133** *(2017) 208–216.*

[74] *J. Wang, L. Liu, C. N. Tomé, S. X. Mao, and S. K. Gong, Twinning and de-twinning via glide and climb of twinning dislocations along serrated coherent twin boundaries in hexagonal-close-packed metals,* Materials Research Letters **1** *(2013), no. 2 81–88.*

[75] *H. Wang, P. D. Wu, J. Wang, and C. N. Tomé, A crystal plasticity model for hexagonal close packed (HCP) crystals including twinning and de-twinning mechanisms,* International Journal of Plasticity **49** *(2013) 36–52.*

[76] *R. J. McCabe, M. A. Kumar, W. Liu, C. N. Tomé, and L. Capolungo, Revealing the effect of local stresses on twin growth mechanisms in titanium using synchrotron X-ray diffraction,* Acta Materialia **221** *(2021) 117359.*

[77] *T. Gladman, Precipitation hardening in metals,* Materials science and technology **15** *(1999), no. 1 30–36.*

[78] *S. Tang, T. Xin, W. Xu, D. Miskovic, G. Sha, Z. Quadir, S. Ringer, K. Nomoto, N. Birbilis, and M. Ferry, Precipitation strengthening in an ultralight magnesium alloy,* Nature communications **10** *(2019), no. 1 1–8.*

[79] *D. N. Seidman, E. A. Marquis, and D. C. Dunand, Precipitation strengthening at ambient and elevated temperatures of heat-treatable al(sc) alloys,* Acta Materialia **50** *(2002), no. 16 4021–4035.*

[80] *C. Y. Wang, C. M. Cepeda-Jiménez, and M. T. Pérez-Prado, Dislocation-particle interactions in magnesium alloys,* Acta Materialia **194** *(2020) 190–206.*

[81] *F. Wang, J. J. Bhattacharyya, and S. R. Agnew, Effect of precipitate shape and orientation on Orowan strengthening of non-basal slip modes in hexagonal crystals, application to magnesium alloys,* Materials Science and Engineering A **666** *(2016) 114–122.*

[82] *J. D. Robson, N. Stanford, and M. R. Barnett, Effect of precipitate shape and habit on mechanical asymmetry in magnesium alloys,* Metallurgical and Materials Transactions A: Physical Metallurgy and Materials Science **44** *(2013), no. 7 2984–2995.*

[83] *N. Stanford, J. Geng, Y. B. Chun, C. H. Davies, J. F. Nie, and M. R. Barnett, Effect of plate-shaped particle distributions on the deformation behaviour of magnesium alloy AZ91 in tension and compression,* Acta Materialia **60** *(2012), no. 1 218–228.*

[84] *J. P. Zhou, D. S. Zhao, R. H. Wang, Z. F. Sun, J. B. Wang, J. N. Gui, and O. Zheng, In situ observation of ageing process and new morphologies of continuous precipitates in AZ91 magnesium alloy,* Materials Letters **61** *(2007), no. 25 4707–4710.*

[85] *C. R. Hutchinson, J. F. Nie, and S. Gorsse, Modeling the precipitation processes and strengthening mechanisms in a Mg-Al-(Zn) AZ91 alloy,* Metallurgical and Materials Transactions A: Physical Metallurgy and Materials Science **36** *(2005), no. 8 2093–2105.*

[86] *J. B. Clark, Age hardening in a Mg-9 wt.% Al alloy,* Acta Metallurgica **16** *(1968), no. 2 141–152.*

[87] *D. Duly, M. C. Cheynet, and Y. Brechet, Morphology and chemical nanoanalysis of discontinuous precipitation in MgAl alloys-I. Regular growth,* Acta Metallurgica Et Materialia **42** *(1994), no. 11 3843–3854.*

[88] *M. X. Zhang and P. M. Kelly, Crystallography of Mg17Al12 precipitates in AZ91D alloy,* Scripta Materialia **48** *(2003), no. 5 647–652.*

[89] *J. Wang, I. J. Beyerlein, and C. N. Tomé, An atomic and probabilistic perspective on twin nucleation in Mg,* Scripta Materialia **63** *(2010), no. 7 741–746.*

[90] *J. D. Robson, N. Stanford, and M. R. Barnett, Effect of particles in promoting twin nucleation in a Mg-5 wt.% Zn alloy,* Scripta Materialia **63** *(2010), no. 8 823–826.*

[91] *J. Jain, W. Poole, C. Sinclair, and M. Gharghouri, Reducing the tension–compression yield asymmetry in a mg–8al–0.5zn alloy via precipitation,* Scripta Materialia **62** *(2010), no. 5 301–304.*

[92] *B. Zhang, C. Yang, Y. Sun, J. Li, and F. Liu, Effects of aln reinforcement particles on the twinning nucleation and growth in az91 alloy,* Materials Today Communications **24** *(2020) 101023.*

[93] *X. Z. Tang and Y. F. Guo, The engulfment of precipitate by extension twinning in Mg–Al alloy,* Scripta Materialia **188** *(2020) 195–199.*

[94] *M. R. Barnett and H. Wang, Interaction Between Propagating Twins and Non-shearable Precipitates in Magnesium Alloys, in* TMS Magnesium Technology 2018*, pp. 365–367, TMS, 2018.*

[95] *P. Hidalgo-Manrique and J. D. Robson, Interaction Between Precipitate Basal Plates and Tensile Twins in Magnesium Alloys,* Metallurgical and Materials Transactions A: Physical Metallurgy and Materials Science **50** *(2019), no. 8 3855–3867.*

[96] *M. R. Barnett, Twinning Super Dislocations to Help Understand Strength, in* Magnesium Technology 2017*, pp. 143–145, 2017.*

[97] *C. Liu, P. Shanthraj, J. D. Robson, M. Diehl, S. Dong, J. Dong, W. Ding, and D. Raabe, On the interaction of precipitates and tensile twins in magnesium alloys,* Acta Materialia **178** *(2019) 146–162.*

[98] *H. Fan, Y. Zhu, J. A. El-Awady, and D. Raabe, Precipitation hardening effects on extension twinning in magnesium alloys,* International Journal of Plasticity **106** *(2018), no. March 186–202.*

[99] *M. A. Gharghouri, G. C. Weatherly, and J. D. Embury, The interaction of twins and precipitates in a Mg-7.7 at.% Al alloy,* Philosophical Magazine A: Physics of Condensed Matter, Structure, Defects and Mechanical Properties **78** *(1998), no. 5 1137–1149.*

[100] *N. Stanford and M. R. Barnett, Effect of particles on the formation of deformation twins in a magnesium-based alloy,* Materials Science and Engineering A **516** *(2009), no. 1-2 226–234.*

[101] *J. D. Robson and M. R. Barnett, The Effect of Precipitates on Twinning in Magnesium Alloys,* Advanced Engineering Materials **21** *(2019), no. 4.*

[102] *P. Rangaswamy, M. A. Bourke, D. W. Brown, G. C. Kaschner, R. B. Rogge, M. G. Stout, and C. N. Tome, A study of twinning in zirconium using neutron diffraction and polycrystalline modeling,* Metallurgical and Materials Transactions A **33** *(2002), no. 3 757–763.*

[103] *O. Muránsky, D. G. Carr, P. Šittner, and E. C. Oliver, In situ neutron diffraction investigation of deformation twinning and pseudoelastic-like behaviour of extruded AZ31 magnesium alloy,* International Journal of Plasticity **25** *(2009), no. 6 1107–1127.*

[104] *C. C. Aydiner, J. V. Bernier, B. Clausen, U. Lienert, C. N. Tomé, and D. W. Brown, Evolution of stress in individual grains and twins in a magnesium alloy aggregate,* Physical Review B **80** *(2009), no. 2 1–6.*

[105] *P. J. Withers and P. J. Webster, Neutron and synchrotron X-ray strain scanning,* Strain **37** *(2001), no. 1 19–33.*

[106] *Y. Leng,* Materials characterization: Introduction to microscopic and spectroscopic methods: Second edition. *John Wiley Sons, 2013.*

[107] *J. R. Greer, W. C. Oliver, and W. D. Nix, Size dependence of mechanical properties of gold at the micron scale in the absence of strain gradients,* Acta Materialia **53** *(2005), no. 6 1821–1830.*

[108] *J. R. Greer and W. D. Nix, Nanoscale gold pillars strengthened through dislocation starvation,* Physical Review B - Condensed Matter and Materials Physics **73** *(2006), no. 24 1–6.*

[109] *Z. W. Shan, R. K. Mishra, S. A. Syed Asif, O. L. Warren, and A. M. Minor, Mechanical annealing and source-limited deformation in submicrometre- diameter Nicrystals,* Nature Materials **7** *(2008), no. 2 115–119.*

[110] *H. Suzuki, S. Ikeda, and S. Takeuchi, Deformation in thin copper crystals.pdf,* Journal of the Physical Society of Japan **11** *(1956), no. 4 382–393.*

[111] *J. T. Fourie, The flow stress gradient between the surface and centre of deformed copper single crystals,* Philosophical Magazine **17** *(1968), no. 148 735–756.*

[112] *H. Mughrabi, Some consequences of surface and size effects in plastically deformed copper single crystals,* Physica Status Solidi (B) **44** *(1971), no. 1 391–402.*

[113] *C. Keller, E. Hug, A. M. Habraken, and L. Duchene, Finite element analysis of the free surface effects on the mechanical behavior of thin nickel polycrystals,* International Journal of Plasticity **29** *(2012), no. 1 155–172.*

[114] *F. Pettinari-Sturmel, G. Saada, J. Douin, A. Coujou, and N. Clément, Quantitative analysis of dislocation pile-ups in thin foils compared to bulk,* Materials Science and Engineering A **387-389** *(2004), no. 1-2 SPEC. ISS. 109–114.*

[115] *L. Liu, Z. Meng, G. Xu, C. He, X. Wu, and R. Wang, Surface Effects on the Properties of Screw Dislocation in Nanofilms,* Advances in Materials Science and Engineering **2017** *(2017), no. 1.*

[116] *B. Gars and X. Markenscoff, The Peierls stress for coupled dislocation partials near a free surface,* Philosophical Magazine **92** *(2012), no. 11 1390–1421.*

[117] *W. Wu, R. Schäublin, and J. Chen, General dislocation image stress of anisotropic cubic thin film,* Journal of Applied Physics **112** *(2012), no. 9.*

[118] *C. L. Lee and S. Li, A half-space Peierls-Nabarro model and the mobility of screw dislocations in a thin film,* Acta Materialia **55** *(2007), no. 6 2149–2157.*

[119] *X. Cheng, Y. Shen, L. Zhang, and X. Liu, Surface effect on the screw dislocation mobility over the Peierls barrier,* Philosophical Magazine Letters **92** *(2012), no. 6 270–277.*

[120] *C. R. Weinberger, Dislocation drag at the nanoscale,* Acta Materialia **58** *(2010), no. 19 6535–6541.*

[121] *C. R. Weinberger, Comment on "lattice resistance to dislocation motion at the nanoscale",* Physical Review Letters **105** *(2010), no. 9 99601.*

[122] *Y. Liu, E. Van der Giessen, and A. Needleman, An analysis of dislocation nucleation near a free surface,* International Journal of Solids and Structures **44** *(2007), no. 6 1719–1732.*

[123] *T. A. Khraishi and H. M. Zbib, Free-surface effects in 3D dislocation dynamics: Formulation and modeling,* Journal of Engineering Materials and Technology, Transactions of the ASME **124** *(2002), no. 3 342–351.*

[124] *A. A. Kohnert, H. Tummala, R. A. Lebensohn, C. N. Tomé, and L. Capolungo, On the use of transmission electron microscopy to quantify dislocation densities in bulk metals,* Scripta Materialia **178** *(mar, 2020) 161–165.*

[125] *J. C. Crone, L. B. Munday, and J. Knap, Capturing the effects of free surfaces on void strengthening with dislocation dynamics,* Acta Materialia **101** *(2015) 40–47.*

[126] *D. M. Barnett and J. Lothe, Journal of Physics F : Metal Physics Related content An image force theorem for dislocations in anisotropic bicrystals An image force theorem for dislocations in anisotropic bicrystals,* Journal of Physics: Metal Physics **4** *(1974).*

[127] *A. Datta, A. Srirangarajan, U. V. Waghmare, U. Ramamurty, and A. C. To, Surface effects on stacking fault and twin formation in fcc nanofilms: A first-principles study,* Computational Materials Science **50** *(2011), no. 12 3342–3345.*

[128] *H. Moulinec and P. Suquet, A fast numerical method for computing the linear and nonlinear mechanical properties of composites,* Comptes rendus de l'Académie des sciences. Série II, Mécanique, physique, chimie, astronomie **318** *(1994), no. 11 1417–1423.*

[129] *H. Moulinec and P. Suquet, A numerical method for computing the overall response of nonlinear composites with complex microstructure,* Computer Methods in Applied Mechanics and Engineering **157** *(1998), no. 1-2 69–94, [arXiv:2012.0896].*

[130] *R. Brenner, R. A. Lebensohn, and O. Castelnau, Elastic anisotropy and yield surface estimates of polycrystals,* International Journal of Solids and Structures **46** *(2009), no. 16 3018–3026.*

[131] *R. A. Lebensohn, N-site modeling of a 3D viscoplastic polycrystal using Fast Fourier Transform,* Acta Materialia **49** *(2001), no. 14 2723–2737.*

[132] *M. Arul Kumar, I. J. Beyerlein, and C. N. Tomé, Effect of local stress fields on twin characteristics in HCP metals,* Acta Materialia **116** *(2016) 143–154.*

[133] *M. Arul Kumar, I. J. Beyerlein, R. J. McCabe, and C. N. Tomé, Grain neighbour effects on twin transmission in hexagonal close-packed materials,* Nature Communications **7** *(2016) 13826.*

[134] *B. Anthony, B. Leu, I. Beyerlein, and V. Miller, Deformation twin interactions with grain boundary particles in multi-phase magnesium alloys,* Acta Materialia **219** *(2021) 117225.*

[135] *J. W. Zhang, B. Leu, M. A. Kumar, I. J. Beyerlein, and W. Z. Han, Twin hopping in nanolayered Zr-2.5Nb,* Materials Research Letters **8** *(2020), no. 8 307–313.*

[136] *B. Leu, M. Arul Kumar, and I. J. Beyerlein, Influence of Layer Thickness on Deformation Twinning in Mg/Nb Laminates, in* Magnesium Technology 2021*, pp. 3–6, TMS, 2021.*

[137] *B. Leu, M. Arul Kumar, and I. J. Beyerlein, The effects of free surfaces on deformation twinning in HCP metals,* Materialia **17** *(2021), no. January 101124.*

[138] *Y. Liu, N. Li, S. Shao, M. Gong, J. Wang, R. J. McCabe, Y. Jiang, and C. N. Tomé, Characterizing the boundary lateral to the shear direction of deformation twins in magnesium,* Nature Communications **7** *(2016) 8–13.*

[139] *W. Callister and D. Rethwisch,* Materials Science and Eng. *John Wiley Sons, Inc., MA, 9 ed., 2014.*

[140] *A. D. Rollett and U. F. Kocks, A review of the stages of work hardening, in* In Solid State Phenomena 1993*, pp. 1–18, Trans Tech Publications Ltd, 1993.*

[141] *D. Kuhlmann-Wilsdorf, Theory of workhardening 1934-1984,* Metallurgical Transactions A **16** *(1985), no. 12 2091–2108.*

[142] S. Kalidindi, C. Bronkhorst, and L. Anand, Crystallographic texture evolution in bulk deformation processing of FCC metals, Journal of the Mechanics and Physics of Solids **40** *(1992), no. 3 537–569.*

[143] D. Raabe, M. Sachtleber, Z. Zhao, F. Roters, and S. Zaefferer, Micromechanical and macromechanical effects in grain scale polycrystal plasticity experimentation and simulation, Acta Materialia **49** *(2001), no. 17 3433–3441.*

[144] E. Voce, The relationship between stress and strain for homogeneous deformation, Journal of the Institute of Metals **74** *(1948) 537–562.*

[145] I. J. Beyerlein and C. N. Tomé, A dislocation-based constitutive law for pure Zr including temperature effects, International Journal of Plasticity **24** *(2008), no. 5 867–895.*

[146] R. Madec, B. Devincre, and L. P. Kubin, From Dislocation Junctions to Forest Hardening, Physical Review Letters **89** *(2002), no. 25 1–4.*

[147] G. Saada, Dynamical effects in crystal plasticity, in Key Engineering Materials*, vol. 97, pp. 275–286, Trans Tech Publ, 1994.*

[148] G. Thomas, Electron microscopy and strength of crystals, .

[149] Y. Dai and M. Victoria, Defect structures in deformed F.C.C. metals, Acta Materialia **45** *(1997), no. 8 3495–3501.*

[150] U. Essmann and H. Mughrabi, Annihilation of dislocations during tensile and cyclic deformation and limits of dislocation densities, Philosophical Magazine A **40** *(1979), no. 6 731–756.*

[151] F. F. Lavrentev and Y. A. Pokhil, Effect of Forest Dislocations in the 1122 1123 system on hardening in Mg single crystals under basal slip, Physica Status Solidi (a) **32** *(1975), no. 1 227–232.*

[152] P. Franciosi and A. Zaoui, Multislip in f.c.c. crystals a theoretical approach compared with experimental data, Acta Metallurgica **30** *(1982), no. 8 1627–1637.*

[153] H. Mecking and U. F. Kocks, Kinetics of flow and strain-hardening, Acta Metallurgica **29** *(1981), no. 11 1865–1875.*

[154] F. Lavrentev, The type of dislocation interaction as the factor determining work hardening, Materials Science and Engineering **46** *(1980), no. 2 191–208.*

[155] U. F. Kocks and H. Mecking, Physics and phenomenology of strain hardening: the FCC case, Progress in Materials Science **48** *(2003) 172–268.*

[156] *J. J. Gilman, Toward physically-based rate laws for dislocations,* Materials Science and Engineering A **322** *(2002), no. 1-2 126–131.*

[157] *D. Mordehai, Y. Ashkenazy, I. Kelson, and G. Makov, Dynamic properties of screw dislocations in Cu: A molecular dynamics study,* Physical Review B - Condensed Matter and Materials Physics **67** *(2003), no. 2 1–9.*

[158] *U. Kocks, Termodynamics and kinetics of slip,* Prog. in Mater. Sci. **242** *(1975).*

[159] *D. Zhao, X. Ma, A. Srivastava, G. Turner, I. Karaman, and K. Y. Xie, Significant disparity of non-basal dislocation activities in hot-rolled highly-textured Mg and Mg-3Al-1Zn alloy under tension,* Acta Materialia **207** *(2021) 116691.*

[160] *J. D. Robson, N. Stanford, and M. R. Barnett, Effect of precipitate shape on slip and twinning in magnesium alloys,* Acta Materialia **59** *(2011), no. 5 1945–1956.*

[161] *C. Y. Wang, C. M. Cepeda-Jiménez, and M. T. Pérez-Prado, Dislocation-particle interactions in magnesium alloys,* Acta Materialia **194** *(2020) 190–206.*

[162] *J. J. Bhattacharyya, F. Wang, N. Stanford, and S. R. Agnew, Slip mode dependency of dislocation shearing and looping of precipitates in Mg alloy WE43,* Acta Materialia **146** *(2018) 55–62.*

[163] *L. Jiang, M. A. Kumar, I. J. Beyerlein, X. Wang, D. Zhang, C. Wu, C. Cooper, T. J. Rupert, S. Mahajan, E. J. Lavernia, and J. M. Schoenung, Twin formation from a twin boundary in Mg during in-situ nanomechanical testing,* Materials Science and Engineering A **759** *(2019), no. January 142–153.*

[164] *E. L. S. Solomon and E. A. Marquis, Deformation behavior of b' and b"' precipitates in Mg-RE alloys,* Materials Letters **216** *(2018) 67–69.*

[165] *I. J. Beyerlein and C. N. Tomé, A probabilistic twin nucleation model for HCP polycrystalline metals,* Proceedings of the Royal Society A: Mathematical, Physical and Engineering Sciences **466** *(2010), no. 2121 2517–2544.*

[166] *F. Zhang, Y. Ren, Z. Yang, H. Su, Z. Lu, C. Tan, H. Peng, K. Watanabe, B. Li, M. R. Barnett, and M. Chen, The interaction of deformation twins with long-period stacking ordered precipitates in a magnesium alloy subjected to shock loading,* Acta Materialia **188** *(2020) 203–214.*

[167] *X. Z. Tang and Y. F. Guo, The engulfment of precipitate by extension twinning in Mg–Al alloy,* Scripta Materialia **188** *(2020) 195–199.*

[168] *G. Simmons and H. Wang,* Single Crystal Elastic Constants and Calculated Aggregate Progress*, vol. 34. The M.I.T. Press, 2nd ed., 1965.*

[169] N. Wang, W. Y. Yu, B. Y. Tang, L. M. Peng, and W. J. Ding, Structural and mechanical properties of Mg17Al12 and Mg24Y5 from first-principles calculations, Journal of Physics D: Applied Physics **41** *(2008), no. 19.*

[170] J. D. Robson, The effect of internal stresses due to precipitates on twin growth in magnesium, Acta Materialia **121** *(2016) 277–287.*

[171] X. Ma, Q. Jiao, L. J. Kecskes, J. A. El-Awady, and T. P. Weihs, Effect of basal precipitates on extension twinning and pyramidal slip: A micro-mechanical and electron microscopy study of a Mg–Al binary alloy, Acta Materialia **189** *(2020) 35–46.*

[172] S. Si, J. Wu, I. P. Jones, and Y. L. Chiu, Influence of precipitates on basal dislocation slip and twinning in AZ91 micro-pillars, Philosophical Magazine *(2020) 2949–2971.*

[173] B. Zhang, C. Yang, Y. Sun, J. Li, and F. Liu, Effects of AlN reinforcement particles on the twinning nucleation and growth in AZ91 alloy, Materials Today Communications **24** *(2020), no. February 101023.*

[174] Q. Yu, J. Wang, Y. Jiang, R. J. McCabe, and C. N. Tomé, Co-zone (1012) twin interaction in magnesium single crystal, Materials Research Letters **2** *(2014), no. 2 82–88.*

[175] M. Arul Kumar, L. Capolungo, R. J. McCabe, and C. N. Tomé, Characterizing the role of adjoining twins at grain boundaries in hexagonal close packed materials, Scientific Reports **9** *(2019), no. 1 1–10.*

[176] Y. Zhu and X. Wu, Perspective on hetero deformation induced (HDI) hardening and backstress, Materials Research Letters **7** *(2019), no. 10 393–398.*

[177] N. Stanford and M. R. Barnett, Solute strengthening of prismatic slip, basal slip and 1012 twinning in Mg and Mg-Zn binary alloys, International Journal of Plasticity **47** *(2013) 165–181.*

[178] W. Z. Han, J. S. Carpenter, J. Wang, I. J. Beyerlein, and N. A. Mara, Atomic-level study of twin nucleation from face-centered-cubic/body-centered-cubic interfaces in nanolamellar composites, Applied Physics Letters **100** *(2012), no. 1.*

[179] H. Wang, B. Clausen, L. Capolungo, I. J. Beyerlein, J. Wang, and C. N. Tomé, Stress and strain relaxation in magnesium AZ31 rolled plate: In-situ neutron measurement and elastic viscoplastic polycrystal modeling, International Journal of Plasticity **79** *(2016) 275–292.*

[180] *G. Gottstein and T. A. Samman, Texture Development in Pure Mg and Mg Alloy AZ31,* Materials Science Foru **495-497** *(2005), no. 1 623–632.*

[181] *B. A. Simkin, B. C. Ng, M. A. Crimp, and T. R. Bieler, Crack opening due to deformation twin shear at grain boundaries in near-γ TiAl,* Intermetallics **15** *(2007), no. 1 55–60.*

[182] *R. H. Wagoner, X. Y. Lou, M. Li, and S. R. Agnew, Forming behavior of magnesium sheet,* Journal of Materials Processing Technology **177** *(2006), no. 1-3 483–485.*

[183] *S. J. Zheng, J. Wang, J. S. Carpenter, W. M. Mook, P. O. Dickerson, N. A. Mara, and I. J. Beyerlein, Plastic instability mechanisms in bimetallic nanolayered composites,* Acta Materialia **79** *(2014) 282–291.*

[184] *J. Wang, M. Ramajayam, E. Charrault, and N. Stanford, Quantification of precipitate hardening of twin nucleation and growth in Mg and Mg-5Zn using micro-pillar compression,* Acta Materialia **163** *(2019) 68–77.*

[185] *J. W. Zhang, B. Leu, M. A. Kumar, I. J. Beyerlein, and W. Z. Han, Twin hopping in nanolayered Zr-2.5Nb,* Materials Research Letters **8** *(2020), no. 8 307–313.*

[186] *J. Zhang, G. Xi, X. Wan, and C. Fang, The dislocation-twin interaction and evolution of twin boundary in AZ31 Mg alloy,* Acta Materialia **133** *(2017) 208–216.*

[187] *A. Ostapovets and R. Gröger, Twinning disconnections and basal-prismatic twin boundary in magnesium,* Modelling and Simulation in Materials Science and Engineering **22** *(2014), no. 2.*

[188] *A. Ostapovets and A. Serra, Characterization of the matrix-twin interface of a (1012) twin during growth,* Philosophical Magazine **94** *(2014), no. 25 2827–2839.*

[189] *K. Dang, S. Wang, M. Gong, R. J. McCabe, J. Wang, and L. Capolungo, Formation and stability of long basal-prismatic facets in Mg,* Acta Materialia **185** *(2020) 119–128.*

[190] *J. Wang, S. K. Yadav, J. P. Hirth, C. N. Tomé, and I. J. Beyerlein, Pure-Shuffle Nucleation of Deformation Twins in Hexagonal-Close-Packed Metals,* Materials Research Letters **1** *(2013), no. 3 126–132.*

[191] *P. A. Olsson, First principles investigation of the finite temperature dependence of the elastic constants of zirconium, magnesium and gold,* Computational Materials Science **99** *(2015) 361–372.*

[192] *M. Avedesian and H. Baker,* Magnesium and magnesium alloys. *1999.*

[193] *N. Bertin, C. N. Tomé, I. J. Beyerlein, M. R. Barnett, and L. Capolungo, On the strength of dislocation interactions and their effect on latent hardening in pure Magnesium,* International Journal of Plasticity **62** *(2014) 72–92.*

[194] *I. J. Beyerlein, R. J. Mccabe, and C. N. Tome, Effect of microstructure on the nucleation of deformation twins in polycrystalline high-purity magnesium : A multi-scale modeling study,* Journal of the Mechanics and Physics of Solids **59** *(2011) 988–1003.*

[195] *J. Wang, S. K. Yadav, J. P. Hirth, C. N. Tomé, and I. J. Beyerlein, Pure-Shuffle Nucleation of Deformation Twins in Hexagonal-Close-Packed Metals,* Materials Research Letters **1** *(2013), no. 3 126–132.*

[196] *F. Wang, K. Hazeli, K. D. Molodov, C. D. Barrett, T. Al-Samman, D. A. Molodov, A. Kontsos, K. T. Ramesh, H. El Kadiri, and S. R. Agnew, Characteristic dislocation substructure in 101¯2 twins in hexagonal metals,* Scripta Materialia **143** *(2018) 81–85.*

[197] *J. P. Hirth, J. Wang, and C. N. Tomé, Disconnections and other defects associated with twin interfaces,* Progress in Materials Science **83** *(2016) 417–471.*

[198] *C. D. Barrett and H. El Kadiri, Impact of deformation faceting on 1 0 1 2 , 1 0 1 1 and 1 0 1 3 embryonic twin nucleation in hexagonal close-packed metals,* Acta Materialia **70** *(2014) 137–161.*

[199] *M. Knezevic, M. R. Daymond, and I. J. Beyerlein, Modeling discrete twin lamellae in a microstructural framework,* Scripta Materialia **121** *(2016) 84–88.*

[200] *J. Senger, D. Weygand, P. Gumbsch, and O. Kraft, Discrete dislocation simulations of the plasticity of micro-pillars under uniaxial loading,* Scripta Materialia **58** *(2008), no. 7 587–590.*

[201] *H. Tang, K. W. Schwarz, and H. D. Espinosa, Dislocation escape-related size effects in single-crystal micropillars under uniaxial compression,* Acta Materialia **55** *(2007), no. 5 1607–1616.*

[202] *M. Wronski, M. Arul Kumar, L. Capolungo, R. J. McCabe, K. Wierzbanowski, and C. N. Tomé, Deformation behavior of CP-titanium: Experiment and crystal plasticity modeling,* Materials Science and Engineering A **724** *(2018), no. February 289–297.*

[203] *M. Arul Kumar, I. J. Beyerlein, and C. N. Tomé, Grain size constraints on twin expansion in hexagonal close packed crystals,* Journal of Applied Physics **120** *(2016), no. 15.*

[204] M. R. Barnett, M. D. Nave, and A. Ghaderi, Yield point elongation due to twinning in a magnesium alloy, Acta Materialia **60** *(2012), no. 4 1433–1443.*

[205] Q. Sun, X. Y. Zhang, Y. Ren, J. Tu, and Q. Liu, Interfacial structure of 101¯2 twin tip in deformed magnesium alloy, Scripta Materialia **90** *(2014), no. 1 41–44.*

[206] Q. Sun, X. Y. Zhang, J. Tu, Y. Ren, H. Qin, and Q. Liu, Characterization of basal-prismatic interface of 101¯2 twin in deformed titanium by high-resolution transmission electron microscopy, Philosophical Magazine Letters **95** *(2015), no. 3 145–151.*

[207] Y. Liu, P. Z. Tang, M. Y. Gong, R. J. McCabe, J. Wang, and C. N. Tomé, Three-dimensional character of the deformation twin in magnesium, Nature Communications **10** *(2019), no. 1 1–7.*

[208] J. Tu, X. Y. Zhang, Z. M. Zhou, and C. Huang, Structural characterization of 10 1¯ 2 twin tip in deformed magnesium alloy, Materials Characterization **110** *(2015) 39–43.*

[209] M. Gong, J. P. Hirth, Y. Liu, Y. Shen, and J. Wang, Interface structures and twinning mechanisms of twins in hexagonal metals, Materials Research Letters **5** *(2017), no. 7 449–464.*

[210] T. Braisaz, P. Ruterana, G. Nouet, and R. C. Pond, Investigation of 1012 twins in zn using high-resolution electron microscopy: Interfacial defects and interactions, Philosophical Magazine A **75** *(1997), no. 4 1075–1095.*

[211] M. Gong, S. Xu, Y. Jiang, Y. Liu, and J. Wang, Structural characteristics of 1¯012 non-cozone twin-twin interactions in magnesium, Acta Materialia **159** *(2018) 65–76.*

[212] H. El Kadiri, C. D. Barrett, J. Wang, and C. N. Tomé, Why are 10 1 ¯ 2 twins profuse in magnesium?, Acta Materialia **85** *(2015) 354–361.*

[213] J. McGrath and C. Davis, Polishing pad surface characterisation in chemical mechanical planarisation, Journal of Materials Processing Technology **153-154** *(2004), no. 1-3 666–673.*

[214] G. Proust, C. N. Tomé, and G. C. Kaschner, Modeling texture, twinning and hardening evolution during deformation of hexagonal materials, Acta Materialia **55** *(2007), no. 6 2137–2148.*

[215] S. R. Agnew, D. W. Brown, and C. N. Tomé, Validating a polycrystal model for the elastoplastic response of magnesium alloy AZ31 using in situ neutron diffraction, Acta Materialia **54** *(2006), no. 18 4841–4852.*

[216] J.-F. Nie, Precipitation and Hardening in Magnesium Alloys, Metallurgical and Materials Transactions A **43** *(nov, 2012) 3891–3939.*

[217] J. F. Nie and B. C. Muddle, Characterisation of strengthening precipitate phases in a Mg-Y-Nd alloy, Acta Materialia **48** *(2000), no. 8 1691–1703.*

*[218] J. Wang and N. Stanford, Investigation of precipitate hardening of slip and twinning in Mg5***100** *(2015) 53–63.*